Spring 2011

Covalently functionalized gold nanoparticles: synthesis, characterization, and integration into capillary electrophoresis

Michael Robert Ivanov
University of Iowa

COVALENTLY FUNCTIONALIZED GOLD NANOPARTICLES: SYNTHESIS, CHARACTERIZATION, AND INTEGRATION INTO CAPILLARY ELECTROPHORESIS

by

Michael Robert Ivanov

An Abstract

Of a thesis submitted in partial fulfillment
of the requirements for the Doctor of
Philosophy degree in Chemistry
in the Graduate College of
The University of Iowa

May 2011

Thesis Supervisor: Assistant Professor Amanda J. Haes

ABSTRACT

Nanomaterials are widely used as pseudostationary and stationary phases in electrically driven separations. The advantages of using nanomaterials are numerous including tunable sizes, multiple core compositions, flexible injection schemes, and diverse surface chemistries. Nanomaterials, however, exhibit large surface energies which induce aggregation and may yield unpredictable function in separations. Because nanomaterials can modify buffer conductivity, viscosity, and pH; successful and systematic incorporation of nanomaterials into separations requires rigorous synthetic control and characterization of both the nanoparticle core and surface chemistry.

This dissertation investigates the impact of gold nanoparticle surface chemistry and morphology to capillary electrophoresis separations. Gold nanoparticle core composition, shape, size, self assembled monolayer (SAM) formation, and SAM packing density are quantified for gold nanoparticles functionalized with thioctic acid, 6-mercaptohexanoic acid, or 11-mercaptoundecanoic acid SAMs. TEM, ^{1}H NMR, extinction spectroscopy, zeta potential, X-ray photoelectron spectroscopy, and flocculation assess the morphology, surface chemistry, optical properties, surface charge, SAM packing density, and stability of the nanoparticles, respectively.

Using well-characterized nanostructures, pseudostationary phases of gold nanoparticles in capillary electrophoresis are studied. Gold nanoparticles functionalized with thioctic acid and either 6-mercaptohexanoic acid or 6-aminohexanethiol impact the mobility of analytes in a concentration and surface chemistry-dependent manner. From these data, a novel parameter termed the critical nanoparticle concentration is developed and is used to estimate nanoparticle stability during capillary electrophoresis separations.

To understand the function of carboxylated gold nanoparticles in capillary electrophoresis, extended DLVO theory is used to model interparticle interactions. Nanoparticle aggregation leads to electron tunneling between nanoparticles thereby taking on bulk electrical properties which cause measured currents to increase for nanoparticles functionalized with poorly ordered SAMs. Nanoparticles functionalized with well-ordered SAMs main their nanoscale properties and reduce measured currents during electrically driven flow.

Finally, carboxylic acid functionalized gold nanoparticles effect the separation of target biomarkers in both a SAM composition and surface coverage dependent manner. These effects are most systematic with well ordered SAMs. To understand the separation mechanism functionalized gold nanoparticles exhibit, their ζ potential with and without dopamine are evaluated. Large dopamine concentrations neutralize the three functionalized gold nanoparticles according to a dose response curve. The positively charged dopamine molecules saturate the negatively charged nanoparticle surfaces thereby providing a plausible explanation to the observed biomarker concentration trends. These data and future work provide a rigorous experimental and theoretical evaluation of nanoparticle structure impacts their function as pseudostationary phases in separations and other applications.

Abstract Approved: _____
Thesis Supervisor

_____
Title and Department

_____
Date

COVALENTLY FUNCTIONALIZED GOLD NANOPARTICLES: SYNTHESIS, CHARACTERIZATION, AND INTEGRATION INTO CAPILLARY ELECTROPHORESIS

by

Michael Robert Ivanov

A thesis submitted in partial fulfillment
of the requirements for the Doctor of
Philosophy degree in Chemistry
in the Graduate College of
The University of Iowa

May 2011

Thesis Supervisor: Assistant Professor Amanda J. Haes

Graduate College
The University of Iowa
Iowa City, Iowa

CERTIFICATE OF APPROVAL

_____

PH.D. THESIS

_____

This is to certify that the Ph.D. thesis of

Michael Robert Ivanov

has been approved by the Examining Committee
for the thesis requirement for the Doctor of Philosophy
degree in Chemistry at the May 2011 graduation.

Thesis Committee: _____
Amanda J. Haes, Thesis Supervisor

_____
Johna Leddy

_____
Vicki H. Grassian

_____
Lou Messerle

_____
Jennifer Fiegel

To Julie with love…

ACKNOWLEDGMENTS

First, this work would have never been possible without the constant loving support of my wife, Julie. Throughout this process you have shared my successes and failures, cried and cared for me. We earned this together, and now I am ready for our next wonderful adventure!

I would also like to thank the tremendously wonderful friends that I have made here at Iowa. First, Tim, whom I will always owe a cup of coffee to for the rest of my life! Your computer skills helped avert a total meltdown and I couldn't ask for a better friend. I will treasure the memories we made here.

I need to also thank Perry and Irma -the Cannonites. It was our friendship and solidarity that helped us overcome a very difficult time. We all stuck with it. I would also like to thank Kristina, Gordy, Dave, Garrett, Steph, and the rest of the Leddy crew. Grad school was always better with you guys around.

Next, I would like to thank the members of the Haes group, both past and present. Through floods we have made it together, and I expect many wonderful accomplishments in the future. Remember to aim high and I believe in each one of you.

Finally, I would like to thank my advisor, Amanda, for accepting this wayward orphan three years ago and for taking a chance on me. I have learned so much and become a better chemist because of your guidance.

Hopefully, my work has helped advanced the detection of suspected Parkinson's disease biomarkers. I would like to end by dedicating my dissertation to Virginia Biver, a wonderful wife, mother, and grandmother who battled Parkinson's bravely and will be missed- you are never far from our thoughts……

MRI 2011

ABSTRACT

Nanomaterials are widely used as pseudostationary and stationary phases in electrically driven separations. The advantages of using nanomaterials are numerous including tunable sizes, multiple core compositions, flexible injection schemes, and diverse surface chemistries. Nanomaterials, however, exhibit large surface energies which induce aggregation and may yield unpredictable function in separations. Because nanomaterials can modify buffer conductivity, viscosity, and pH; successful and systematic incorporation of nanomaterials into separations requires rigorous synthetic control and characterization of both the nanoparticle core and surface chemistry.

This dissertation investigates the impact of gold nanoparticle surface chemistry and morphology to capillary electrophoresis separations. Gold nanoparticle core composition, shape, size, self assembled monolayer (SAM) formation, and SAM packing density are quantified for gold nanoparticles functionalized with thioctic acid, 6-mercaptohexanoic acid, or 11-mercaptoundecanoic acid SAMs. TEM, ^{1}H NMR, extinction spectroscopy, zeta potential, X-ray photoelectron spectroscopy, and flocculation assess the morphology, surface chemistry, optical properties, surface charge, SAM packing density, and stability of the nanoparticles, respectively.

Using well-characterized nanostructures, pseudostationary phases of gold nanoparticles in capillary electrophoresis are studied. Gold nanoparticles functionalized with thioctic acid and either 6-mercaptohexanoic acid or 6-aminohexanethiol impact the mobility of analytes in a concentration and surface chemistry-dependent manner. From these data, a novel parameter termed the critical nanoparticle concentration is developed and is used to estimate nanoparticle stability during capillary electrophoresis separations.

To understand the function of carboxylated gold nanoparticles in capillary electrophoresis, extended DLVO theory is used to model interparticle interactions. Nanoparticle aggregation leads to electron tunneling between nanoparticles thereby taking on bulk electrical properties which cause measured currents to increase for nanoparticles functionalized with poorly ordered SAMs. Nanoparticles functionalized with well-ordered SAMs main their nanoscale properties and reduce measured currents during electrically driven flow.

Finally, carboxylic acid functionalized gold nanoparticles effect the separation of target biomarkers in both a SAM composition and surface coverage dependent manner. These effects are most systematic with well ordered SAMs. To understand the separation mechanism functionalized gold nanoparticles exhibit, their ζ potential with and without dopamine are evaluated. Large dopamine concentrations neutralize the three functionalized gold nanoparticles according to a dose response curve. The positively charged dopamine molecules saturate the negatively charged nanoparticle surfaces thereby providing a plausible explanation to the observed biomarker concentration trends. These data and future work provide a rigorous experimental and theoretical evaluation of nanoparticle structure impacts their function as pseudostationary phases in separations and other applications.

TABLE OF CONTENTS

LIST OF TABLES

LIST OF FIGURES

CHAPTER 1

NANOMATERIAL SURFACE CHEMISTRY DESIGN FOR ADVANCEMENTS IN CAPILLARY ELECTROPHORESIS MODES

1.1 Introduction

Capillary electrophoresis[1-3] is an effective technique for the liquid-phase separation of molecules ranging from metal ions[4] to biomolecules such as DNA.[5, 6] Capillary electrophoresis separation modes[7] utilize small sample volumes (nanoliter injection volumes)[8] and high separation selectivities.[9] These electrically driven separations are achieved by applying a potential to charged molecules suspended in a solution. Electrophoretic separations of charged species occur because (1) anions and cations migrate in opposite directions toward electrodes of opposite charge and (2) similarly charged ions with varying Stokes radii exhibit different migration velocities (Figure 1.1).[10]

To separate neutral species, both pseudostationary (i.e. matrices which can either co-migrate with or migrate against the mobile phase) and stationary phases (i.e. non-moving matrices) are implemented to improve separation selectivity.[11] Terabe et. al.[12, 13] pioneered micellar electrokinetic chromatography, a technique which uses surfactants added to a separation buffer as a pseudostationary phase to improve the separation of neutral or like charged molecules. Above the critical micelle concentration, surfactant molecules form micelles with non-polar cores which are protected from the aqueous, mobile phase environment by polar head groups. Because neutral molecules partition between the micelle and mobile phases differently, separation selectivity improves vs. traditional capillary electrophoresis.

Unfortunately, some hydrophobic molecules can irreversibly partition into micelles thereby reducing separation selectivity and detection specificity.[14] As a result,

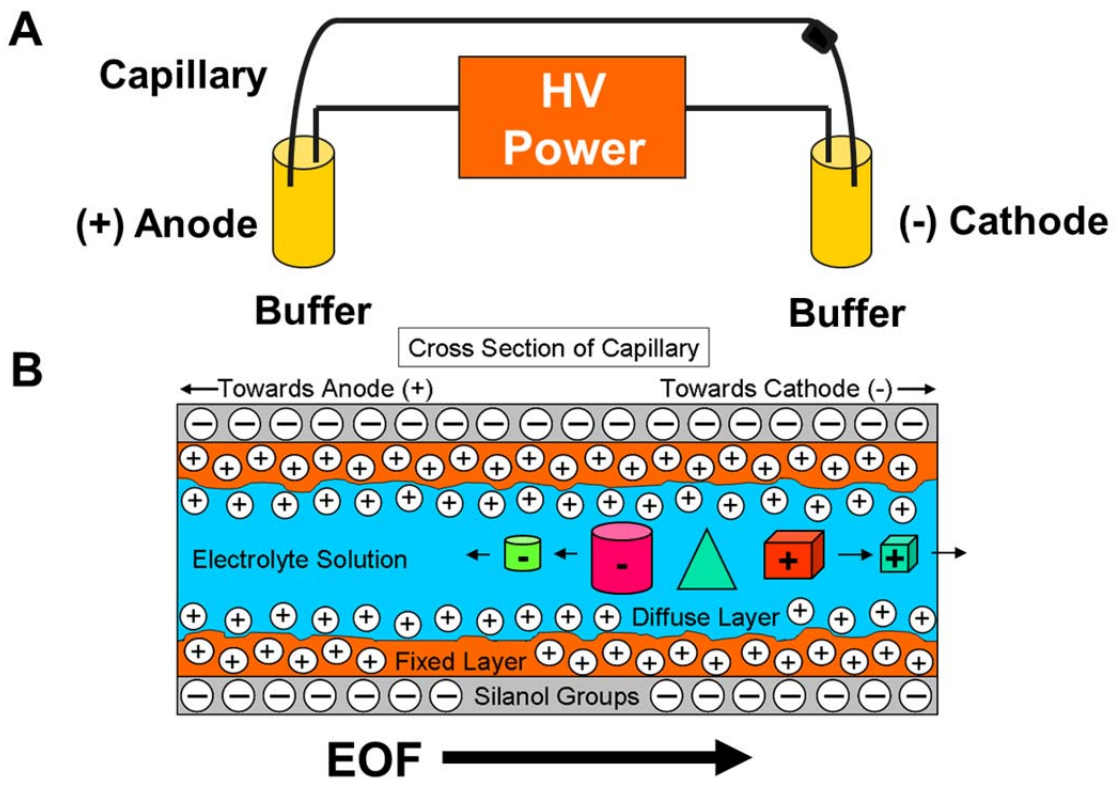

Figure 1.1 Capillary electrophoresis. (A) Schematic of the capillary electrophoresis setup which operates as a high voltage (HV Power) is applied between an anode (+) and cathode (-) as well as across a capillary. (B) Cross sectional view of the separation mechanisms of capillary electrophoresis. The direction of electrophoretic mobilities of analytes, electroosmotic flow (EOF), and charge states of the capillary wall are depicted.

additional organic modifiers can be added to the run buffer to decrease micelle–molecule affinity[15-17] or to change the separation mechanism.[18] Further efforts to improve capillary electrophoresis selectivity are summarized in Figure 1.2 and include capillary electrochromatography,[19] capillary gel electrochromatography,[20] and various capillary coatings.[21] Capillary electrochromatography, for instance, combines the high efficiency of an electrophoretic capillary electrophoresis separation with the selectivity of HPLC.[22, 23]

Pseudostationary or stationary phases in these separation techniques can include nanomaterials to further improve selectivity via three mechanisms.[24, 25] Nanomaterials possess ideal properties for integration into capillary electrophoresis as pseudostationary and stationary phases. For instance, these materials are inherently "small" - that is, contain at least one dimension less than 100 nm and can be included at low concentrations compared to traditional pseudostationary or stationary phases so that less than 1% of the total capillary volume is occupied by nanoparticles.[26] Second, nanomaterials exhibit inherently large surface area to volume ratios and novel size dependent chemical and physical properties.[27, 28]

Nanomaterials have been used in capillary electrophoresis separations for over two decades. In 1989, Wallingford demonstrated that a pseudostationary phase containing 20 nm (diameter) sulfonated polymer nanoparticles improved the separation of five catechol amines.[29] Although resolution in these experiments was poor, the usefulness of nanomaterials in separations and the importance of nanomaterial surface chemistry were clearly demonstrated. Recent advances in nanomaterials and capillary electrophoresis were summarized in several reviews and included: (1) separation effects of nanoparticle pseudostationary phases in capillary electrophoresis,[30, 31] (2) general uses of nanomaterials in separation science,[32] (3) extension and modification of micellar electrokinetic chromatography mathematics to nanoparticle pseudostationary and stationary phases in capillary electrophoresis,[33] (4) exploitation of nanomaterials for

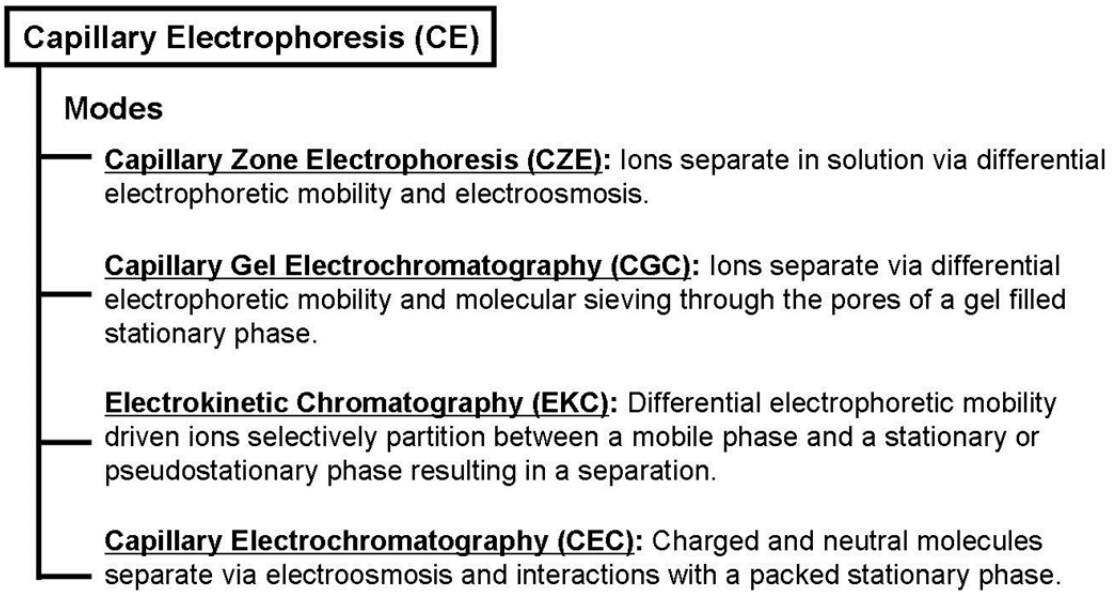

Figure 1.2 Classification of common capillary electrophoresis modes.

electrochemical detection in capillary electrophoresis,[34] and (5) electrophoretic separations of nanoparticles.[35]

Herein, the importance of nanomaterial stability and surface chemistry in various modes of capillary electrophoresis will be explored. In particular, the characterization of nanomaterial surface chemistry for customized use in separations, properties of nanomaterials inside the capillary, methods of nanomaterial introduction, and nanomaterial surface chemistry dependent molecular interactions will be discussed.

1.2 Classification of Nanomaterial Core Composition

Research funding for the development of applications which include nanomaterials is continually increasing. Globally, the total number of nanotechnology patent applications filed in 2008 exceeded 12,000 among the 15 largest national patent registries.[36] For the 2011 fiscal year, the United States National Nanotechnology Initiative (NNI) requested $1.8 billion for nanotechnology investments. Since 2001, the cumulative National Nanotechnology Initiative investment in nanotechnology, including the 2011 request, is ~$14 billion.[37] These substantial investments are directly related to applications involving the novel size dependent chemical and physical properties of these materials at the nanoscale where catalytic,[38] electrical,[39] magnetic,[40] mechanical,[41] optical,[42] and thermal[43] properties can deviate from those of bulk materials.

Although nanomaterial properties are primarily dictated by composition, shape, and size; precise control of nanomaterial surface chemistry is one of the critical characteristics for successful and reproducible nanomaterial applications. The large surface area to volume ratio of nanomaterials relative to the bulk increases the overall surface energy of the nanomaterial system thereby increasing reactivity. Surface chemistry influences the surface energy, functionality, and structural stability of nanomaterials;[44] and as a result, can be used to modulate surface energy thereby dictating the function of the nanomaterial in a bulk environment.[45] Additionally, because of the

high surface energy of nanomaterial systems, structural changes in nanoparticles are often observed,[46] and nanoparticle surface chemistry can lead to structurally stable or asymmetric nanoparticle architectures.[47]

Nanomaterials are ideally suited as pseudostationary and stationary phases in electrokinetic chromatography because of their small sizes, large surface area to volume ratios vs. bulk materials, and customizable surface chemistries. Nanoparticle surface chemistry plays two important roles in these separations. First, nanoparticle surface chemistry can modulate the separation mechanism(s) (i.e. effects the electroosmotic flow (EOF) or capillary surface) and dictate the elution order of targeted molecules.[24, 25, 48, 49] For instance, Kuo et. al.[48] observed an increase in effective capillary surface charge as silica nanoparticle concentration (diameter, d = 60 nm) increased in pH ~3 buffer.[48] As nanoparticle concentration increased (~50–180 nM), migration times of the analytes varied slightly as nanoparticles aggregated and/or interacted with the capillary wall. Nanomaterial instability was apparent from increased scattering intensities, unstable baselines, irreproducible separations (at elevated nanoparticle concentrations), and/or reduced detection sensitivities. Second, surface chemistry can dictate nanomaterial stability as a function of nanomaterial-nanomaterial interactions, interactions between the nanomaterial and the separation environment, and interactions between the target molecules and nanomaterial (Figure 1.3). Li et. al.[50] used citrate to both stabilize gold nanoparticles (d = 13 nm) and to extract indoleamines from solution prior to separations. The targeted molecules were hypothesized to interact with citrate on the nanoparticle surface via either van der Waals or electrostatic interactions. Limits of detection were improved by a factor of ~4000 for separations using nanoparticle extraction techniques vs. controls.

In both of these previous examples, surface chemistry dictated the role of nanomaterials in the separation. As a result, all properties of the nanostructures – including core composition, shape, size, and surface chemistry – must be considered

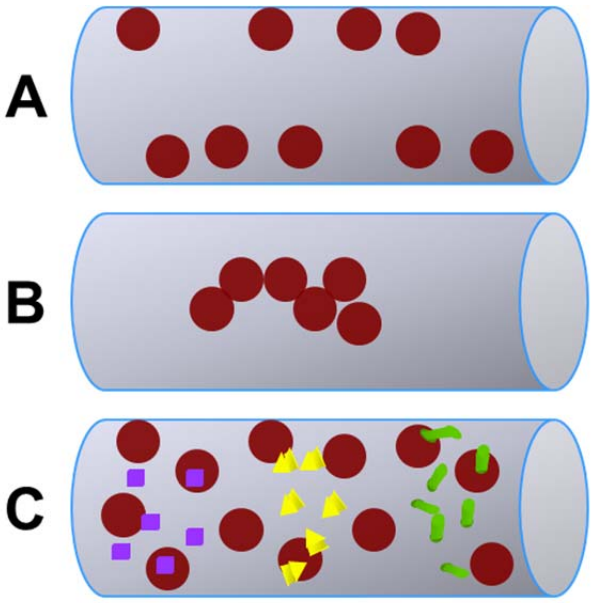

Figure 1.3 Nanomaterials impact separations via three mechanisms: (A) nanoparticle-capillary, (B) nanoparticle-nanoparticle, and (C) nanoparticle-analyte interactions. In all cases, the red spheres represent nanoparticles. In part C, the squares, triangles, and rods represent various analytes. Drawings are not to scale.

when evaluating the functionality of nanomaterials in separations. To simplify this discussion, we will classify nanostructures as containing either non-plasmonic or plasmonic cores.

1.2.1 Non-Plasmonic Nanomaterials

Non-plasmonic nanomaterials such as carbon nanotubes, latex/polymer nanoparticles, and silica nanoparticles exhibit novel properties which are routinely exploited as pseudostationary and stationary phases in various capillary based separation techniques. For instance, the high surface area to volume ratio and conductivity of carbon nanotubes encourages their use in separations.[51] Carbon nanotubes are one dimensional nanostructures and can be classified as either single-walled nanotubes (SWNTs) or multi-walled nanotubes (MWNTs) which are carbon nanotubes composed of one or multiple concentric cylinder(s), respectively.

Despite many promising investigations with the separation of peptides,[52] aniline derivatives,[53] and water soluble vitamins;[54] carbon nanotubes have experienced limited success in capillary electrophoresis. First, carbon nanotubes can interfere with detectable signals from both ultraviolet (UV) and laser induced fluorescence (LIF) detectors.[55] Second, raw carbon nanotubes are highly conductive[56] which can lead to irreproducible currents and separations. Third, the surface of a carbon nanotube is natively hydrophobic[57] which results in materials which are insoluble in water and commonly used separation buffers.

The conductivity and solubility of carbon nanotubes are influenced by surface chemistry. For instance, carbon nanotubes surfaces are oxidized by concentrated acids which yield hydroxyl, carbonyl, or carboxyl head groups rendering the normally non-polar carbon nanotubes water soluble.[58, 59] In 2003, Wang et. al.[60] used this strategy to successfully incorporate SWNTs as a pseudostationary phase in electrokinetic chromatography. Since that hallmark work, the utility of SWNTs in capillary

electrophoresis was further advanced by surfactant modified surface chemistries. Suárez et. al.[61] modified SWNTs (d = 0.7 – 1.2 nm) with sodium dodecyl sulfate (SDS) (CNT@SDS) which improved the separation resolution of three mixtures containing chlorophenols, non-steroidal anti-inflammatory drugs, or penicillin derivatives. Importantly, molecule-dependent separation selectivity was observed. When CNT@SDS were included in the separation buffer, the mobility of the penicillin derivative penicillin G decreased vs. no additives thereby suggesting a high affinity of penicillin G to the nanomaterial surface compared to the other penicillin derivatives.

Latex nanoparticles are also used to improve the separation of pharmaceutical compounds. Recently, Palmer et. al.[62] synthesized latex nanoparticles (d = 63 nm) for use as an electrokinetic chromatography pseudostationary phase. Unlike carbon nanotubes, latex nanoparticles contain native surface chemistries that are water soluble and cores which are not conductive. In comparison to traditional micelle electrokinetic chromatography separations, the average plate numbers for the separation of pharmaceutical compounds were slightly lower vs. controls (2×10^5 m^{-1}); however, selectivity increased dramatically for the nanoparticle-based experiments. Improvements in selectivity were attributed to surface chemistry; that is, increased hydrophobic interactions between the nanoparticle surface and target molecules.

Silica nanoparticles are also widely used to improve separations. Above pH ~2-3, the surface silanol groups of silica nanoparticles are negatively charged and under normal polarity conditions force the particles to migrate towards the anode (away from the detector). Fujimoto et. al.[63] exploited this native surface charge to selectively induce increased hydrogen bonding between the silica particle surface and polar organic molecules in solution. This approach was further used to improve the separation of aromatic acids[64] and anti-bacterial quinolones.[65]

Despite pseudostationary phases offering generally higher selectivity than if no pseudostationary phase is used, possible negative impacts on resolution are often

overlooked or underestimated when nanomaterials are used in capillary electrophoresis. For instance, while not technically nanomaterials (i.e. critical dimensions are larger than 100 nm), Bächmann et. al.[66] compared separation implications of 500 nm and 1.5 μm diameter silica particles to micelles used in micelle electrokinetic chromatography. The total band broadening (H_{total}) was defined as follows

$$H_{Total} = H_l + H_m + H_T + H_{ep(p)} + H_i \quad (1.1)$$

where H_l, H_m, H_T, $H_{ep(p)}$, and H_i are band broadening that arises from longitudinal diffusion, adsorption/desorption kinetics of molecules from a nanomaterial surface, diffusion caused by radial temperature gradients, interactions between nanomaterials and target analytes, and diffusion caused by flow profiles, respectively. This equation represents the first assessment of new contributions (both positive and negative) from particle additives in electrokinetic chromatography and clearly shows that band broadening can impact both separation selectivity and resolution for separations performed using these pseudostationary phases.

1.2.2 Plasmonic Nanomaterials

Plasmonic nanomaterials (i.e. gold, silver, composites, etc.) exhibit a size dependent property in which electrical and optical energy can be stored at their surfaces and is known as a localized surface plasmon resonance (LSPR).[67, 68] When metallic nanostructures possess critical size dimensions smaller than ~half the wavelength of incident light, the incident electromagnetic energy can be selectively absorbed and scattered by the nanoparticle which induces an oscillating electric field localized at the nanoparticle surface.[69]

The LSPR of noble metal nanoparticles is (1) experimentally measured using extinction spectroscopy (i.e. scattered and absorbed light);[70] (2) dependent on the distance matter is from the nanoparticle surface;[71] (3) theoretically predicted using Mie theory;[72] and (4) dictated by nanoparticle composition, shape, size, and local environment

surrounding the core nanomaterial.[72-74] Previously, LSPR spectroscopy was used to investigate a wide variety of chemical phenomena including biosensors for disease diagnosis,[75] cancer research,[76, 77] single molecule detection,[78] and surface enhanced Raman scattering (SERS).[79]

The influence of surface chemistry on the LSPR of gold nanoparticles (d ~ 13 nm) is demonstrated in Figure 1.4. Gold nanoparticles functionalized with citrate, thioctic acid, 11-mercaptoundecanoic acid, and 6-mercaptohexanoic acid display unique LSPR spectra with characteristic extinction maxima wavelengths (λ_{max}). While all four nanoparticle samples are statistically identical in terms of core sizes, the citrate stabilized gold nanoparticles contain the lowest molecular density of electrostatically bound surface molecules. Consequently, the extinction maximum of the sample is blue-shifted from the three covalently bound functional groups.

The nanostructures functionalized with carboxylic acid terminated self assembled monolayers (SAMs) exhibit surface chemistry dependent trends as well. As shown in Figure 1.4, the extinction maxima wavelength red shifts as molecular packing density and/or alkanethiol chain length increases. For example, it is well-established that thioctic acid binds to the gold nanoparticle surface via a disulfide ring,[80] whereas 11-mercaptoundecanoic acid and 6-mercaptohexanoic acid associate via a single dative thiol bond. The larger binding footprint of thioctic acid lowers its packing density vs. the other two SAMs.[81] Furthermore, because the LSPR wavelength increases as alkanethiol chain length increases,[82] nanoparticles functionalized with 11-mercaptoundecanoic acid show a lower energy extinction maximum than those modified with 6-mercaptohexanoic acid. These surface chemistry dependent properties can serve as an important monitoring parameter for understanding nanoparticle function and stability during electrically driven capillary based separations.

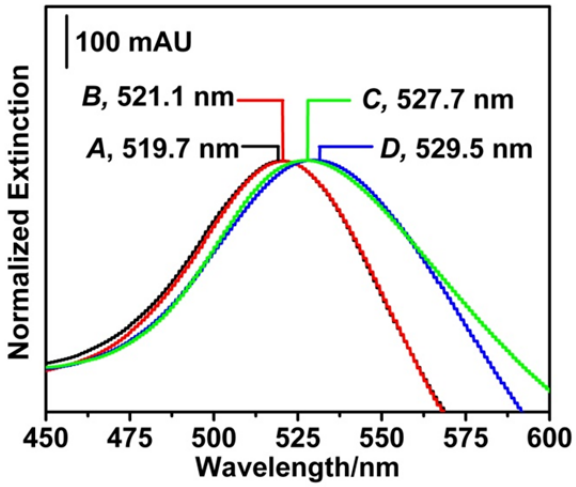

Figure 1.4 Normalized extinction spectra of gold nanoparticles stabilized with (A) citrate, λmax = 519.7 nm; (B) thioctic acid, λmax = 521.1 nm; (C) 6-mercaptohexanoic acid, λmax = 527.7 nm; and (D) 11-mercaptoundecanoic acid, λmax = 529.5 nm in aqueous solutions.

1.3 Bulk Nanomaterial Characterization

Nanomaterials exhibit surface chemistry-dependent properties which provide numerous advantages for their use in separation science. Nanomaterial stability and utility in capillary electrophoresis are dictated by their core composition and surface chemistry. As a result, thorough characterization of these properties as well as an evaluation of their shape, size, and reactivity are needed to establish a mechanistic understanding of how nanomaterials impact separations. If this information is not evaluated, the ability to use these materials reproducibly and to predict structure-function behavior is difficult/impossible.

1.3.1 Core vs. Surface Classification

Classification of nanomaterial pseudostationary and stationary phases in various capillary based separation techniques is summarized in Figure 1.5. The nanomaterials are divided into two categories: (1) nanomaterial cores modified by a capping agent (i.e. chemically distinct surface chemistry) that differs in composition from the core: "Core ≠ Surface" and (2) nanomaterial cores modified by native surface functionality of the nanomaterial: "Core = Surface" (i.e. core and surface are chemically identical but contain distinct atomic coordination numbers or a native oxide surface layer).

The chemical diversity of nanomaterials is complex as both core and surface chemistry composition dictates material properties and function (Figure 1.5). First, surface chemistry homogeneity impacts the stability of a nanostructure. For instance, charge density is often more homogeneous if capping agents are used vs. native functionalization (Core = Surface);[82, 83] however, non-specific molecular binding to "Core = Surface" structures is inherently less controllable than if a capping agent is used. Furthermore, in "Core ≠ Surface" nanostructures, molecules can form localized distributions with distinct molecular orientations and packing densities on a single nanoparticle which can then vary from nanoparticle to nanoparticle.[83] As a result,

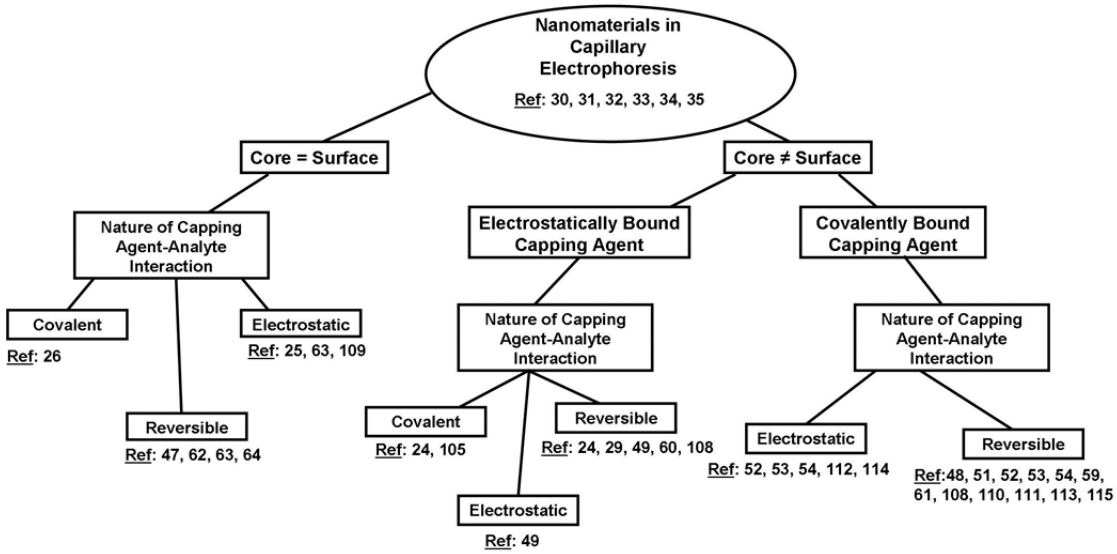

Figure 1.5 Classification of nanomaterials used in capillary electrophoresis. Nanomaterials are divided into two general categories: Core = Surface and Core ≠ Surface.

nanomaterial interactions can differ slightly from nanoparticle to nanoparticle thereby yielding an overall more heterogeneous nanomaterial phase than if the nanoparticle is stabilized by its native surface functionality (Core = Surface).

Finally, because initial surface functionalization is often used for both core stabilization and subsequent conjugation,[84-86] both head and tail groups on a surface ligand must be chosen for successful integration into applications. Because capping agents (Core ≠ Surface) offer more options for chemical flexibility and materials stability than native surface chemistries, this nanoparticle design approach is more often employed in capillary based separations. Both platforms (Core = Surface and Core ≠ Surface), however, yield nanoparticle surface chemistries that can be further exploited for their electrostatic, covalent, and/or reversible functionalities.

1.3.2 Nanomaterial Stability

Surface chemistry is particularly important in preventing uncontrolled nanomaterial aggregation in all applications including in separations. Because background electrolyte solutions are used in a wide range of ionic strengths and pHs, the stability of nanomaterial additives in capillary electrophoresis are dictated by the capping agent pK_a and composition. Classical Derjaguin, Landau, Verwey, and Overbeck (DLVO) theory[87] uses van der Waals (V_{vdW}, Equation 1.2) and electrostatic interactions (V_{elec}, Equation 1.3) to explain nanoparticle stability.[88]

$$V_{vdW} = -\frac{A}{6}k_B T\left[\frac{2R^2}{d^2-4R^2}+\frac{2R^2}{d^2}+\ln\left(\frac{d^2-4R^2}{d^2}\right)\right] \tag{1.2}$$

$$V_{elec} = 2\pi\varepsilon_r\varepsilon_0\psi_0^2 R k_B T \ln\left[1+\exp(-kd)\right] \tag{1.3}$$

$$\text{where} \quad k = \frac{1000e^2 N_A(2I)}{\varepsilon_R\varepsilon_O k_B T} \tag{1.4}$$

In these equations, A is the Hamaker constant, k_B is the Boltzman constant, T is the temperature, R is the radius of the particles, d is the separation distance between particles,

ε_r is the relative dielectric constant of the liquid, ε_o is the permittivity of the vacuum, ψ_0 is the zeta potential of the particles, *k* is the inverse Debye length, *e* is the elementary charge, N_A is Avagadro's number, and *I* is the ionic strength of the solution.

Classical DLVO theory models particles as infinitely flat solid surfaces with uniform surface charge densities. Furthermore, surface potential (i.e. zeta potential) is constant and uniform, and no chemical reactions occur between the solvent and the particles (i.e. solvent influences the solution dielectric constant only). Despite these assumptions, classical DLVO theory is widely accepted as a plausible model for the total interactions (V_{total}) between two electrostatically stabilized particles in solution as follows:

$$V_{total} = V_{vdW} + V_{elec} \tag{1.5}$$

Using this classical DLVO model, the total interactions between 13 nm diameter Au nanoparticles stabilized with thioctic acid in 30 mM ionic strength buffer is shown in Figure 1.6. In these conditions, electrostatic repulsive forces are minimized at separation distances less that (~3 nm). As a result, when these particles interact at this and shorter distances, uncontrolled aggregation occurs.

1.3.3 Nanomaterial Concentration

While numerous techniques are routinely used to characterize noble metal nanoparticles, one of the most widely used techniques for estimating plasmonic nanoparticle concentration exploits the LSPR. For instance, gold nanoparticle concentration can be assessed using a standard estimation model[89] where LSPR spectroscopy and transmission electron microscopy (TEM) data are utilized. In addition to estimating nanoparticle concentration, LSPR spectral changes for noble metal nanoparticles[45, 90] can indicate nanoparticle stability and surface chemistry properties.

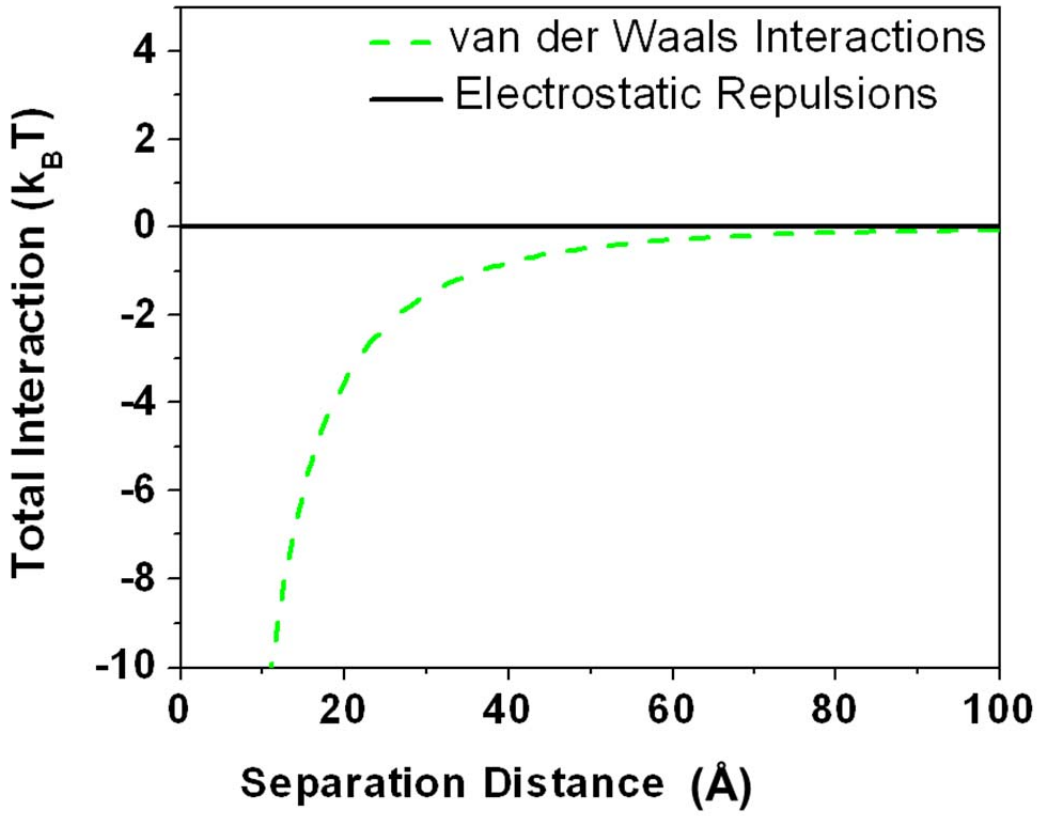

Figure 1.6 Classic DLVO theory model for the potential energy interaction as a function of distance for Au@TA (d =13 nM, ζ potential = -18.7 mV) nanoparticles in a 30 mM ionic strength aqueous solution. Under these conditions, classic DLVO predicts agglomeration of Au@TA nanoparticles at separations distances of ~ 3 nm.

Conversely, in cases where LSPR data are neither available nor exploited, nanomaterial concentration can be reported as a weight/weight (w/w) or weight/volume (w/v) ratio. These methods depend on measuring and suspending a known initial dry weight of a nanomaterial in solution. If an average nanoparticle size is reported, nanoparticle concentration can be estimated. Alternatively, nanomaterial concentration can be calculated from the amount of starting reagents used. The morphology of the nanomaterials is then used to estimate concentration.

1.3.4 Nanomaterial Surface Charge

Nanomaterial stability and their potential usefulness as pseudostationary and/or stationary phases in capillary based separation techniques are dictated by surface chemistry and charge. Zeta potential, a technique that measures electric potential differences between the slipping plane of a stationary fluid layer on a nanoparticle surface,[91] can be used to quantify surface charge in a fixed buffer composition, concentration, ionic strength, and pH environment. In general, a "high" zeta potential (> 25 mV or < -25 mV) indicates stable nanostructures. As the zeta potential approaches "0" or the point of zero charge,[93, 94] the attraction between nanomaterials exceeds the repulsive forces between the structures resulting in agglomeration.[92] As a result, this solution-dependent surface charge measurement is useful in predicting the stability and function of nanomaterials in various environments.

1.3.5 Surface Functionality

While both LSPR and zeta potential data yield important information regarding the composition, concentration, and effective charge of nanomaterials; more precise information regarding molecule orientation must be garnered using other techniques such as X-ray photoelectron spectroscopy (XPS)[93, 94] and NMR.[95, 96]

While traditionally used as an organic chemistry characterization tool, NMR can provide detailed information regarding the interactions between[97, 98] as well as orientation

and composition of[96, 99] SAMs on nanomaterials. For instance, Schmitt et. al. used solid state ^{13}C NMR to investigate the effects of SAM terminal groups on ~3 nm gold nanoparticles.[100] The conformational ordering of 8-mercapto-1-octanoic acid and 16-hydroxyhexadecanethiol was dictated by the degree of (1) van der Waals interactions between the alkanethiol chains and (2) hydrogen bonding between terminal groups of neighboring molecules on individual nanoparticles. Carboxylic acid terminated SAMs exhibited the most conformational order followed by hydroxylated and methyl terminated functionalities.

1.4 Incorporating Nanomaterials in Capillary Electrophoresis

Manipulation of nanomaterial pseudostationary and stationary phase properties (i.e. core composition, shape, size, and surface chemistry) inherently impacts their function in capillary based separation techniques. Once the nanomaterial core and surface compositions are selected and evaluated, the method in which the nanomaterials are introduced into a capillary is the next critical parameter to realize for both stable and reproducible applications. Three methods are typically used to introduce nanomaterials as pseudostationary and stationary phases into a capillary: continuous full filling,[101-104] partial filling,[102, 105, 106] and capillary coating (Figure 1.7).[24, 25, 101, 104, 107-109]

The first deliberate use of nanomaterials[29] in electrokinetic chromatography implemented continuous full filling methods where the nanomaterials were included in the background electrolyte solution. Target molecules interacted with the nanomaterials throughout the separation. Partial filling techniques, where discrete nanomaterial plugs are injected into a capillary prior to the sample matrix, were successfully used to generate discontinuous nanomaterial pseudostationary phases. Because target molecules possessed greater mobilities than the nanoparticle pseudostationary phase, the molecules eluted through the nanomaterial pseudostationary phase thereby influencing separation

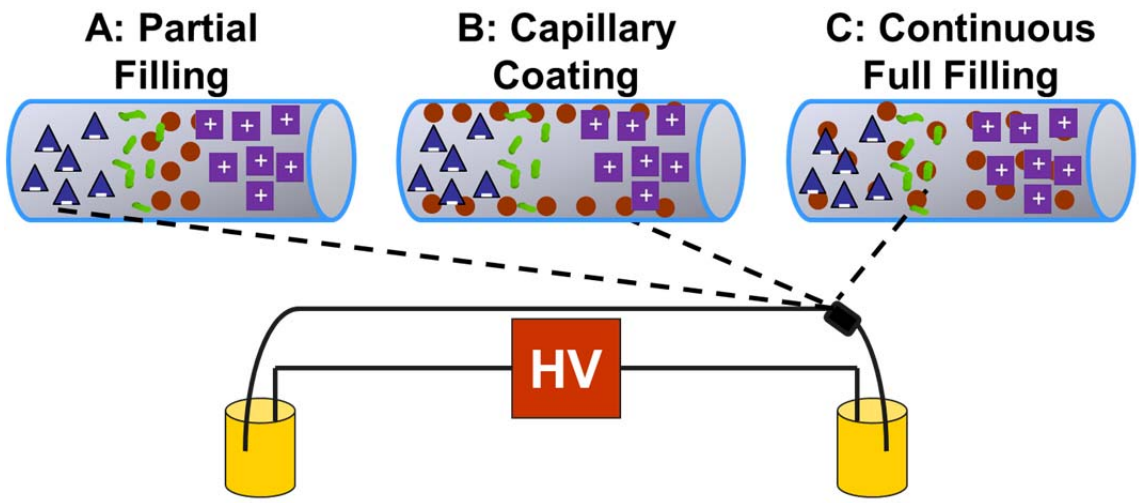

Figure 1.7 Methods for integrating nanomaterials into capillary electrophoresis. (A) Partial filling techniques utilize nanomaterials as a discreet plug. (B) Capillary coating approaches utilize the adherence of nanoparticles to the capillary surface. (C) Continuous full filling methods include nanomaterials in the separation buffer. In all cases, analytes interact with the nanomaterials as they pass through the capillary. Drawing is not to scale.

selectivity.[102, 105, 106] Regardless of whether the nanomaterials are injected into the capillary as a discrete plug or continuously, the method of injection (hydrodynamic or electrokinetic) can bias the nanomaterial concentration and drastically impact the nanomaterial function in a separation. Finally, capillary coating methods utilize nanomaterials through capillary modification via covalent and/or electrostatic interactions.[24, 25] In these cases, the nanomaterial is modeled as a stationary phase.

In all nanomaterial integration techniques, optimization of separation conditions is required for reproducible separation results. Control (i.e. lack of control or understanding) of nanomaterial concentration can adversely impact separations by (1) causing instability in the system, (2) interfering with detection by generating an inconsistent background signal, (3) inducing conductivity differences within the capillary, and (4) increasing backpressure within the capillary. In addition to traditional capillary based separation interactions, nanomaterials can interact with target molecules, the capillary wall, and/or other nanomaterials during a separation.

1.5 Conclusions, Future Outlook, and Thesis Outline

Nanomaterials are widely used as pseudostationary and stationary phases in electrically driven capillary separations. Nanomaterial advantages are numerous and include small/tunable sizes, core composition variations, flexible injection/introduction methods in separation techniques, and diverse surface chemistry options. Nanomaterials, however, exhibit inherently large surface energies which can change upon aggregation and/or surface chemistry modification, and as a result, yield unpredictable function in separations. Furthermore, nanomaterials can adversely impact separations by changing buffer conductivity, viscosity, and pH which requires a careful balance in nanoparticle stability and separation optimization. Finally, nanomaterials can complicate detection by varying background signals.

A unified mechanism which predicts the structure-function relationship of a nanomaterial phase to separation effects is complex, dynamic, and often not thoroughly understood. In this dissertation, a rigorous evaluation of nanoparticle core and surface properties will be used to develop a better mechanistic understanding of nanomaterial function in capillary electrophoresis. Initially, the optimization and characterization of gold nanoparticles with tailored surface chemistries will be described in Chapters 2 and 3. Specifically, Chapter 2 will focus on the synthesis and characterization of thioctic acid functionalized gold nanoparticles. Chapter 3 will systematically investigate the surface chemistry on and morphology of gold nanoparticles functionalized with thioctic acid, 6-mercaptohexanoic acid, and 11-mercaptoundecanoic acid. Next, Chapter 4 will focus on applications of gold nanoparticles as pseudostationary phases in capillary electrophoresis. Gold nanoparticles functionalized with mixed self-assembled monolayers composed of thioctic acid and either 6-mercaptohexanoic acid or 6-aminohexanethiol will be injected as discrete plugs into the capillary to affect the separation of possible Parkinson's disease biomarkers. Chapter 5 will investigate the mechanism that functionalized gold nanoparticle pseudostationary phases exhibit during capillary electrophoresis separations. Nanoparticle influences on current as a result of nanoparticle surface chemistry in the capillary will be evaluated. Distinct nanoparticle surface chemistries will be shown to uniquely interact with the capillary and other nanoparticles thereby impacting separation conditions. Chapter 6 examines nanoparticle concentration and surface chemistry effects on the separation of hypothesized Parkinson's disease biomarkers. The effects of surface ligand composition and coverage will be used to systematically evaluate separation efficiency, resolution, and selectivity. These data will be critical in designing pseudostationary phases for use in capillary electrophoresis separations. Chapter 7 will present the conclusions and future directions of nanomaterial pseudostationary and stationary phases in separations.

CHAPTER 2
SALT-MEDIATED SELF ASSEMBLY OF THIOCTIC ACID ON GOLD NANOPARTICLES

2.1 Introduction

Surface modification via self assembled monolayers (SAMs) is revolutionizing how surfaces and interfaces are modified for applications in biosensors, biotechnology, chemical sensors, and molecular electronics.[110-120] A wide variety of ligands (i.e. amine, carboxylate, isocyanide, phosphine, and thiol)[121, 122] form SAMs on gold films[110] and colloidal particles;[69, 75, 84, 114, 123] however, thiol/disulfide surface attachment groups are widely employed because of the strong bond that forms between gold and sulfur.[110] The stability of solution-phase nanoparticles can be improved with SAMs thereby increasing their usefulness in biology, catalysis, and nanotechnology.[69, 114, 124-126]

Reproducible utilization of thiol functionalized gold nanoparticles in any application depends on the reliable assembly of SAMs on their surfaces. Alkanethiol chains composed of more than 10 carbon atoms produce SAMs which are more highly ordered and oriented with increased molecular packing densities than shorter chains.[127, 128] These SAMs, however, generally contain at least three types of defect sites: pinholes, gauche defects in alkyl chains,[129] and collapsed-site defects which arise from (1) imperfect adsorption of alkanethiols during the self assembly process; (2) thermal and tilt-order driven chain dynamics; and (3) loss of thiols during rinsing, storage, and use.[127, 130] For thiols on flat gold surfaces, the fraction of these defect sites to the total surface area is estimated at ~6-10%.[131] While the influence of alkanethiol chain length,[127] anchoring group,[132] chemical composition,[133] immersion time,[134] and substrate topography was previously investigated for nanoparticles;[127] no evaluation of defect sites on solution-phase nanoparticles and implications thereof was performed.

In these studies, we will investigate how the ionic strength of the dielectric medium impacts the self assembly of thioctic acid on the surface of gold (Au@TA) nanoparticles. Specifically, an increase in NaCl concentration during alkanethiol incubation increases the packing density of thioctic acid SAMs on solution-phase gold nanoparticles by 17% while their stability increases by approximately the same magnitude vs. control studies. During SAM modification, the core size and optical properties of the gold nanoparticles will be shown to remain statistically unchanged as revealed by transmission electron microscopy (TEM) and extinction spectroscopy, respectively. In contrast, zeta potential and X-ray photoelectron spectroscopy (XPS) will reveal that the effective surface charge and sulfur to gold atomic ratio of functionalized gold nanoparticles, respectively, vary systematically then saturate as the estimated SAM packing density equilibrates. Significantly, nanoparticles functionalized in the presence of salt will be shown to be approximately twice as stable as nanoparticles prepared in the absence of salt. These data support that SAM packing density increases as a function of increasing NaCl concentration, thereby suggesting that the density of pinhole and/or collapsed-site defects on the nanoparticle surface are reduced. Better control in alkanethiol packing density as a result of a salt-mediated SAM assembly on gold nanoparticles will be fundamental in achieving reproducible gold nanoparticle covalent functionalization and their subsequent utility in applications and new technologies.

2.2 Experimental

2.2.1 Preparation of Thioctic Acid Functionalized Gold Nanoparticles

Gold (III) chloride trihydrate ($HAuCl_4$), trisodium citrate dihydrate (citrate), thioctic acid, boric acid, and sodium tetraborate decahydrate were purchased from Sigma Aldrich (St. Louis, MO). Sodium chloride (NaCl), sodium hydroxide (NaOH), ethanol, hydrochloric acid (HCl), and nitric acid (HNO_3) were purchased from Fisher Scientific

(Pittsburg, PA). Nanopure water (18.2 MΩ cm^{-1}) was obtained from a Barnstead Nanopure System and used for all experiments. All glassware used in the preparation and storage of Au nanoparticles was cleaned with aqua regia (3:1 $HCl:HNO_3$), rinsed with water, and oven dried. Citrate stabilized gold (Au@citrate) nanoparticles were prepared according to previous reports.[135] Briefly, a 200 mL aqueous solution of 1 mM $HAuCl_4$ was refluxed while stirring vigorously. Next, 20 mL of 38.8 mM citrate was quickly added, refluxed for 10 minutes, and allowed to cool to room temperature while stirring. The resulting gold nanoparticle diameter is $11.6_9 \pm 0.9_8$ nm as determined by TEM and an extinction maximum, λ_{max} = 518 nm.

Au@TA nanoparticles were prepared by modifying a previously published method.[106] First, Au@citrate nanoparticles were filtered (0.45 μm filter) (Whatman, Middlesex, UK) and centrifuged (Eppendorf – Model centrifuge 5424, Germany; 11,500 RPM (8797 x g) for 40 minutes) to remove large aggregates and excess citrate, respectively. The resulting pellet was suspended in pH adjusted water (pH = 11 with 1 M NaOH) to a nanoparticle concentration of 10 nM according to the method described by Haiss.[89] Thioctic acid functionalization was carried out by adding 10 mM thioctic acid (100 μL in ethanol) to 10 mL aliquots of 10 nM Au@citrate nanoparticles. This solution was allowed to stir in the dark for at least 16 hrs at 20°C.

During the slow addition of salt, a 2 M NaCl solution was added drop-wise to Au@TA nanoparticle solutions until the salt concentration reached 4 mM. This solution was allowed to stir (slowly) for 8 hours. The NaCl concentration was then increased to 8 and 16 mM in similar subsequent steps. After each of these incubation periods, excess thioctic acid and NaCl were removed by centrifugation at 11,500 RPM (8,797 x g) for 40 minutes. In order to investigate the effect of time on the samples incubated in the presence of 16 mM NaCl, the samples were allowed to equilibrate for an additional 32 hours. Prior to measurements, these samples were centrifuged at 11,500 RPM (8,797 x g) for 40 minutes. Following removal of the supernatant, the nanoparticle pellet was

resuspended in pH adjusted water (pH = 11). This rinsing process was repeated three times. Samples in which no salt was added but allowed to incubate in thioctic acid solutions were used as a control.

2.2.2 Transmission Electron Microscopy (TEM)

The homogeneity and diameter of the nanoparticles were characterized using TEM (JEOL JEM-1230). Samples were prepared by applying 30 μL of a diluted nanoparticle solution (50% mixture in ethanol) to a carbon Formvar coated copper grid (400 mesh, Electron Microscopy Sciences, Hatfield, PA). Excess solution was removed with filter paper, and the sample was allowed to dry. The resulting images were analyzed using Image Pro Analyzer, and at least 100 nanoparticles were evaluated per sample.

2.2.3 ^{1}H NMR Spectroscopy

^{1}H NMR and two dimensional correlation spectroscopy (2D COSY) spectra were recorded on a Bruker 600 mHz spectrometer (Bruker Biospin Corp., Billerica, MA). Samples were prepared by centrifugation at 15,000 RPM (14,967 x g) for 30 minutes. After the supernatant was removed, the nanoparticles were resuspended in pH adjusted water (pH = 11) (repeated three times). Next, the samples were transferred to a lyophilizing vessel, flash frozen with liquid N_2, lyophilized to remove water, and resuspended in D_2O to a 50 nM nanoparticle concentration. Spectra were analyzed using Topspin and Nuts. Chemical shifts were referenced to the residual shifts of the deuterated solvent. 2D COSY spectra were acquired using standard pulse sequences optimized to the individual parameters of each sample. These data were used for proton assignments in the 1D spectra.

2.2.4 Extinction Spectroscopy

Extinction spectra of Au@TA nanoparticles were acquired using an UV-visible spectrometer (Ocean Optics HR 4000) configured in transmission geometry. Before

acquiring spectra, samples were centrifuged at 11,500 RPM (8,797 x g) for 40 minutes and redispersed in 20 mM sodium borate buffer (pH = 9). The solution was diluted to a final nanoparticle concentration of 2 nM using the same buffer. All spectra were collected in disposable methacrylate cuvettes (path length = 0.5 cm) using the following parameters: integration time = 20 msec, average = 20 scans, and boxcar = 10.

2.2.5 Zeta Potential Measurements

Effective gold nanoparticle surface charges (zeta potential) were determined from their electrophoretic mobility at 25°C using a Malvern Zetasizer (Worcestershire, UK). Au@TA nanoparticle samples were centrifuged at 11,500 RPM (8,797 x g) for 40 minutes, redispersed in 20 mM sodium borate buffer (pH = 9), and diluted to a final concentration of 2 nM. Monomodal acquisitions and fits according to the Smoluchowski theory were used. Measurements were performed in triplicate, and error bars represent the standard deviation of these data.

2.2.6 X-Ray Photoelectron Spectroscopy (XPS)

XPS measurements were collected using a Kratos Axis Ultra Spectrometer with a monochromatic Al K_α X-ray source as described previously.[136] Briefly, a 160 eV pass energy, 1 eV step size, 200 ms dwell time, and ~700 μm x 300 μm X-ray spot size were used for a survey scan (range = 1200 – -5 eV). Region scans (O 1s, C 1s, S 2p, and Au 4f) exhibited typical band widths of 20 - 50 eV, 20 eV pass energies, 0.1 eV step sizes, and 1 sec dwell times. All spectra were analyzed using CasaXPS and were charge-calibrated with respect to the adventitious C 1s peak at 285.0 eV. The S 2p peak of thioctic acid was peak fitted using the S 2p doublet with a 2:1 area ratio and an energy difference of 1.2 eV. A Shirley background was used to subtract the inelastic background from the S 2p and Au 4f signals. The curves were fit using a Gaussian/Lorentzian (GL(30)) lineshape. To account for differences in nanoparticle concentration in sample

spots, the S 2p areas were normalized using the Au 4f area. Two areas were analyzed per sample. Error bars represent the standard deviation of these data.

2.2.7 Nanoparticle Flocculation Measurements

Au@TA nanoparticle solutions (10 nM) were prepared in pH 11 water. To monitor flocculation, gold nanoparticles were incubated for 72 hours in the absence and presence of salt, centrifuged, and redispersed in 3.0 mS cm^{-1} sodium acetate or phosphate buffer (pH 5.5 or 12, respectively). The solution was stirred, and extinction spectra were collected every 2 seconds. The data were baseline subtracted using an in-house written MatLab program. Briefly, LSPR spectra collected in pH 12 buffer were aligned to 0 AU at 800 nm. A normalization factor was determined for these spectra and then applied to all other spectra for that sample. Integrated areas were calculated from the normalized spectra (from 575 – 800 nm) collected in pH 5.5 buffer and plotted as a function of time.

2.3 Results and Discussion

2.3.1 Optical Characterization of Au@TA Nanoparticles

Figure 2.1 depicts the self assembly of thioctic acid on Au@TA nanoparticles. After initially functionalizing these nanostructures with thioctic acid and allowing them to incubate for 16 hours, NaCl is added incrementally in 8 hour incubation steps to promote thioctic acid self assembly. Au@TA nanoparticles remain stable up to 16 mM salt concentrations. Above this concentration, Au@TA nanoparticles begin to aggregate as indicated by the growth of a characteristic low energy (~620 nm) band (data not shown). Because each salt containing gold nanoparticle aliquot was allowed to incubate for 8 hours, time control assays (i.e. equal incubation times in the absence of salt) are included. Structural analysis of these nanostructures via TEM (Figure 2.2) reveals that average nanoparticle size does not change significantly throughout the SAM formation process (in the presence or the absence of salt). A representative TEM micrograph of

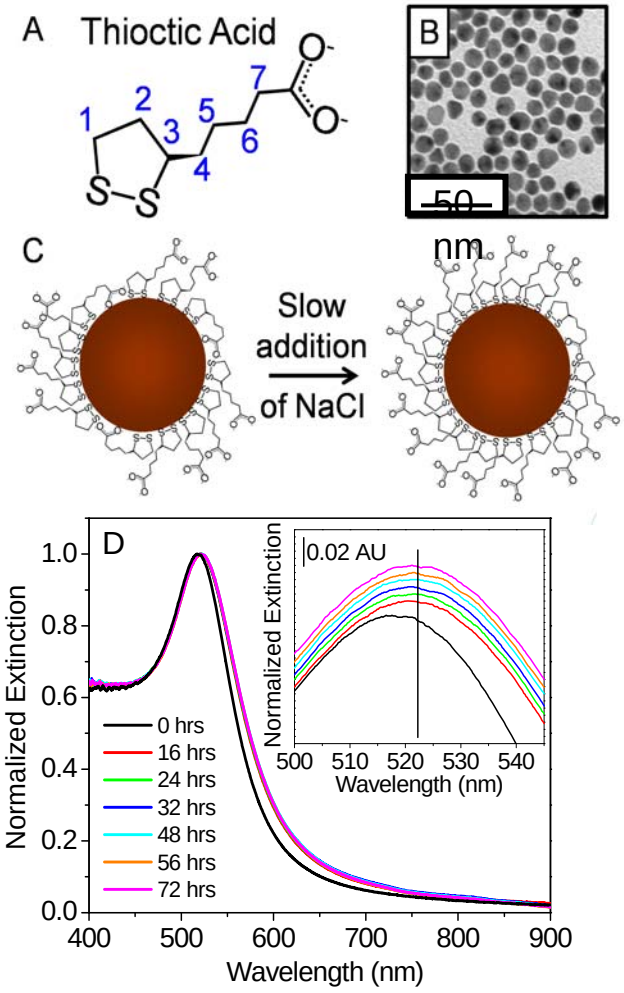

Figure 2.1 Slow addition of NaCl to Au@TA nanoparticles. (A) Structure and proton assignments used for thioctic acid. (B) Representative TEM image of Au@TA nanoparticles (average diameter, $d = 11.6_1 \pm 0.9_8$, N = 311). (C) Schematic of the proposed mechanism for thioctic acid packing with the slow addition of NaCl. (D) Extinction spectra of Au@TA nanoparticles equilibrated for 0 - 72 hours. Inset shows an enlarged view of the extinction maxima (λ_{max} = 518 nm and ~521 nm for 0 and 16 – 72 hours, respectively) in 20 mM sodium borate buffer (pH = 9).

Au@TA nanostructures is shown in Figure 2.1B. As expected, Au@TA nanoparticles are spherical and exhibit a mean diameter of $11.6_1 \pm 0.9_8$ nm.

Noble metal nanoparticles (i.e. copper, gold, silver, etc.) exhibit strong extinction properties in the visible region of the electromagnetic spectrum[137-142] which are sensitive to changes in nanoparticle shape, size, stability, and local dielectric environment (i.e. the surrounding medium and/or surface chemistry).[143, 144] These localized surface plasmon resonance (LSPR) spectra arise when the incident electromagnetic energy is in resonance with the collective oscillation of the conduction electrons in the nanoparticles resulting in the selective absorption/scattering of light and the generation of large electric fields on nanoparticle surfaces.[145] Figure 2.1D shows the LSPR spectra of citrate stabilized gold (Au@citrate) (0 hours) and Au@TA nanoparticles after being functionalized in thioctic acid at varying salt concentrations and equilibration times. To ensure that bulk refractive index changes are not impacting these sensitive optical properties, the nanoparticles were washed and redispersed in 20 mM borate buffer (pH 9) prior to each measurement. The gold nanoparticles exhibit an extinction maximum (λ_{max}) at ~518 prior to functionalization. After exchange with thioctic acid, the λ_{max} shifts to ~521 nm. This value does not change significantly with increased incubation time and is indicative of stable, electromagnetically isolated nanostructures. Because thioctic acid chemisorbs to the surface of gold nanoparticles, the observed optical properties are consistent with an increase in local refractive index upon thioctic acid conjugation.

2.3.2 Surface Charge Characterization of Au@TA Nanoparticles

To verify that salt concentration is influencing the surface coverage of thioctic acid on the Au nanoparticle surfaces, zeta potential measurements (in mV) were carried out as a function of time both in the presence and absence of salt. Figure 2.3 summarizes these average (effective) surface charge data. For clarity, both control (no NaCl) and salt

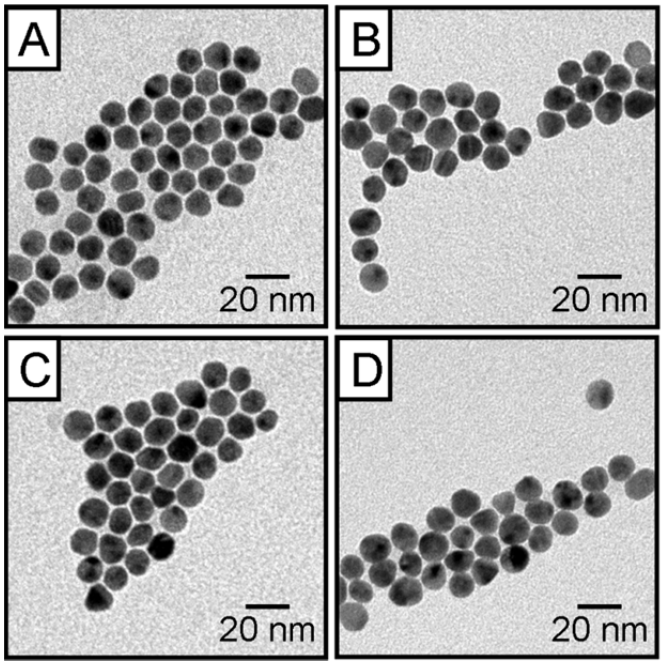

Figure 2.2 Representative TEM images of Au@TA nanoparticles incubated for (A) 16 (no NaCl), (B) 56 (no NaCl), (C) 56 (16 mM NaCl), and (D) 72 (16 mM NaCl) hours exhibited mean diameters $11.6_9 \pm 0.9_8$, $12.0_6 \pm 0.8_1$, $11.6_1 \pm 0.9_8$, and $12.0_0 \pm 0.8_6$ nm, respectively.

(with NaCl) data are plotted versus time (i.e. the incubation time for gold nanoparticles in the thioctic acid solutions). It should be noted that the surface pK_a for carboxylic acid terminated SAMs are typically more basic than solution values which range from 4.5 - 7.[80, 106] For all Au@TA nanoparticle samples studied, the surface potentials exhibit a negative value at pH = 9 which arises from the deprotonation of terminal carboxyl acid groups on thioctic acid bound to the nanostructures.

Previous studies revealed that carboxylic acid functionalized gold nanoparticles exhibited negative zeta potential values that ranged from 36 – 60 mV (pH 9).[106] As shown in Figure 2.3, the zeta potential of Au@TA nanoparticles are dependent on both time and salt addition. In the absence of NaCl, the negative zeta potential magnitudes range from 23.9 to 30.1 mV, a change of 6.2 mV, as incubation time increases. Similar trends are observed for Au@TA nanoparticles prepared in the presence of NaCl; however, the negative surface potentials range from 23.9 to 33.8 mV, a change of 9.9 mV, a change that is 60% greater vs. controls.

To further investigate the differences between ligand exchange reactions in the absence and presence of salt, the zeta potential curves are analyzed using an exponential fit. From this fit, a (theoretical) saturated zeta potential is calculated at -30.4 and -34.5 mV for Au@TA nanoparticles incubated in the absence and presence of NaCl, respectively. Although the zeta potential magnitude increases with increasing incubation time, the addition of NaCl during thioctic acid functionalization produce more negative zeta potential magnitude (vs. controls). These surface charge differences support that molecular surface coverage (i.e. thioctic acid packing density) increases on gold nanoparticles when salt is present during functionalization versus control studies.

2.3.3 ^{1}H NMR Analysis of Au@TA Nanoparticles

Recently, ^{13}C and ^{1}H NMR were applied to characterize molecules adsorbed to the surface of nanomaterials.[146] Four significant spectral characteristics are generally

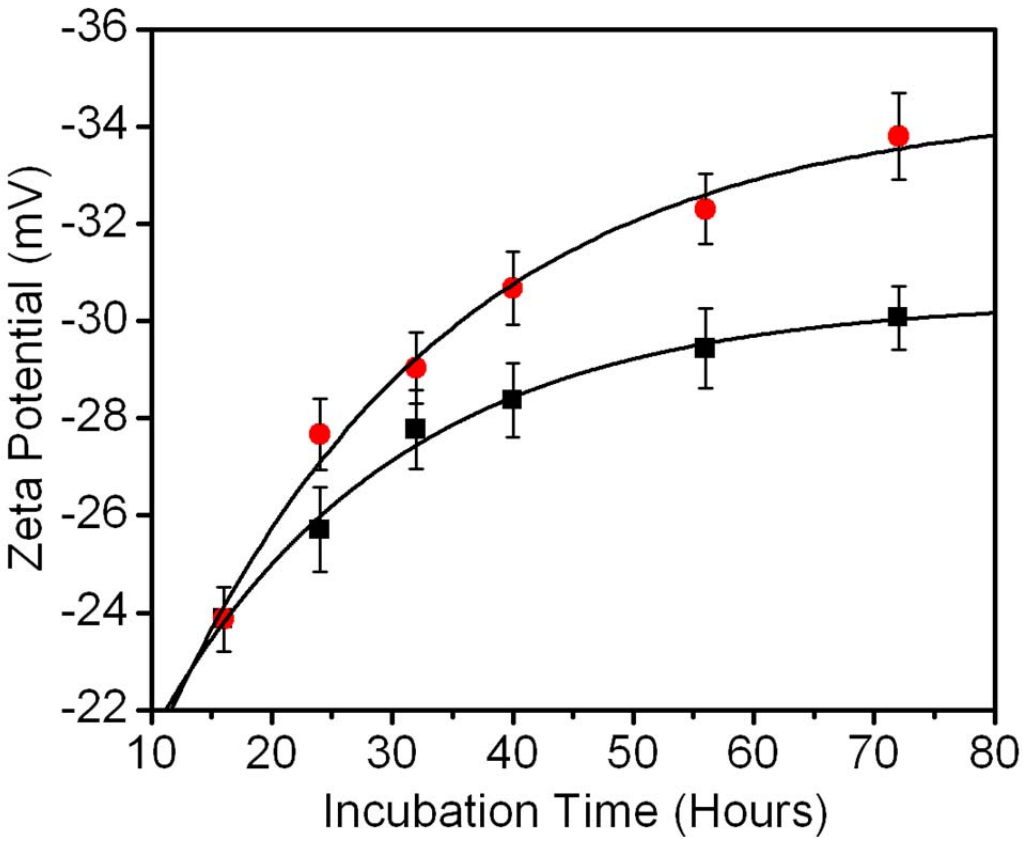

Figure 2.3 Zeta potential measurements for 2 nM Au@TA nanoparticles prepared in the (●) presence and (■) absence of NaCl. Nanoparticles were rinsed and suspended in 20 mM sodium borate buffer (pH = 9) prior to each measurement. The solid lines represent exponential fits for the Zeta Potential vs. Incubation Time data: "No NaCl" $y = -14.7_5e^{-x/20.0} - 30.4_3$ and "With NaCl" $y = -20.5_2e^{-x/23.5} - 34.5_0$.

observed: (1) peak broadening;[83] (2) free ligand signatures superimposed on the surface-bound ligand spectrum;[147] (3) chemical shift differences between free ligand and surface-bound ligands;[147] and (4) magnetic field variations for the ligand which depends on the distance between the proton and the nanomaterial surface,[99] as well as with nanoparticle composition and size.[40, 148] Similar observations are made for Au@TA nanoparticles. ^{1}H NMR is used to qualitatively evaluate the orientation of thioctic acid on the surface of gold nanoparticles. 2D COSY studies (Figure 2.4A) were performed to determine the proton assignments shown in Figure 2.1A. In comparison to free ligand studies, spectral features for thioctic acid are significantly broadened when bound to gold nanoparticles (Figure 2.4B) thereby verifying that the molecules sampled are chemisorbed to the nanoparticle surface and not free in solution. This is an important spectral observation given that no superimposed bands are observed in these spectra.

Table 1 summaries the average chemical shift data for thioctic acid free in solution (no nanoparticles) and bound to nanoparticle surfaces. At least four spectral features are notable. First, the methylene protons on carbons 7 and 6 exhibit no significant chemical shift differences between free and surface bound ligands. This suggests that these protons are farthest from the nanoparticle surface and possess the highest degree of entropy or solution-like behavior relative to the other protons.[98, 100]

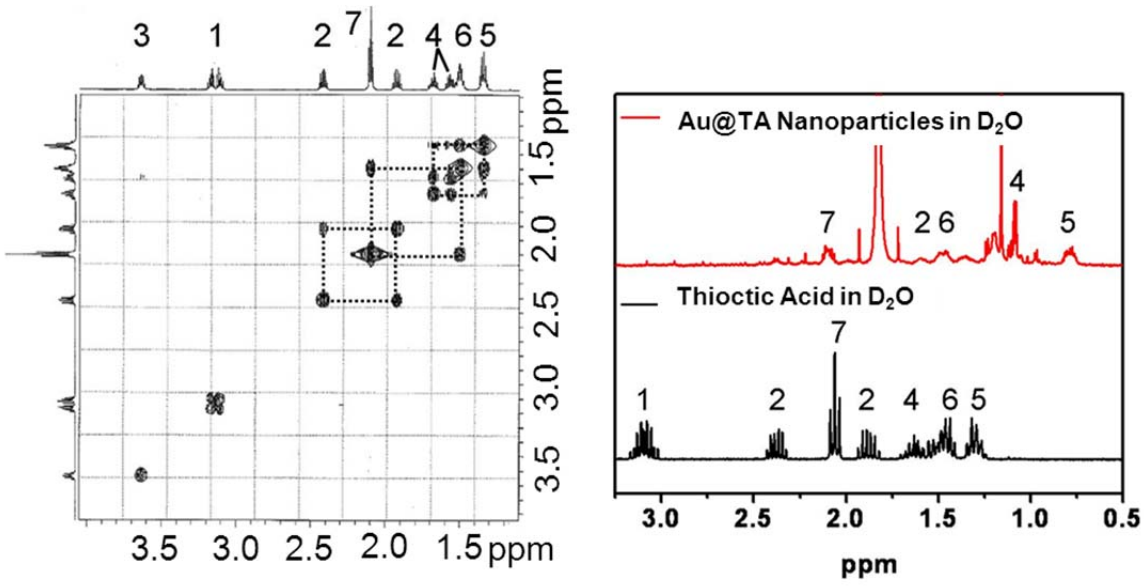

Figure 2.4 ^{1}H NMR characterization (A) 2D COSY ^{1}H NMR spectrum of 10 mM thioctic acid dissolved in D_2O. (B) ^{1}H NMR spectra of 10 mM thioctic acid and 50 nM Au@TA nanoparticle in D_2O. The numbers represent proton assignments for thioctic acid.

Table 2.1 ^{1}H NMR Chemical Shifts, δ in ppm for Thioctic Acid Free in Solution and Bound to Au Nanoparticles.

Proton Assignment			
(ppm)	**Nanoparticle Bound (ppm)**	**Free Ligand**	**Chemical Shift Difference (δ ppm)**
7	2.05	2.05	0.00
6	1.50	1.45	0.05
5	1.38	0.80	0.58
4	1.60, 1.70	1.10	0.50, 0.60
3	3.65	Not observed	-
2	1.90, 2.40	1.70, 2.10	0.20, 0.30
1	3.15	Not observed	-

Second, a greater degree of up-field chemical shift difference is observed for the methylene protons on carbons 5 and 4. As discussed previously, chemical shift differences between free and nanoparticle bound NMR signatures increase as the distance from the nanoparticle surface decreases.[99] Following this reasoning, the degree of up-field shift differences for a given proton can be used to gauge its average distance from the nanoparticle surface relative to other protons. Finally, although the protons on carbon 2 are detectable, the protons on carbons 3 and 1 are not observed because of significant signal broadening which leads to minimization of the signal to noise ratio of these peaks. As expected, these data suggest thioctic acid is attached to the surface of the gold nanoparticle via the dithiol ring with the carboxylic acid group extending out into solution.

2.3.4 XPS Characterization of and Packing Density Estimation for Au@TA Nanoparticles

Both LSPR and zeta potential data indicate that the slow addition of salt increases the packing density of thioctic acid on the gold nanoparticle surface. To verify this, quantitative information regarding the efficiency of thiol immobilization and the nature

of thiol-gold interactions are probed using XPS. Previously, thioctic acid functionalized gold thin film analysis revealed that the S 2p region exhibited a pair of doublets with a 1.2 eV splitting energy centered at ~161.8 and 164.0 eV for molecules directly bound and unbound to the gold surface, respectively.[45, 149] As shown in Figure 2.5A, Au@TA nanoparticles that are singly rinsed exhibit S 2p photoelectron spectral features consistent with bound and unbound thioctic acid molecules. Repeated rinsing, however, leads to the disappearance of the high binding energy (BE) S 2p bands associated with unbound thioctic acid.[150] Figure 2.5B reveals XPS spectra of Au@TA nanoparticles prepared in the absence and presence of salt after sufficient rinsing. In these data, a single S 2p doublet (centered at ~162.5 eV) is observed. While the S 2p photoelectron spectra exhibit weak signal strengths because of the sub-monolayer to monolayer thioctic acid surface coverage on the nanoparticle surfaces, these findings indicate that the majority of the signal is attributed to surface bound thioctic acid ligands.

To evaluate how incubation time and/or salt concentration impact thioctic acid surface coverage, the S 2p doublet signal strength was monitored. Figure 2.5B compares S 2p spectra for Au@TA nanoparticles prepared in 0 and 16 mM NaCl after a 72 hour incubation period. Signal correction of the S 2p peak area to the gold 4f peak area removed any interference caused by evaluating slightly different nanoparticle concentrations and samples. These data reveal that the addition of NaCl during thioctic acid functionalization increases the normalized S 2p peak area versus conditions when no salt is added. Moreover, the C 1s peak area and the O 1s peak area did not show any trends as a result of organic species contamination as the samples were prepared in ambient conditions.[151]

To quantitate the XPS data, the S 2p and Au 4f peak areas were converted to a S:Au atomic ratio using the empirical atomic sensitivity factor (SF) for each element (SF = 0.54 and 4.95 for S 2p and Au 4f, respectively). Furthermore, because XPS

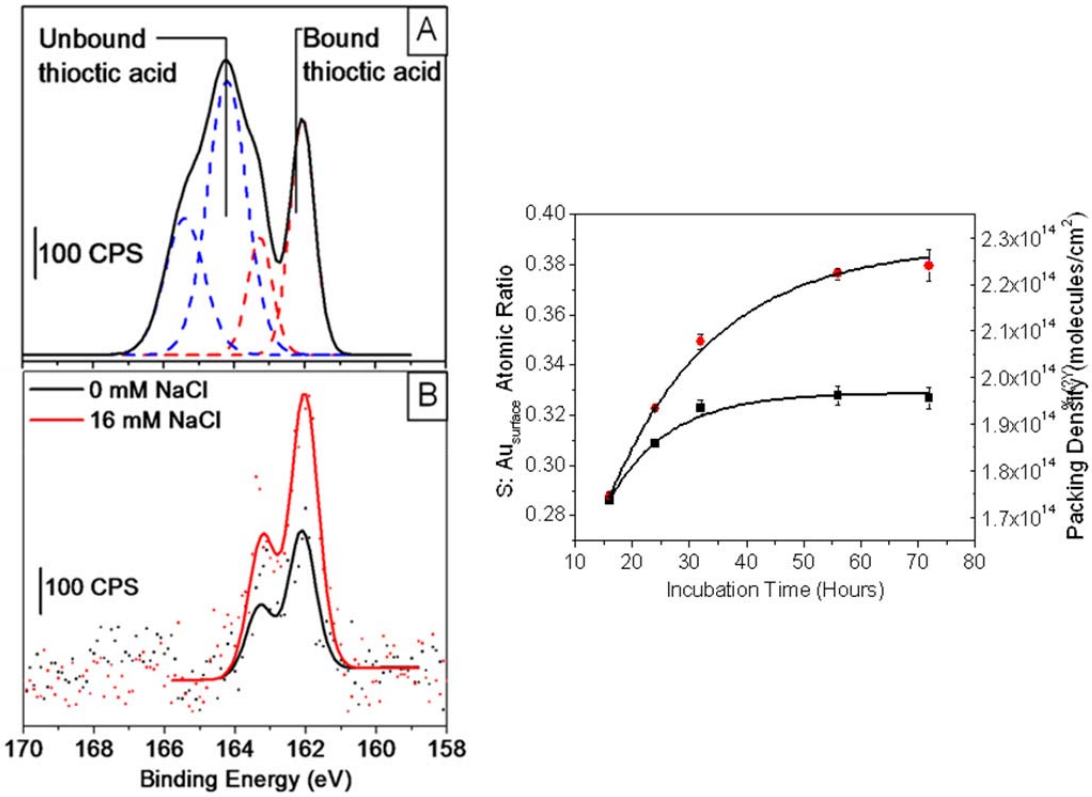

Figure 2.5 XPS characterization of Au@TA nanoparticles. (A) Normalized XPS spectra (S 2p) of Au@TA nanoparticles after one rinsing cycle. Two thioctic acid species are predominant (BE = 164.3 and 165.5 eV). (B) Normalized XPS spectra of Au@TA nanoparticles prepared in 0 and 16 mM NaCl (equilibration time = 72 hours) where the solid lines and dots correspond to the fitted and raw data, respectively. (C) Comparison of the S atom: $Au_{surface}$ atomic ratio (right-hand y axis) and packing density (left-hand y axis) vs. incubation time for Au@TA nanoparticles prepared in the (●) presence and (■) absence of NaCl. The solid lines represent exponential fits for the S_{atom}: $Au_{surface}$ atom ratio vs. incubation time: "No NaCl" $y = -0.19_8e^{-x/10.4} + 0.32_9$ and "With NaCl" $y = -0.24_0e^{-x/18.4} + 0.38_8$.

interrogates a fraction of the total atomic layers, the Au XPS area must be corrected for the electron escape depth as follows:

$$\text{Escape Depth} = \lambda \cos(\theta) \tag{2.1}$$

where λ is the inelastic mean free path (IMFP) and θ is the angle between the surface normal and the direction of the emitted electron.[151, 152] For these experiments; θ is 0, and λ is $1.78 \pm 0.00_2$ nm where the IMFP is determined using the NIST Electron Inelastic Mean Free Path Database, and the average kinetic energy of the Au 4f peaks.[153-155]

To apply this to a nanoparticle, the shell method must be used to calculate the total number of atomic layers in a nanoparticle.[69, 156] The shell method models a nanoparticle as a central atom which is surrounded by n shells (i.e. layers) of gold atoms where the number of gold atoms in the *n*th shell can be calculated using the equation $10n^2+2$.[69, 156] Next, the total number of shells per nanoparticle is calculated by dividing the nanoparticle diameter ($d = 11.6_1 \pm 0.9_8$ nm) by the gold atom diameter (d_{Au} = 2.882 Å). Dividing the escape depth by the diameter of a gold atom will finally yield the number of atomic layers signaled (N_{layer}) as follows:

$$N_{layer} = \frac{\lambda}{d_{Au}} = 6._2 \text{ layers} \tag{2.2}$$

where the number of layers is rounded to the closest whole number of shells in subsequent calculations.

Using these equations, a gold nanoparticle ($d = 11.6_1 \pm 0.9_8$ nm) contains 20 shells total but ~6 are sampled. The shell method can be applied to correct the S to Au atomic ratio ($S/Au_{surface}$) using the following equation:

$$\frac{S}{Au_{surface}} = \left[\frac{\sum_{n=15}^{20} (10n^2 + 2)}{10n^2 + 2} \right] \left[\frac{S}{Au} \right] \tag{2.3}$$

where the numerator in the first set of brackets is the number of total gold atoms signaled (n = 15 to 20), and the denominator is the number of surface gold atoms (n = 20). In the second set of brackets, S/Au represents the (sensitivity factor) corrected XPS signal.

In order to distinguish if increased thioctic acid SAM packing density arises from the systematic addition of NaCl or from increased incubation time with thioctic acid, the $S/Au_{surface}$ atomic ratio for gold nanoparticles incubated with thioctic acid in the absence and presence of NaCl are compared (Figure 2.5C). In both ligand exchange environments, the $S/Au_{surface}$ atomic ratio increases systematically with increasing thioctic acid incubation times. Figure 2.5C clearly displays that the $S/Au_{surface}$ atomic ratio saturates after an incubation period of 72 hours. Additionally, while longer incubation times increase the number of thioctic acid molecules on the Au nanoparticles; salt mediates this process.[81] By applying an exponential fit to these data, saturated $S/Au_{surface}$ atomic ratios of 0.32_9 and 0.38_8 are calculated for Au@TA nanoparticles incubated in absence and presence of NaCl, respectively. In the absence of NaCl, these values imply that at least three gold atoms interact with one sulfur atom. In comparison, this value decreases to ~2.5 gold atoms interacting with each sulfur atom for SAMs prepared in the presence of NaCl. While the difference between the $S/Au_{surface}$ atomic ratio is small, significant differences in the number of molecules on the nanoparticle surfaces are indicated.

Expanding on these data, the packing density of thioctic acid SAMs on gold nanoparticles can be estimated. As discussed previously, the core sizes of Au@TA nanoparticles incubated in the absence and presence of NaCl are not significantly different (Figure 2.2A-D) and the surface of ~12 nm gold nanoparticles contain predominately (100) surface planes.[157, 158] As a result, the packing density of atoms on the surface on the nanoparticle (σ_{hkl}) can be calculated as follows:

$$\sigma_{hkl} = \frac{4}{Qa^2(h^2 + k^2 + l^2)^{1/2}} \tag{2.4}$$

where Q is 2 for (100) and a is the bulk lattice parameter.

Next, the packing density of thioctic acid on Au@TA nanoparticle surfaces prepared in the absence and presence of salt can be approximated from XPS data as follows:

$$\text{Packing density} = \left[\frac{S}{Au_{surface}}\right]\left[\frac{TA}{S}\right]\left[\sigma_{100}\right] \tag{2.5}$$

where the corrected XPS signal (Equation 2.3), the thioctic acid to sulfur ratio (2 sulfur atoms per thioctic molecule), and the gold atom packing density for a (100) surface plane are found in the first, second, and third brackets, respectively. For Au@TA nanoparticles prepared in the absence of salt, surface coverage is ~1.7_2 x 10^{14} molecules/cm^2 after 16 hours of equilibration time and increases to 1.9_7 x 10^{14} molecules/cm^2 after equilibrating for 72 hours. With systematic NaCl additions, Au@TA nanoparticles equilibrated for 16 hours exhibit thioctic acid packing densities of 1.7_3 x 10^{14} molecules/cm^2 and increases to 2.2_9 x 10^{14} molecules/cm^2 after equilibrating for 72 hours. The packing density calculations demonstrate that the slow addition of salt increases thioctic acid SAM packing density by 17% relative to the control experiments. These values agree well with previously reported thioctic acid packing densities on flat gold surfaces which range from $1.8x10^{14}$ – $2.1x10^{14}$ molecules/cm^2,[80, 159-164] indicating XPS is an excellent technique to quantitate SAM packing density on gold nanoparticles.

2.3.5 Mechanism of Salt-Mediated TA Self-Assembly on Gold Nanoparticles

The LSPR, XPS, and zeta potential measurements suggest that the slow addition of salt increases the chemisorption of thioctic acid on gold nanoparticle surfaces thereby resulting in overall larger SAM surface coverages than when salt is not included. We

hypothesize that the mechanism of this effect is attributed to changes in the Debye length thickness surrounding the carboxylic acid headgroups. As a result, the Debye-Hückel limiting law is used to estimate corresponding Debye lengths as a function of NaCl concentrations used in this study (Table 2.2). Relative permittivities (ε_S) required for the Debye length calculation are computed using the following expression derived by Fawett *et. al.*:[165]

$$\varepsilon_S = 78.45 - \delta_S C_S + b C_S^{3/2} \quad (2.6)$$

where δ_S is the permittivity decrement (16 $L \cdot mol^{-1}$ when NaCl is the electrolyte), C_S is the electrolyte concentration, and b is a constant with a value of 5 $L^{2/3} \cdot mol^{-3/2}$. Table 2.2 reveals that NaCl concentration is inversely proportional to Debye length; thus as NaCl concentration increases, pinhole defects in the SAM layer are more easily accessed and filled by additional thioctic acid molecules.

Table 2.2 Calculated Debye Lengths using the Debye Hückel Limiting Law as a Function of NaCl Concentration.

[NaCl] (mM)	**Debye Length (nm)**
0	5.6
4	3.6
8	2.9
16	2.2
25	1.8

2.3.6 Implications of TA Packing Density on Nanoparticle Stability

To further investigate how SAM packing density impacts nanostructure stability, the flocculation parameter[45, 90, 166] for Au@TA nanoparticles incubated for 72 hours in the absence and presence of NaCl is evaluated. Flocculation parameter studies can be used to

gain semi-quantitative information about the nanostructure stability by monitoring changes in extinction as a function of solution pH and/or time.[45, 90, 166] As nanoparticle flocculation increases, the extinction intensity at ~521 nm decreases while a new lower energy band at 650 nm intensifies. Next, the extinction spectra were integrated from 575 – 800 nm to quantify the degree of nanoparticle flocculation as a function of time (Figure 2.6). In pH 5.5 buffer, the integrated area increases as a function of time and at different rates for the two nanoparticle samples. To compare the stability of the Au@TA nanoparticles, the integrated data was used to determine when flocculation reached its maximum. Larger values are indicative of more stable nanostructures.[166] The Au@TA nanoparticles incubated without NaCl flocculated within 26 seconds whereas the Au@TA nanoparticles incubated in the presence of NaCl flocculated in twice the time. Significantly, these flocculation studies reveal that salt-mediated thioctic acid self-assembly increases the stability of the Au@TA nanoparticles by ~20% vs. controls.

2.4 Conclusions

In summary, gold nanoparticles functionalized with thioctic acid were prepared with the slow addition of NaCl. TEM, ^{1}H NMR, extinction spectroscopy, zeta potential, XPS, and flocculation studies determined that the self-assembly of thioctic acid on gold nanoparticles increases with increasing NaCl concentration. Quantitative information regarding the fraction of pinhole and collapsed defect sites on gold nanoparticles was not evaluated; however, salt facilitated the self-assembly process. First, an increase in NaCl decreases the Debye length surrounding the deprotonated carboxylate groups on the assembled thioctic acid molecules thereby facilitating increased SAM packing densities. Furthermore, the slow addition of NaCl to gold nanoparticle solutions during thioctic acid self assembly increased subsequent functionalized nanoparticle stability vs. controls as determined from flocculation studies. We expect these results will improve strategies for reproducible SAM formation on solution-phase nanostructures. Future studies could be

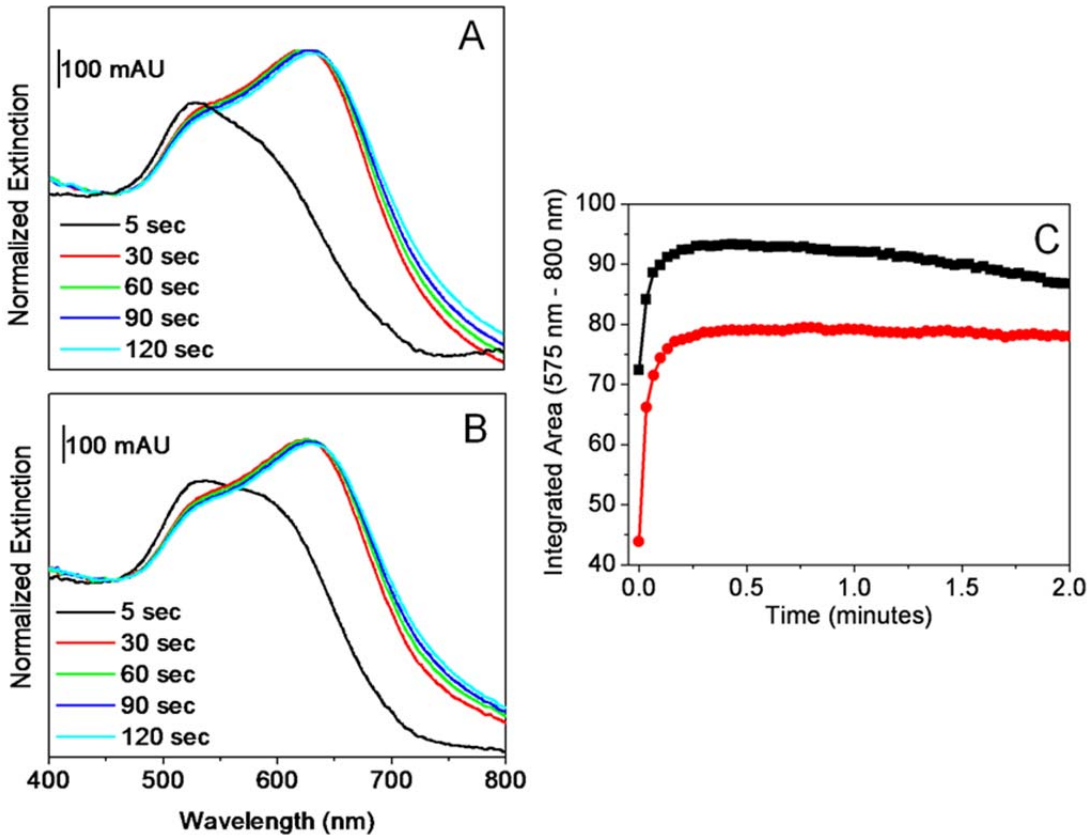

Figure 2.6 Normalized extinction spectra for Au@TA nanoparticles incubated for 72 hours in the (A) absence and (B) presence of 16 mM NaCl. Nanoparticles were centrifuged, dispersed in buffer (pH 5.5), and monitored while stirring as a function of time. Normalized integrated area (C) for Au@TA nanoparticles incubated for 72 hours in the presence (●) and absence (■) of salt. Extinction spectra of Au@TA nanoparticles in buffer (pH=5.5) and integrated areas were collected from λ = 575-800 nm.

expanded to investigate how nanoparticle shape, size, and radius of curvature impact this self assembly process for ultimate improvements in the reproducible synthesis and use of nanomaterials in a variety of applications.

CHAPTER 3
QUALITATIVE AND QUANTITATIVE COMPARISONS OF THIOCTIC ACID, 6-MERCAPTOHEXANOIC ACID, AND 11-MERCAPTOUNDECANOIC ACID FUNCTIONALIZED GOLD NANOPARTICLES

3.1 Introduction

The 21st century is marked by the incredibly rapid development of nanotechnology which encompasses many scientific fields including biotechnology, chemistry, engineering, materials science, and physics.[167] The interdisciplinary nature of nanotechnology facilitates the exploitation of the unique chemical and physical properties of nanomaterials. For instance, gold is a widely used material in nanotechnology because of its chemical stability,[28, 168, 169] diverse surface chemistry,[170, 171] and unique optical properties.[172, 173] Critical to gold nanoparticle-based technologies is the use of sulfur bound self assembled monolayers (SAMs).[174, 175] These monolayers form because of the high binding affinity (47 kcal/mol) between sulfur and gold.[176, 177] Ordered monolayers can be terminated with a wide range of organic molecules including alcohols,[178] amines,[179] carboxylic acids[179] and hydroxyls.[180, 181]

SAM formation on gold nanoparticles can be monitored using localized surface plasmon resonance (LSPR) spectroscopy.[67-69] The LSPR of gold nanoparticles is (1) experimentally measured using extinction spectroscopy (i.e. scattered and absorbed light);[70] (2) dependent on the distance matter is from the nanoparticle surface;[71] (3) theoretically predicted using Mie theory;[72] and (4) dictated by nanoparticle composition, shape, size, and local environment surrounding the core nanomaterial.[72, 82] Previously, LSPR spectroscopy was used to investigate a wide variety of chemical phenomena including biosensors for disease diagnosis,[75] cancer research,[76, 77] single molecule detection,[78] and with surface enhanced Raman scattering (SERS).[79]

Previously, SAM functionalization and characterization led to new materials for biosensors, [110, 114]; biotechnology,[111] chemical sensors, [112, 117] and molecular electronics.[119, 120] In all cases, efficient and reproducible utilization of functionalized gold surfaces depends on the assembly of defect-free SAMs.[182] Alkanethiol chains composed of at least 10 carbons produce SAMs which are more highly ordered than shorter chains.[127, 128] These SAMs, however, generally contain at least three types of defect sites: pinholes,[183] gauche defects in alkyl chains,[184] and collapsed-site defects;[185] which arise from (1) imperfect adsorption of alkanethiols during the self assembly process; (2) thermally and tilt-order driven chain dynamics; (3) and/or loss of thiols during rinsing, storage, and use.[127, 130] The fraction of these defect sites to the total surface area is estimated at ~6-10% for thiols on flat gold surfaces.[131] Reducing these defects requires investigation of the kinetics of SAM formation on gold surfaces.

The mechanism of SAM chemisorption on gold surfaces is still debated.[186] For example, Calvente et. al.[187] and others[188, 189]describe SAM formation in a two-step process: a rapid (24 hour) chemisorption of thiols to gold, followed by reorganization of the molecular backbone to eliminate gauche and pinhole defects. Whereas Georgiadis et. al.[190] and others,[80, 191, 192] describe the kinetics of SAM formation in *three* steps: the rapid chemisorption of the thiol groups onto the gold surface; a reorganization of the molecular backbone to eliminate gauche defects; and finally, the filling of pinhole defects. In both assembly mechanisms, the influence of binding moiety,[127] chain length,[132]chemical composition,[133] immersion time,[193] and substrate topography[134] impact SAM formation.

Herein, carboxylic terminated SAM formation on gold nanoparticles is monitored as a function of time and characterized both qualitatively and quantitatively. Thioctic acid, 6-mercaptohexanoic acid, and 11-mercaptoundecanoic acid functionalized gold (Au@TA, Au@MHA, and Au@MUA, respectively) nanoparticles exhibit unique trends in SAM formation and stabilities (Figure 3.1). Specifically, increasing SAM ligand chain length and binding moiety increases the rate of ligand binding proportionally and

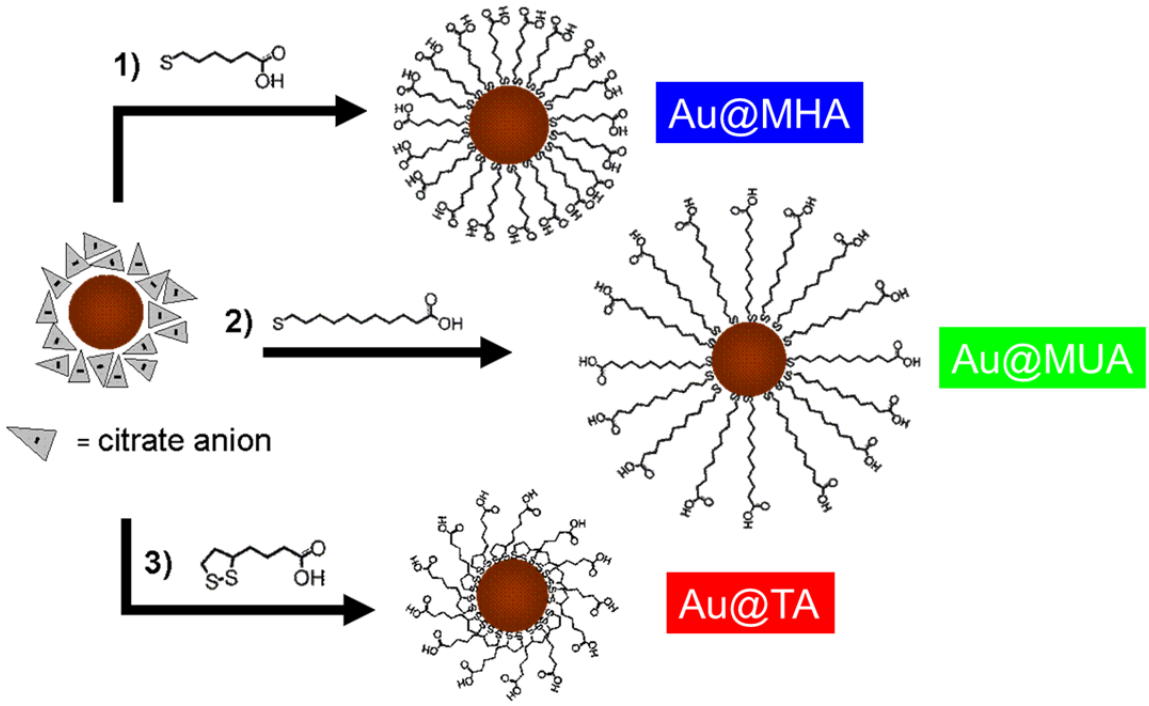

Figure 3.1 Gold nanoparticle functionalization scheme: 1) 6-mercaptohexanoic acid (Au@MHA), 2) 11-mercaptoundecanioc acid (Au@MUA), and 3) thioctic acid (Au@TA) nanoparticles. Drawings are not to scale.

inversely proportionally, respectively. This is evaluated using LSPR spectroscopy. Resultantly, surface charge, molecular orientation, packing density, and effective nanoparticle pK_a will be assessed using zeta potential, ^1H NMR, flocculation parameter studies, and X-ray photoelectron spectroscopy, respectively. These qualitative and quantitative characterization tools provide a comprehensive understanding of carboxylated SAM formation on gold nanoparticles and resulting implications thereby assisting in the reproducible functionalized of gold nanoparticles for various applications.

3.2 Experimental

3.2.1 Reagents and Chemicals

All chemicals were purchased from Sigma-Aldrich (St Louis, MO) unless otherwise noted. Water was purified to a resistivity greater than 18 MΩ cm^{-1} using a Barnstead Nanopure (Dubuque, IA) water filtration system. Nanoparticle solution pH was adjusted to 11 using a 1 M NaOH stock solution. Stock buffer solution (pH 7.2) was prepared from sodium dihydrogen phosphate dihydrate and sodium phosphate dibasic heptahydrate and diluted with water to a final conductivity of 5.5 mS cm^{-1}, filtered using a 0.2 μm nylon filter (Whatman, Middlesex, UK), and degassed prior to use.

3.2.2 Citrate Stabilized Nanoparticle Synthesis

All glassware were cleaned with aqua regia and rinsed prior to nanoparticle synthesis. Gold nanoparticles were prepared using an established procedure.[106] Briefly, 20 mg of $HAuCl_4$ was dissolved in 50 mL of water and brought to a rolling boil while stirring using a reflux condenser. Trisodium citrate (60 mg) was dissolved in water (5 mL) and added to the boiling solution. Initially, the solution was dark violet which quickly changed to red. The solution was refluxed for an additional 15-20 minutes. After cooling, the resulting nanoparticle solution was stored in a brown bottle. Nanoparticle

solutions were filtered through 13 mm diameter, 0.45 μm nylon filters (Whatman, Middlesex, UK) prior to use.

3.2.3 Nanoparticle Functionalization and Preparation

Citrate stabilized gold (Au@citrate) nanoparticles were functionalized with either 6-mercaptohexanoic acid (MHA), thioctic acid (TA), or 11-mercaptoundecanoic acid (MUA). First, 1 mL of 10 mM ligand (MHA, TA, or MUA) was dissolved in ethanol and added to 10 mL of a 10 nM Au@citrate nanoparticle solution. This solution was stirred at 500 RPM for at least 60 hours at room temperature. The nanoparticles were then centrifuged at 11,500 RPM (8797 x g) for 40 minutes, and the supernatant was replaced with pH adjusted water (pH adjusted to 11 with 1 M NaOH). The rinsing procedure was repeated three times to ensure sufficient removal of unbound ligand. The nanoparticles were stored in a brown bottle until use.

3.2.4 Transmission Electron Microscopy (TEM)

Nanoparticles homogeneity was characterized by TEM using a JEOL JEM-1230. In all cases, 2 μL of diluted nanoparticle solutions (50% mixture in ethanol) was applied to a carbon-formvar coated copper grid (400 mesh, Ted Pella, Redding, CA or Electron Microscopy Sciences Hatfield, PA) and allowed to air dry. The resulting images were analyzed using Image Pro Analyzer, and at least 100 nanoparticles were evaluated per sample.

3.2.5 UV-Visible (UV-Vis) Spectroscopy

Nanoparticle solutions were characterized using an UV-Vis spectrometer (USB 4000, Ocean Optics, Dunedin, FL) and white light source. All measurements were taken using the following parameters: 10 millisecond integration time, 20 averages, and boxcar of 5. Stock solutions were diluted using a 5.5 mS cm^{-1} pH 7.3 sodium phosphate (NaPi)

buffer. Extinction maxima were calculated from the zero point crossing value of the first derivative of the spectra using an in-house written MathCAD program.

3.2.6 Flocculation Parameter Measurements

Flocculation was monitored using previously established techniques.[45, 233] Briefly, Au nanoparticle stock solutions were diluted to 1 nM concentrations in 5.5 mS cm^{-1} buffers ranging in pH from 2 to 11. Extinction spectra collected after two minute incubation periods were plotted as a function of buffer pH. An in-house developed MATLAB program was used to baseline adjust all spectra to 0 AU at λ = 800 nm and to subsequently normalized each spectrum using data collected in pH 12 buffer for that sample. Flocculation parameters were calculated from integrated areas between 600-800 nm. To compare the samples, these flocculation parameters were converted to a percentage, plotted vs. pH, and fit with a sigmoidal curve. The effective zero-point charge of the nanoparticle and surface bound ligand pK_a was determined at 0 %.

3.2.7 Zeta Potential Measurements

Nanoparticle solutions were diluted to 1 nM in NaPi buffer prior to zeta potential measurements (Delsa Nano, Beckman-Coulter, Brea, CA). Samples were allowed to incubate for two minutes prior to analysis. Zeta potential measurements were performed in triplicate using H_2O diluent parameters (refractive index (RI) = 1.3328, viscocity (η) = 0.8919 cP, and dielectric constant (ε) = 78.4) at 25° C. A flow cell configuration was used for all measurements, and the data were fit using Smoluchowski theory.

3.2.8 ^{1}H NMR Spectroscopy

^{1}H NMR and 2D COSY spectra were recorded on a Bruker 600 mHz spectrometer (Bruker Biospin Corp., Billerica, MA). Each functionalized gold nanoparticle sample was prepared uniquely to maximize their stability during these measurements. Au@MUA and Au@TA nanoparticle samples were centrifuged at 11,500

RPM (8,797 x g) for 40 minutes. Au@MHA nanoparticle samples were centrifuged at 5,000 RPM (1,817 x g) for 20 minutes. The supernatant was then removed and re-centrifuged to maximize sample recovery. In all cases, the sample were redispersed in pH adjusted D_2O (pH adjusted to 11 with 1 M NaOH). This procedure was repeated in triplicate to maximize the removal of H_2O and other contaminates. After rinsing, nanoparticle concentration was determined using a standard estimation model[89] which yielded 5, 10, and 20 nM for Au@MHA, Au@TA, and Au@MUA nanoparticles, respectively. NMR spectra were analyzed using Topspin and Nuts. Chemical shifts were referenced to the residual shifts of the deuterated solvent.[194] 2D COSY spectra were acquired using standard pulse sequences optimized to the individual parameters of each sample. These data were used for proton assignments in the 1D spectra.

3.2.9 X-Ray Photoelectron Spectroscopy (XPS)

XPS measurements were collected using a Kratos Axis Ultra Spectrometer with a monochromatic Al K_α X-ray source as described previously.[136] Briefly, a 160 eV pass energy, 1 eV step size, 200 msec dwell time, and ~700 μm x 300 μm X-ray spot size were used for a survey scan (range = 1200 – -5 eV). Region scans (O 1s, C 1s, S 2p, Au 4f) exhibited typical band widths of 20 - 50 eV, 20 eV pass energies, 0.1 eV step sizes, and 1000 msec dwell times.

All spectra were analyzed using CasaXPS and were charge-calibrated with respect to the adventitious C 1s peak at 285.0 eV. The S 2p peak of thioctic acid, 6-mercaptohexanoic acid, and 11-mercaptoundecanoic acid was deconvoluted using the S 2p doublet with a 2:1 area ratio and an energy difference of 1.2 eV. A Shirley background was used to subtract the inelastic background from the S 2p Au 4f signals. The curves were fit using a Gaussian/Lorentzian (GL(30)) lineshape. To account for differences in nanoparticle concentration in sample spots, the S 2p areas were normalized using the Au

4f areas. Measurements were performed in duplicate, and error bars represent the standard deviation of these data.

3.3 Results and Discussion

3.3.1 Bulk Optical, Size, and Concentration Characterization of Gold Nanoparticles

Nanometer-sized particles exhibit unique chemical and physical properties which depend on their shape, size, and local environment.[27, 195, 196] The extinction maxima wavelengths (λ_{max}) of gold nanoparticles are sensitive to the properties of the bulk dielectric environment and surface ligands.[70, 197] Figure 3.2 illustrates the chemical structures of four carboxylic acid containing surface ligands: (A) citrate, (B) thioctic acid, (C) 6-mercaptohexanoic acid, and (D) 11-mercaptoundecanoic acid. After incubating in the ligand solution for 1 week, Au@citrate nanoparticles exhibit an extinction maximum (λ_{max}) centered at 519.7 nm. This value is blue shifted from the three covalently functionalized samples. Of the covalently bound ligands studied, TA contains the largest surface binding moiety and shortest chain length. When TA is bound to gold

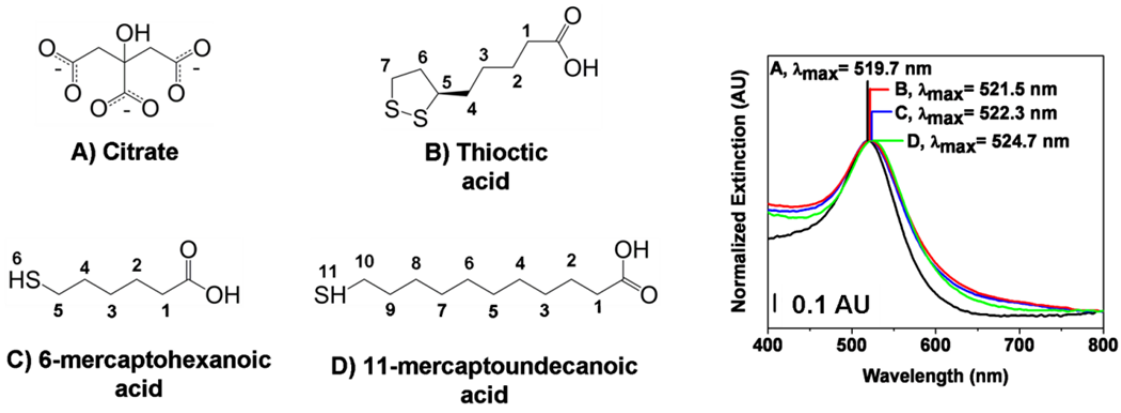

Figure 3.2 (Left) Molecular structures and proton assignments of (A) citrate, (B) thioctic acid, (C) 6-mercaptohexanoic acid and (D) 11- mercaptoundecanoic acid. (Right) Normalized extinction spectra of gold nanoparticles functionalized with (A) citrate, λmax = 519.7 nm; (B) thioctic acid, λmax = 521.5 nm; (C) 6-mercaptohexanoic acid, λmax = 522.3 nm; and (D) 11-mercaptoundecanoic acid, λmax = 524.7 nm in pH 11 adjusted H2O.

nanoparticles, the λ_{max} shifts to 521.5 nm. MHA is approximately the same length but contains a smaller binding footprint versus TA. As a result, the extinction maximum for Au@MHA nanoparticles are slightly red shifted (λ_{max}= 522.3 nm) versus Au@TA nanoparticles. The extinction maxima for Au@MUA functionalized nanoparticles is centered at λ_{max}= 524.7 nm. This red shifted value versus the other two covalently functionalized nanoparticles is supportive of the relatively longer alkanethiol chain length and greater expected packing density.[198]The LSPR spectra from Au nanoparticles covalently functionalized with carboxylic acid terminated SAMs exhibit surface chemistry dependent trends. First, the thioctic acid binds to the gold nanoparticle surface via a disulfide ring,[80, 81, 86] whereas 6-mercaptohexanoic acid and 11-mercaptoundecanoic acid bind via a single thiol bond.[199] The larger binding moiety of thioctic acid lowers its packing density vs. the other two SAMs.[189, 200] Furthermore, because the LSPR wavelength increases as alkanethiol chain length increases, Au@MHA nanoparticles exhibit a higher energy extinction maximum than Au@MUA nanoparticles.

Nanoparticle core size could also influence these plasmonic nanoparticle properties. As a result, each sample was evaluated with TEM. As shown in Figure 3.3A-D; Au@citrate, Au@TA, Au@MHA, and Au@MUA nanoparticles exhibit statistically similar core sizes at or near 13 nm. These data were used in conjunction with a standard estimation model to calculate the of gold nanoparticle concentration.[89]

3.3.2 Optimized Ligand Exchange Reactions

Ligand exchange reactions occur on nanoparticle surfaces and are both kinetically and thermodynamically controlled.[201] Incubation time, the time required for saturated SAM coverages, is a critical and easily controlled parameter to optimize SAM packing density. Regardless of the carboxylated ligand, unique incubation time dependent extinction maxima were observed for the functionalized nanoparticles. For example, Au@citrate nanoparticles were allowed to incubate for 5 minutes, 24 hours, and 60 hours

in 10 mM thioctic acid; and the extinction maximum shifted from 518.5 (original), to 521.5, 520.3, and 521.7 nm, respectively (Figure 3.4) as ligand packing density on the nanoparticle surface increased. Similar trends were observed for all three covalent surface functionalizations.

Although the total dynamics of self-assembly are not completely understood,[202] factors such as nanoparticle surface energy,[110] non-covalent ligand chain interactions, and the binding moiety[95] are known to influence SAM coverage. As shown in Figure 3.4, the extinction maxima of gold nanoparticles functionalized with covalently bound SAMs systematically red shifts as additional ligands bind to the gold surface. Three characteristic exchange phases are observed (Figure 3.5). The first phase of SAM formation is rapid (0 to 10 minutes) as electrostatically bound citrate molecules at the nanoparticle surface are displaced by the thiolated ligands. This occurs rapidly because of the high (47 kcal/mol)[176] binding affinity between sulfur and gold. Next, the surface bound ligands form a double layer which subsequently regulates additional exchange and reorganization for 24 hours.[186] Ligand imposed steric constraints and intermolecular forces (i.e. van der Waals interactions and hydrogen bonding) can either facilitate or prevent SAM reorganization. Because chain to chain stabilization energy increases by a ~1.1 kcal/mol for each carbon in the alkanethiol chain length,[203] longer alkanethiol chains stabilize more quickly than shorter chains. During the third and final phase of self assembly, gauche and pinhole site defects are reduced.[147] The presence and elimination of these defect sites depend on the solution conditions, impurities, and the composition of the ligand.[202]

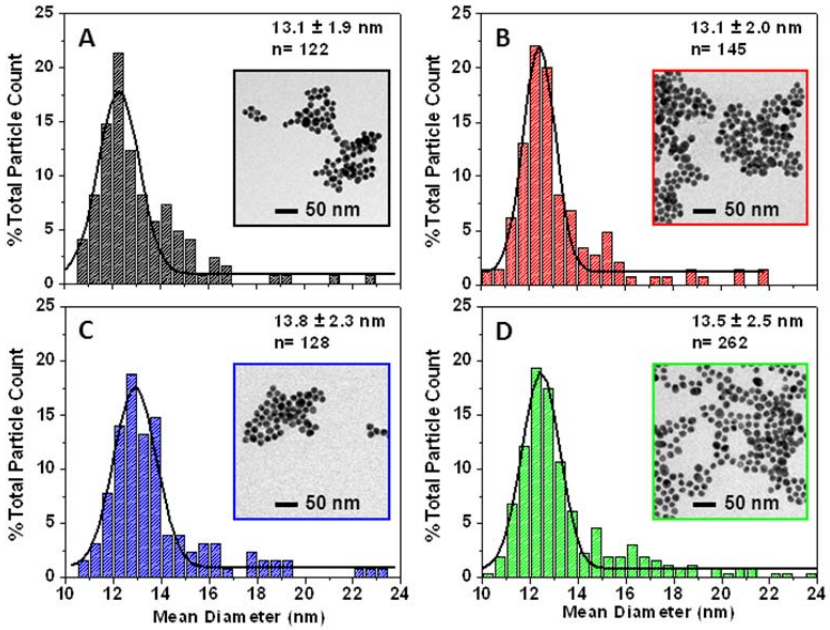

Figure 3.3 Histograms of nanoparticle diameter and TEM images. (A) Au@citrate (d = 13.1 ± 1.9 nm), (B) Au@TA (d = 13.1 ± 2.0 nm), (C) Au@MHA (d = 13.8 ± 2.3 nm), and (D) Au@MUA (d = 13.5 ± 2.5 nm) nanoparticles.

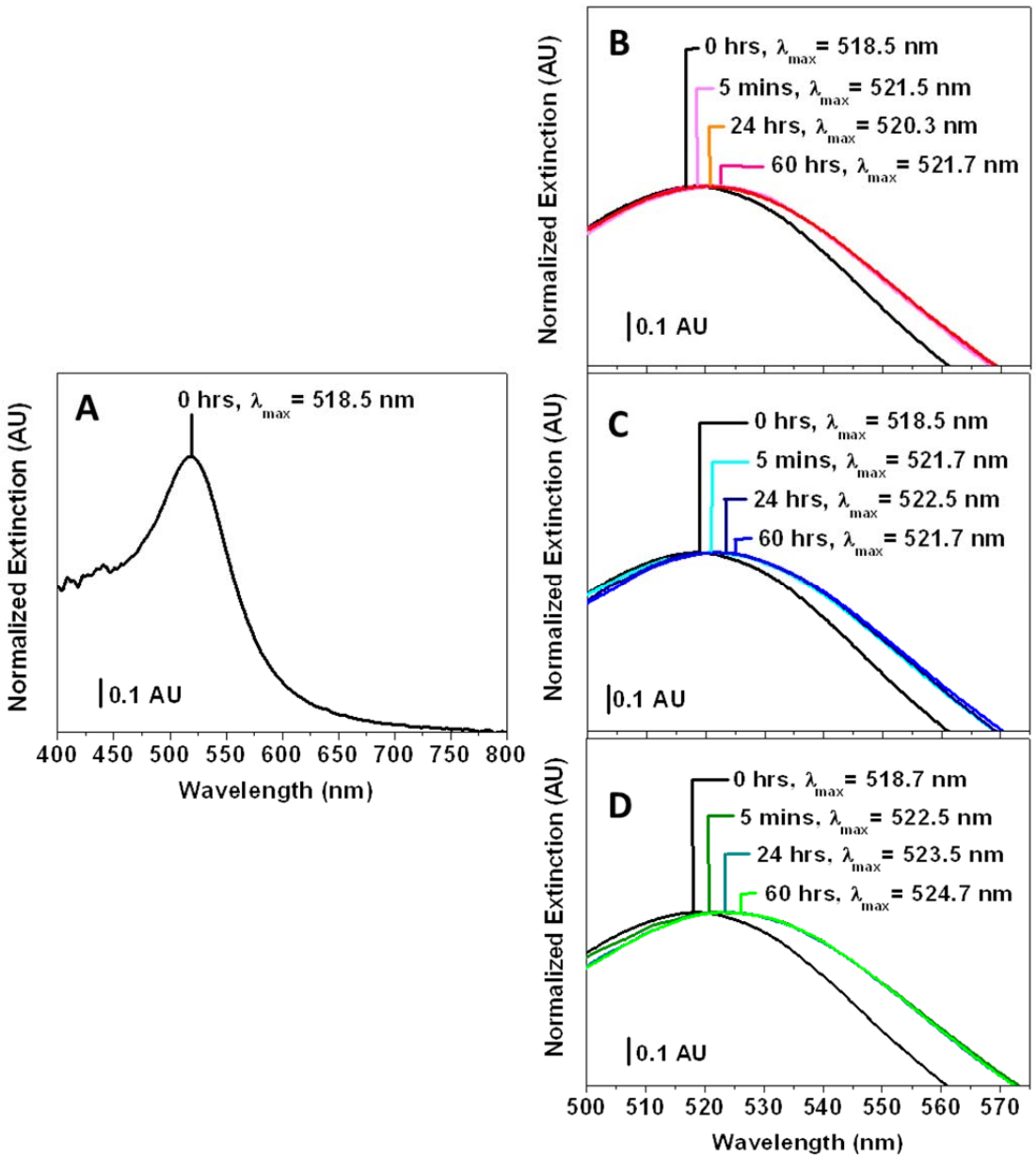

Figure 3.4 Normalized extinction spectra of gold nanoparticles (A) stabilized with citrate, and functionalized with (B) thioctic acid, (C) 6-mercaptohexanoic acid, and (D) 11-mercaptoundecanoic acid during ligand exchange reactions in aqueous solutions. Spectra are plotted prior to ligand addition (0 hours), as well as after 5 minutes, 24 hours and 60 hours after incubation. All spectra were collected in pH adjusted water (pH adjusted to 11 with 1 M NaOH).

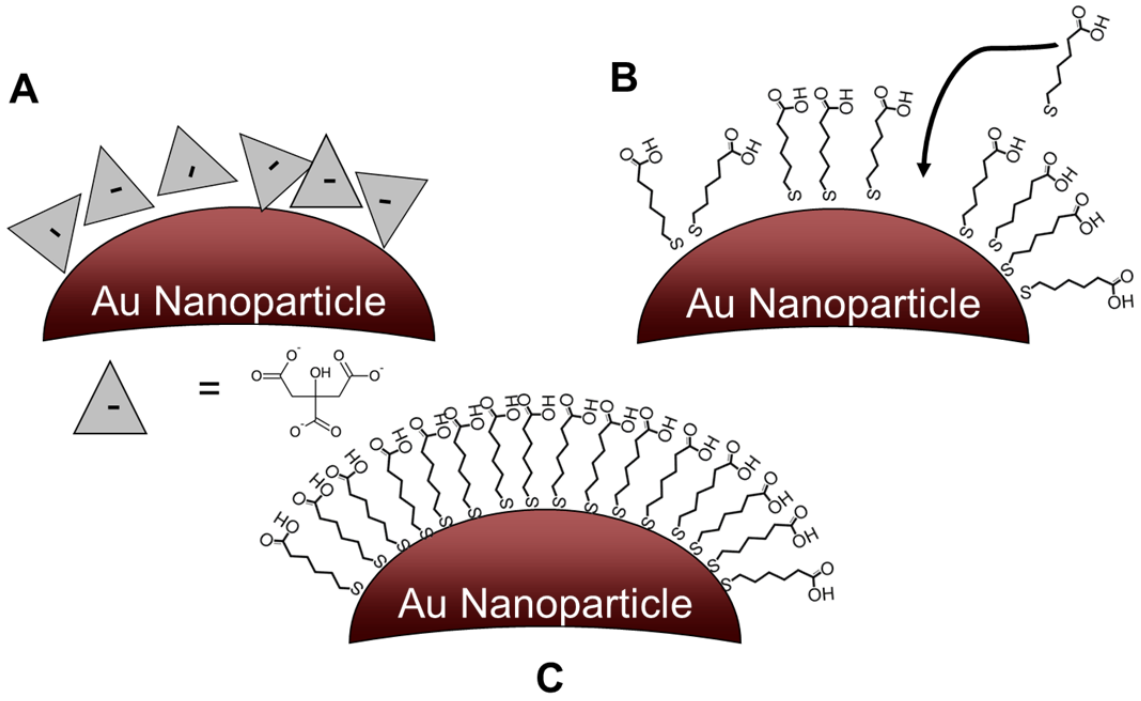

Figure 3.5 Schematic of the three SAM formation phases on Au nanoparticles. (A) Phase I is a rapid displacement of physisorbed citrate from the nanoparticle surface by incoming thiolated molecules. (B) Phase II is a double layer regulated surface ligand filling. (C) Phase III is the reduction of pinhole and gauche defects in the SAM. Drawings are not to scale.

Further analysis of these distinct phases in Figure 3.4 provides insight into chain length and binding moiety effects on SAM formation. For example, phase I for all three SAM functionalities can be fit using an exponential decay function (Equation 3.1).

$$y = Ae^{-x/t} + y_o \qquad (3.1)$$

where A is the rate of self-assembly, t is the first derivative time maximum, and y_o is the saturated extinction maximum wavelength value (Figure 3.6). These data reveal the rate of SAM formation is both chain length and binding moiety dependent. From these data, the rate of SAM formation is 4.5_6, 2.5_7, 1.8_1 nm/second for Au@MUA, Au@MHA, and Au@TA nanoparticles respectively. Accordingly, the extinction maximum shifts 1 nm in 220, 390, and 550 msec as these same molecules assemble on the nanoparticle surface.

These data are consistent with several published SAM formation studies for nanoparticle surfaces[163, 204] and confirm that 1) monothiol SAMs bind more quickly to Au than disulfide ligands and 2) the rate of SAM formation is chain length dependent.

3.3.3 Flocculation Parameter Studies as a Function of Ligand Composition and Local Environment

When nanoparticles aggregate, a complex low energy LSPR is produced as their electromagnetic fields couple.[205] Nanoparticles modified with SAMs can reduce uncontrolled aggregation by forming an electrostatically-induced steric barrier between nanoparticles. As the pH, ionic strength, and or solution composition changes; these electrostatic interactions will decrease, and nanoparticles can aggregate. To quantitate this change in stability, a flocculation parameter can be measured.[45, 90, 166] The flocculation parameter is calculated by integrating the extinction spectra from 600 to 800 nm (Figure 3.7A). Stable, isolated nanoparticles exhibit flocculation parameters of 0 while aggregated or agglomerated nanoparticles display larger values. While all three covalently functionalized Au nanoparticles are statistically identical in terms of core

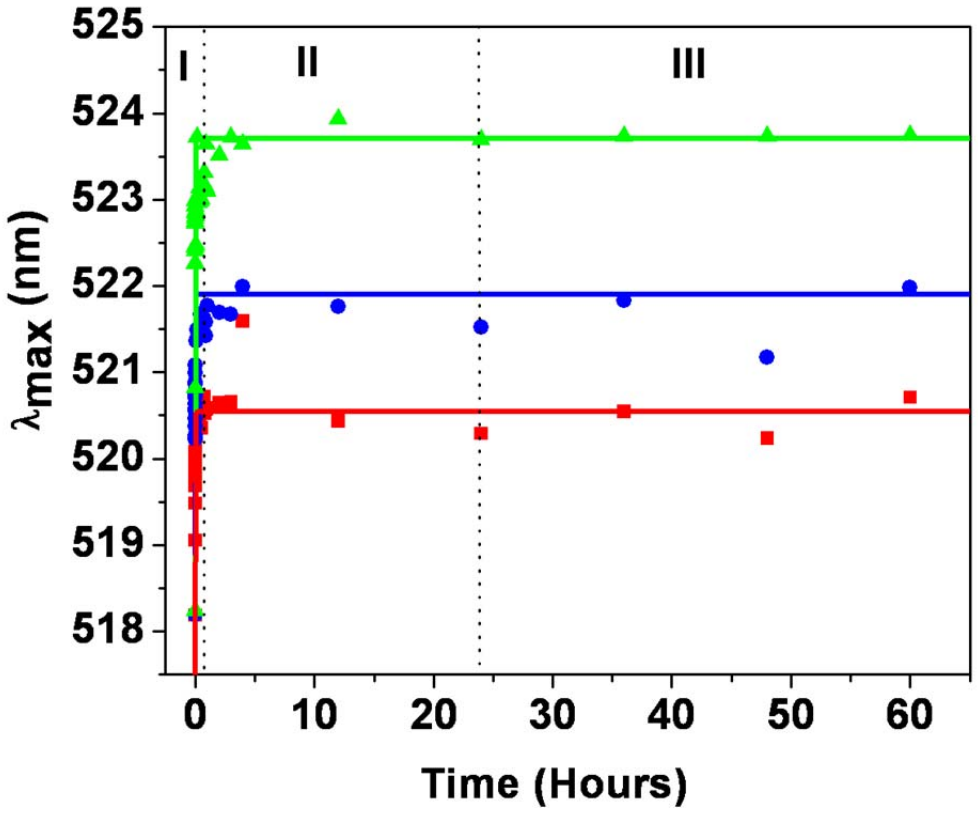

Figure 3.6 Extinction maxima as a function of incubation time for (■) Au@TA, (●) Au@MHA, and (▲) Au@MUA nanoparticles in aqueous solutions. Phases of SAM formation are labeled as I (0-10 minutes), II (10 minutes-24 hours), and III (24- 60 hours). The solid lines represent exponential decay fits for the λ_{max} vs. incubation time data: $y = Ae^{-x/t} + y_0$.

sizes, Au@TA, Au@MHA, and Au@MUA reveal unique flocculation parameters (i.e. stabilities) in various pH environments (Figure 3.7B).

3.3.3 Flocculation Parameter Studies as a Function of Ligand Composition and Local Environment

When nanoparticles aggregate, a complex low energy LSPR is produced as their electromagnetic fields couple.[205] Nanoparticles modified with SAMs can reduce uncontrolled aggregation by forming an electrostatically-induced steric barrier between nanoparticles. As the pH, ionic strength, and or solution composition changes; these electrostatic interactions will decrease, and nanoparticles can aggregate. To quantitate this change in stability, a flocculation parameter can be measured.[45, 90, 166] The flocculation parameter is calculated by integrating the extinction spectra from 600 to 800 nm (Figure 3.7A). Stable, isolated nanoparticles exhibit flocculation parameters of 0 while aggregated or agglomerated nanoparticles display larger values. While all three covalently functionalized Au nanoparticles are statistically identical in terms of core sizes, Au@TA, Au@MHA, and Au@MUA reveal unique flocculation parameters (i.e. stabilities) in various pH environments (Figure 3.7B).

From these data, the nanoparticle pK_a or point of zero charge can be estimated from the functionalized gold nanoparticles. In general, solution pH serves to either protonate or deprotonate the carboxylic acid head groups. For carboxylic acid ligands free in solution, typically pK_a values range from 4 to 5.[206] Covalent binding of the ligand to a gold surface changes the electronic structure of the molecule thus systematically changing the pK_a. As shown in Figure 3.7B, 6-mercaptohexanoic acid terminated monolayers on gold display an estimated pK_a of 6.9_0 versus the solution value of 4.8.[207] Interestingly, thioctic acid stabilized nanoparticles demonstrate less pK_a deviation at 6.3_0 versus free thioctic acid in solution (pK_a = 4.7-5.3).[208] This observation suggests that

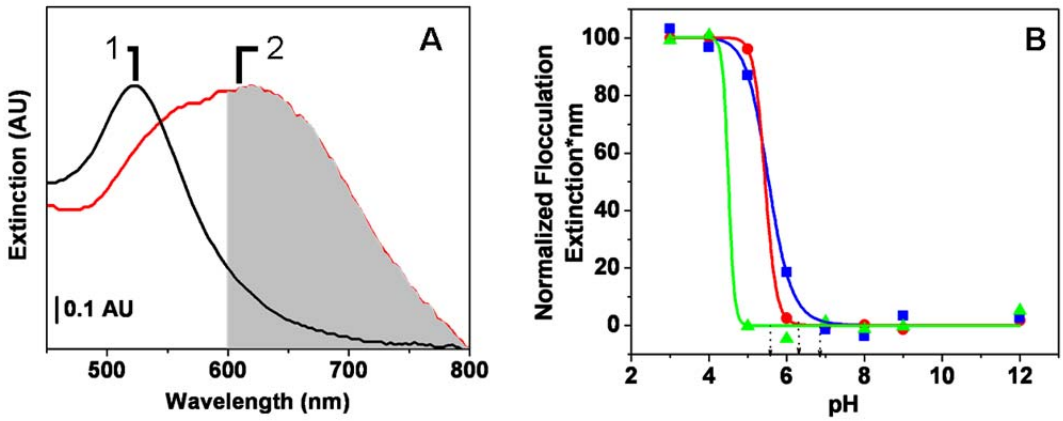

Figure 3.7 Evaluation of carboxylic acid functionalized gold nanoparticles. (A) The flocculation parameter is calculated from the integrated area of the excitation spectra from 600 to 800 nm. Example data for Au@MUA nanoparticles in (1) pH = 12, and (2) pH = 4 buffer, respectively are shown. (B) Flocculation parameter for Au@TA (●), Au@MHA (■), and Au@MUA (▲) nanoparticles in aqueous buffer solutions ranging in pH from 3 to 12 (B). Surface ligand pK_a values were determined at 0 % of the normalized flocculation parameter fit (dashed lines) for the Au@TA ($pK_a = 6.3_0$), Au@MHA ($pK_a = 6.9_0$), and Au@MUA ($pK_a = 5.6_7$) nanoparticles.

cyclic disulfide SAMs are more ordered and result in nanoparticles which are more stable than nanoparticles functionalized with the six carbon alkanethiol.[209, 210] The eleven carbon alkanethiol SAMs are more stable (i.e. exhibit the lowest pK_a value) versus the other functionalizations and exhibit a zero point charge of 5.6_7, a value slightly more basic than the free ligand in solution (4.6-5.0).[211]

3.3.4 Evaluating Surface Potential as a Function of SAM

In addition to surface charge estimations, nanoparticle stability can also be qualitatively evaluated using zeta potential. Previous studies revealed that carboxylic acid functionalized gold nanoparticles exhibited negative zeta potential values from 36 – 60 mV (pH 9).[106, 212] To distinguish differences between the gold nanoparticles functionalized with different carboxylic acid terminated monolayers, zeta potential measurements (in mV) were performed in NaPi. Au@TA and Au@MHA nanoparticles exhibit similar zeta potentials of -18.4 ± 1.3 mV and -20.9 ± 1.5 mV, respectively. This similarity is consistent with the similar SAM pK_a values estimated in the previous section. In contrast, Au@MUA nanoparticles possess a zeta potential of -37.6 ± 3.5 mV - a value ~ twice as large as the other functionalization schemes.

3.3.5 Determining Surface Ligand Orientation via ^1H NMR

To better understand the optical and electrical differences among the three Au nanoparticle functional schemes, SAM orientation on the gold nanoparticle surfaces are evaluated. The ^1H NMR spectra of the free ligands (11-mercaptoundecanoic acid, 6-mercaptohexanoic acid, and thioctic acid) are shown in Figure 3.8. These results are similar to previous reports of alkanethiol functionalized gold nanoparticles.[85, 97, 98, 213]

Recently, ^{13}C and ^1H NMR were applied to characterize molecules adsorbed to the surface of nanomaterials.[146] Four significant spectral characteristics are generally observed: (1) peak broadening;[83] (2) free ligand signatures superimposed on the surface-

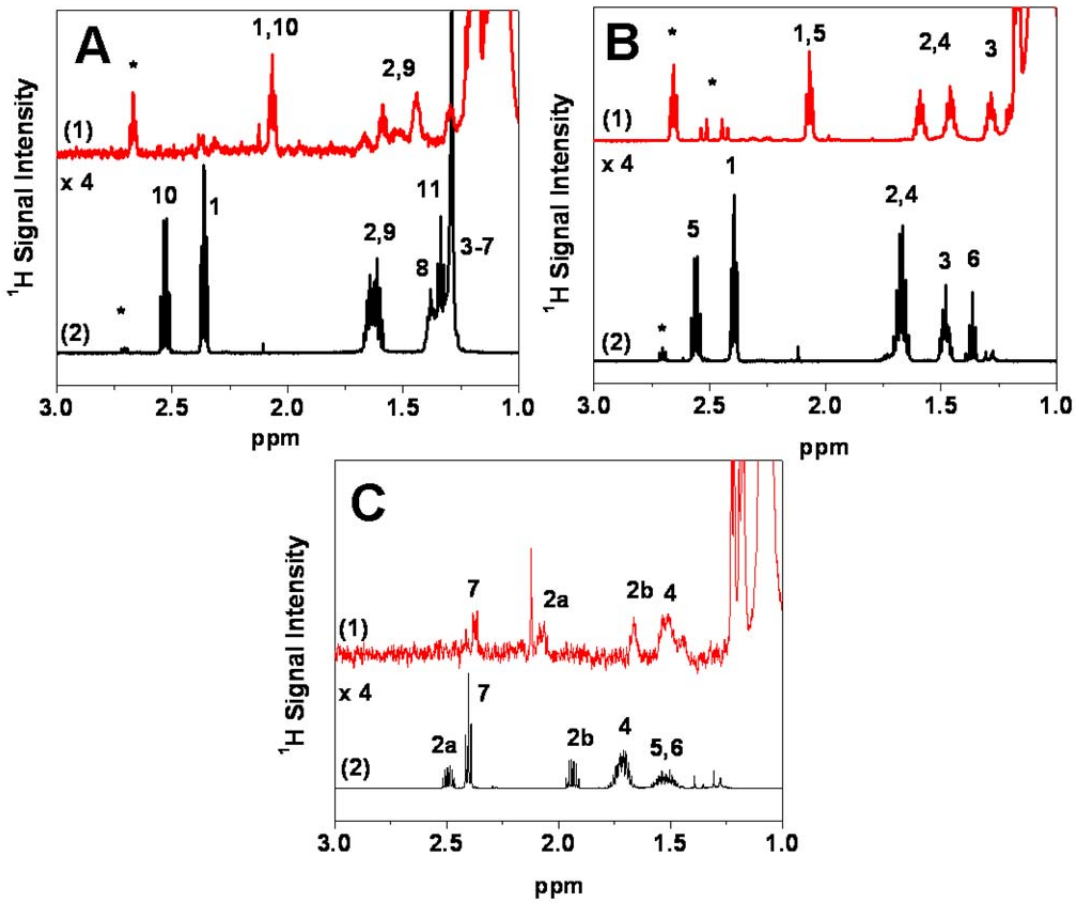

Figure 3.8 ^{1}H NMR characterization of gold nanoparticle and ligand solutions. (A) Comparisons of (1) 20 nM Au@MUA nanoparticles and (2) 10 mM 11-mercaptoundecanoic acid. (B - 1) 5 nM Au@MHA nanoparticles and (2) 10 mM 6-mercaptohexanoic acid, (C - 1) 10 nM Au@TA nanoparticles (1) and (2) 10 mM thioctic acid. In all cases, nanoparticles were diluted in D_2O and free ligands were diluted in $CDCl_3$. The numbers represent proton assignments for sample, and the (*) represents a contaminate peak.

bound ligand spectrum;[147] (3) chemical shift differences between free and surface-bound ligands;[147] (4) the absence of proton signals after binding to gold nanoparticle surfaces. Similar observations are made for all three nanoparticle functionalities studied. To determine the proton assignments shown in Figure 3.8A-C, 2D COSY studies were performed. Peak assignments can be characterized as triplets (t), quartets (q), and multiplets (m). For MUA, the following chemical shifts include: 1.30 - 1.35 ppm (t, thiol proton at S1), 1.35 – 1.375 ppm (m, methylene at protons at C9 and C4-C8), 1.60 ppm (m, methylene at protons at C3 and C10), 2.35 ppm (t, methylene at protons at C2), and 2.45 ppm (q, methylene at protons at C11). For MHA, the peak assignments are 1.35 ppm (t, thiol proton at S1), 1.42_5 – 1.45 ppm (m, methylene at protons at C4), 1.59_5-1.65 ppm (m, methylene at protons at C3 and C5), 2.35 ppm (t, methylene at protons at C2), and 2.45 ppm (q, methylene at protons at C6). For TA, the peak assignments are 1.35 ppm (t, thiol proton at S1), 1.42_5 – 1.45 ppm (m, methylene at protons at C4), 1.59_5-1.65 ppm (m, methylene at protons at C3 and C5), 2.35 ppm (t, methylene at protons at C2), and 2.45 ppm (q, methylene at protons at C6).

Using these COSY data, electric and magnetic differences between ligands free in solution and bound to nanoparticles can be learned. In comparison to free ligand studies, spectral features for all three ligands are significantly broadened when bound to gold nanoparticles thereby verifying the molecules sampled are chemisorbed to the nanoparticle surface and not free in solution. This is an important spectral feature given that no superimposed bands are observed in these spectra

The ^{1}H NMR spectra of surface bound ligands on Au@MUA, Au@MHA, and Au@TA nanoparticles exhibit up-field chemical shift differences relative to free ligands in solution (Figure 3.8). As discussed previously, chemical shift differences arise between free and nanoparticle bound NMR signatures as a result of the unique magnetic characteristics of nanoscale materials. For example, the magnetic properties of gold nanoparticles depend on core size.[99, 214] These ~13 nm gold nanoparticles are

paramagnetic, resulting in up-field shifts for bound ligands rather than free ligands in solution.[40]

In addition to chemical shift variations and peak broadening, 11-mercaptoundecanoic acid and 6-mercaptohexanoic acid functionalized gold nanoparticle spectra do not contain proton signatures associated with the S-H group, and the neighboring protons (on carbons 5 and 10) transform from quartets to triplets. These data suggest that this proton is close to the gold surface and/or is no longer present on the ligand.

3.3.6 Estimating Ligand Packing Density using XPS

LSPR, flocculation parameter, and zeta potential data suggest that equlibriation time as well as binding moiety and ligand chain length impact the packing density of SAMs on Au nanoparticles. As previously demonstrated,[81] XPS can be used to provide quantitative information regarding the efficiency of ligand immobilization.

Herein, Au@TA, Au@MHA, and Au@MUA nanoparticles with statistically similar core sizes (95% confidence interval) exhibit extinction spectra with characteristic extinction maxima wavelengths as well as distinct zeta potentials and flocculation parameter values (stabilities). These differences suggest that SAM packing density influences the effective surface charge and as a result, nanoparticle stability.

To quantitate nanoparticle surface chemistry, XPS is used.[81] Emperical atomic sensitivity factors and the shell method are utilized.[69, 81, 156] It should be noted that (1) the core size of Au nanoparticles functionalized with MUA, MHA, or TA are not statistically different and (2) the surface of gold nanoparticles contain predominately (100) surface planes.[157, 158] Finally, the packing density of carboxylic acid terminated SAMs on gold nanoparticles can be approximated from XPS spectra as follows:

$$\text{Packing density} = \left[\frac{S}{Au_{surface}}\right]\left[\frac{Ligand}{S}\right]\left[\sigma_{100}\right] \qquad (3.2)$$

where the first term is the corrected $S/Au_{surface}$ XPS signal, the second term is the ligand to sulfur ratio (1, 1, and 0.5 sulfur atom per MUA, MHA, and TA molecule, respectively), and the third term is the gold atom packing density for a (100) surface plane (12.03 atoms nm^{-2}). Representative XPS spectra are shown in Figure 3.9, and the data are summarized in Table 3.1.

Table 3.1 XPS Data for Au@TA, Au@MHA, and Au@MUA Nanoparticles

	S 2p:Au 4f Peak Ratio	**Packing Density (molecules/cm^2) x 10^{14}**
Au@TA	$0.83_9 \pm 0.01_5$	$2.20_0 \pm 0.03_9$
Au@MHA	$0.89_2 \pm 0.02_7$	$4.58_1 \pm 0.01_9$
Au@MUA	$0.96_3 \pm 0.02_9$	$4.97_5 \pm 0.01_8$

These XPS spectra reveal several important trends in SAM packing density on Au nanoparticles. First, thioctic acid contains the largest binding moiety and as a result, the smallest ligand packing density on nanoparticles versus other SAMs. This value agrees well with previously reported thioctic acid packing densities on ~13 nm gold nanoparticles.[81] Second, 11-mercaptoundecanoic acid and 6-mercaptohexanoic acid form relatively more dense SAMs on the nanoparticles because of their monothiol binding moiety.[189, 200] Third, gold nanoparticles functionalized with 11-mercaptoundecanoic acid contain ~5.0 x 10^{14} molecules/ cm^2, a value similar to what is found in the literature.[215] This relatively high surface coverage arises from superior ligand order for long alkanethiol SAMs. Finally, these data indicate XPS is an excellent quantitative technique and validates that differences in the extinction maxima, flocculation parameter, and zeta potential measurements likely arise from SAM packing density differences on gold nanoparticle surfaces.

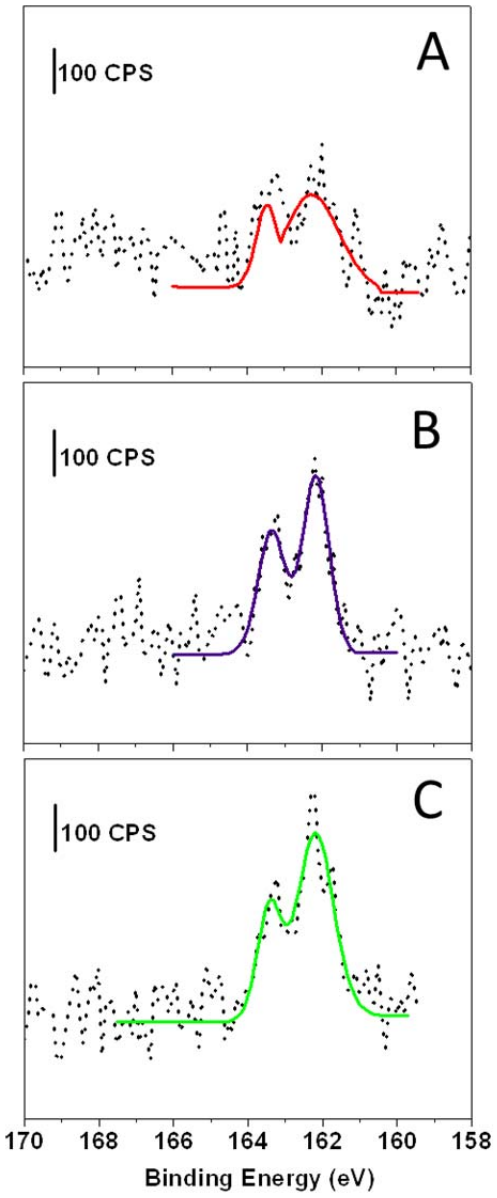

Figure 3.9 XPS characterization of Au@TA, Au@MHA, and Au@MUA nanoparticles. Normalized XPS spectra (S 2p) for (A) Au@TA, (B) Au@MHA, and (C) Au@MUA nanoparticles where the solid and dashed lines correspond to the fitted and raw data, respectively. A S 2p doublet with binding energies of 161 and 163.2 eV are predominate for all three nanoparticle species.

3.4 Conclusions

In conclusion, the surface chemistry on gold nanoparticles impacts their chemical and physical properties. Specifically, gold nanoparticle core shape and, size as well as SAM formation kinetics and ligand packing densities were evaluated. Homogeneous gold nanoparticles were functionalized with either thioctic acid, 6-mercaptohexanoic acid, or 11-mercaptoundecanoic acid. LSPR extinction maxima systematically red shifted with decreasing SAM binding moiety size and increasing ligand chain length. LSPR spectra were monitored as a function of SAM equilibration time which revealed differences in SAM adsorption kinetics. 11-Mercaptoundecanoic acid exhibited the fastest adsorption kinetics vs. both 6-mecaptohexanoic acid and thioctic acid. Specifically, Au nanoparticles exhibited a 1 nm shift in their LSPR spectra in 220, 390, and 550 msec for MUA, MHA, and TA SAMs, respectively. TA binds ~2.5 and 1.4 times more slowly than MUA and MHA, respectively because of the relatively large binding moiety size MHA binds ~1.8 times more slowly than MUA as SAM adsorption efficiency increases with increasing alkanethiol chain length.

Next, the stability of functionalized gold nanoparticles were evaluated using flocculation parameter studies. As solution pH decreased, gold nanoparticles begin to aggregate, and the flocculation parameter increased. The pH at which the flocculation parameter increased which signifies the effective zero point charge or pK_a of the nanoparticles. The longest chain SAM, 11-mercaptoundecanoic acid, exhibited a pK_a which 1) more closely resembles that of free ligand in solution and 2) is most acidic versus either Au@TA nanoparticles or Au@MHA nanoparticles. As a result, Au@MUA nanoparticles are stable down to solution pH values of 5.7 while Au@MHA and Au@TA nanoparticles can be used down to 6.9 and 6.3, respectively.

To better understand these optical and stability differences, ^{1}H NMR was applied to characterize molecules adsorbed to the surface of the gold nanoparticles. Four significant spectral characteristics were observed: (1) peak broadening as a result of

ligand adsorption to the gold nanoparticle surface, (2) no free ligand signatures superimposed on the surface-bound ligand spectra, (3) disappearance of protons peaks associated with thiols for 11-mercaptoundecanoic acid and 6-mercaptohexanoic acid after self assembly, and (4) chemical shift differences between free and surface-bound ligands. Similar observations were made for all three functionalized nanoparticles. In all cases, sulfur groups were orientated closest to the gold surface, and impacts from gold nanoparticles reduced as the distance between the metal and proton increased. Finally, SAM packing density was qualitatively and quantitatively evaluated using zeta potential and XPS, respectively. These data indicate that MUA forms the most dense SAMs on gold nanoparticles, ~8% and ~56% larger than for MHA and TA SAMs, respectively. The combined techniques for nanoparticle characterization reveal similar qualitative and quantitative information regarding nanoparticle structure. Clearly, these surface chemistry differences are important in predicting nanoparticle shelf-life and subsequent applications in relevant nanotechnologies.

CHAPTER 4
MECHANISTIC INVESTIGATIONS OF GOLD NANOPARTICLE STABILITY AND SURFACE FUNCTIONALIZATION IN CAPILLARY ELECTROPHORESIS

4.1 Introduction

Nanometer-sized particles exhibit unique chemical and physical properties that depend on their shape, size, and local environment. Nanoparticles can be combined with separation science to optimize detection,[216-222] facilitate separation of nanoparticles themselves,[223-225] and dramatically improve resolution of target molecules.[109, 226, 227] Furthermore, noble metal nanoparticles both stabilize separation efficiency and decrease electroosmotic flow.[223, 228] The high surface energy of noble metal nanoparticles, however, can induce aggregation in the harsh buffer conditions required for optimized capillary electrophoresis separations.[201] Polymer additives[226, 227] and nanoparticle surface chemistry[24] can improve nanoparticle utility in separation science; however, there is no systematic study that correlates fixed shape and size, nanoparticle concentration, stability, and surface chemistry to analyte mobility in capillary electrophoresis. These studies are limited because nanoparticle parameters are difficult to assess in the dynamic environment of a capillary in an electric field.

One method to understand the function of nanoparticles is by tracking their novel, size-dependent properties. For instance, gold nanoparticles exhibit a strong extinction (absorption + scattering) band that can be tuned throughout visible to near infrared wavelengths.[137] This extinction band results when the incident photon frequency is in resonance with the collective oscillation of the conduction band electrons and is known as the localized surface plasmon resonance (LSPR).[137] Large molar extinction coefficients (~3×10^{11} M^{-1} cm^{-1})[229] are a result of the LSPR and can be used to calculate

the concentration and size of solution-phase nanoparticles[89] as well as to assess nanoparticle aggregation.

To understand the optical properties of gold nanoparticles, material composition, shape, and size as well as local environment must be considered.[230] The local environment includes the surrounding dielectric field with contributions from the solvent, surface molecules as well as other nanoparticles. When the electromagnetic fields from two different nanoparticles interact, a complex LSPR is produced.[231] An important implication of nanoparticle aggregation is shifting of the LSPR to lower energies versus isolated nanoparticles.

Surface chemistry is often used to both prevent disorganized or induce organized aggregation of solution-phase nanoparticles.[232-234] In order to prevent uncontrolled aggregation, nanoparticle surfaces can be modified with capping molecules that form an electrostatically-induced steric barrier.[235] Alternatively, to facilitate controlled nanoparticle aggregation in specific environmental conditions, capping molecules can be assembled onto the surface of the nanoparticles.

Herein, the surface chemistry on gold nanoparticles will be varied and allowed to interact with target molecules during capillary electrophoresis. The nanoparticle pseudostationary phase will comprise only 2% of the total capillary volume which was optimized so the optical properties of the nanoparticles can be easily monitored. The resulting stability of gold nanoparticles will be assessed using dual-wavelength photodiode array (PDA) detection. The mobility of three potential Parkinson's disease biomarkers will be evaluated in the presence of both positively and negatively charged covalently stabilized gold nanoparticles as well as size-matched silica and citrate reduced gold nanoparticles. For covalently functionalized nanoparticles, the effective surface charge impacts the mobility of the biomarkers in a concentration-dependent manner. Positively charged gold nanoparticles will be shown to be more stable and interact more strongly with both the analytes and capillary wall than the negatively charged

nanoparticles in the presence of an electric field. In all cases, the formation of nanoparticle aggregates decreases the migration times of the targeted molecules. We expect that as the nanoparticle pseudostationary phase volume increases, the magnitude of these responses will also increase and therefore be more efficiently implemented in the separation of target chemical and biological species.

4.2 Experimental

4.2.1 Reagents and Chemicals

All chemicals were purchased from Sigma-Aldrich (St Louis, MO) unless otherwise noted. 6-Amino-hexanethiol was purchased from Dojindo Chemicals (Gaithersburg, MD). Silica nanoparticles (diameter, d = 15 nm) were purchased from Nanostructures and Amorphous Materials (Los Alamos, NM). Water was purified to a resistivity greater than 18 MΩ cm^{-1} using a Barnstead Nanopure (Dubuque, IA) water filtration system. Solutions were filtered through 13 mm diameter, 0.45 μm nylon filters from Whatman (Middlesex, UK) prior to use.

Fused silica capillary with an internal diameter of 75 μm, an outer diameter of 360 μm, and an external polyimide coating was purchased from Polymicro (Phoenix, AZ). The total capillary length was 60.2 cm with a 50 cm effective length.

4.2.2 Nanoparticle Synthesis

Prior to synthesis, all glassware were cleaned with aqua regia. Gold nanoparticles were prepared using an established procedure.[135] Briefly, 20 mg of $HAuCl_4$ was dissolved in 50 mL water and brought to a rolling boil while stirring using a reflux condenser. Trisodium citrate (60 mg) was dissolved in water (5 mL) and added to the boiling solution. Initially, the solution turned very dark violet and quickly changed to red. The nanoparticle solution was refluxed for an additional 15-20 minutes, cooled, and stored in a brown bottle until use. A standard estimation model was used to calculate the

concentration of gold nanoparticles.[89] This was achieved and validated in a multi-step process. First, the average nanoparticle diameter was obtained from transmission electron microscopy (TEM). Based on this value, a corresponding molar extinction coefficient (ε) was calculated from the standard estimation model. Next, the nanoparticle concentration was verified using the extinction intensity at 450 nm versus the extinction maximum. For Au@citrate nanoparticles, this concentration was evaluated as 7.8_2 nM.

4.2.3 Nanoparticle Functionalization and Preparation

Functionalized nanoparticles were synthesized by modifying a multi-step procedure.[236] First, citrate molecules on the nanoparticle surface were displaced by thioctic acid. To do this, 0.4 mL of thioctic acid (in ethanol, 10 mM or 4 mM for the carboxylated and amine functionalization, respectively) was added to the previously synthesized citrate-reduced gold nanoparticles in a ratio of 0.1 mL thioctic acid to 1 mL nanoparticles. This solution was stirred overnight so that the reaction could reach equilibrium. The nanoparticles were then centrifuged at 15,000 RPM (14967 x g) for 20 minutes, and the supernatant was discarded. The resulting nanoparticles were resuspended in water to a concentration of 7.8_2 nM.

Au@mercaptohexanoic acid (Au@MHA) nanoparticles were functionalized with 6-mercaptohexanoic acid by first adjusting the pH of the thioctic acid-modified nanoparticle solution to 11 with 1 M NaOH. Next, an ethanolic solution of 10 mM 6-mercaptohexanoic acid was added to the nanoparticle solution in a ratio of 0.1 mL 6-mercaptohexanoic acid to 1 mL nanoparticles and stirred overnight in an ice bath. The resulting carboxylic acid terminated nanoparticles were centrifuged at 15,000 RPM (14,967 x g) for 20 minutes, the supernatant discarded, and the nanoparticles resuspended in water pH adjusted with 1 M NaOH to a concentration of 1.7_4 nM prior to use.

Au@aminohexane thiol (Au@AHT) nanoparticles were functionalized using a similar procedure. In an ice bath, 4 mM 6-amino-1-hexanethiol (in ethanol) was added to

thioctic acid stabilized nanoparticles without adjustment of solution pH (in a ratio of 0.1 mL 6-amino-hexanethiol to 1 mL nanoparticles). Within five minutes, the nanoparticle solution turned from burgundy to purple. After one hour, 1 M HCl (0.1 mL 1 M HCl to 1 mL nanoparticles) was added and the nanoparticle solution immediately changed to burgundy. This solution was stirred overnight in an ice bath. Next, the resulting solution was centrifuged at 15,000 RPM (14,967 x g) for 20 minutes, the supernatant discarded, and the nanoparticles resuspended in water pH adjusted to 2 with 1 M HCl to a (nanoparticle) concentration of 1.3_1 nM prior to use. Varying nanoparticle concentrations were obtained by either diluting the nanoparticles in separation buffer or by preconcentrating the nanoparticles via centrifugation (15,000 RPM (14,967 x g) for 20 minutes) and resuspension in buffer. Silica nanoparticles were suspended in water to a stock concentration of 7.8_2 nM and diluted to the desired concentration in separation buffer.

4.2.4 Buffer Preparation

50 mM tetraborate buffer (pH 9.3) was prepared using boric acid and sodium tetraborate. The pH was adjusted with 1 M NaOH. The separation buffer was prepared by diluting this stock solution to a concentration of 10 mM tetraborate. All buffers were filtered prior to use.

4.2.5 Sample Preparation

Three potential Parkinson's disease biomarkers (dopamine, epinephrine, and pyrocatechol) were used in these studies. Stock solutions (5 mM) of each were made in 10 mM tetraborate buffer. These samples were diluted to a final concentration of 50 μM in the same buffer and filtered prior to use.

4.2.6 Capillary Conditioning

The capillary was conditioned prior to each run as follows. First, the capillary was rinsed with 0.1 M HNO_3 (20 psi for 5 minutes), water (20 psi for 2.25 minutes), 1 M NaOH (20 psi for 2.25 minutes), water (20 psi for 2.25 minutes), and 50 mM sodium tetraborate buffer (20 psi for 2.25 minutes). The capillary was then filled with the separation buffer (20 psi for 3 minutes) prior to each separation.

4.2.7 Capillary Electrophoresis

All separations were performed with a Beckman Coulter PACE-MDQ capillary electrophoresis instrument equipped with a UV detector, photodiode array (PDA) detector, and capillary cooling. The capillary temperature was maintained at 25° C. UV detection occurred at 214 nm, and PDA detection occurred at both 520 nm and 600 nm. The instrument was utilized per manufacturer recommendations.

The neurotransmitter sample and nanoparticle solution were injected sequentially into the capillary to reduce possible nanoparticle instability caused by the molecules. The injection scheme for these materials was as follows: 5 seconds (1 psi) nanoparticles, 1 second (1 kV) buffer, and 10 seconds (10 kV, normal polarity) biomarkers. The buffer plug was used to minimize cross-contamination between sample vials. Separations were performed by applying a voltage of 20 kV (normal polarity) across the capillary.

Each experiment was performed in triplicate. Separations were performed in increasing nanoparticle concentration to reduce complications that might arise from nanoparticle effects in the capillary between runs. Data were analyzed using OriginPro 7.5 and Grams AI 7.0. Data shown in electropherograms were normalized to account for slight variations in buffer and sample matrix. Normalization was performed by adjusting the migration time of epinephrine from the first run of the day to its average migration time for a series of control experiments in the absence of nanoparticles. The same

adjustment factor was subsequently applied to all data from that day. The PDA data were smoothed using a first order Savitzky-Golay fit (20 point window).

4.2.8 UV-Visible (UV-Vis) Spectroscopy

The optical properties and the overall stability of the gold nanoparticle solutions were evaluated in water and buffer using UV-Vis spectroscopy (USB4000, Ocean Optics, Dunedin, FL).

4.2.9 Zeta Potential

The effective surface charges on the gold nanoparticles were measured using zeta-potential (Malvern Instruments Zetasizer, Worcestershire, UK). The reported zeta potential measurements were collected in separation buffer at 1.9_6 nM Au@citrate, 1.9_6 nM silica, 1.7_7 nM Au@MHA, and 0.6_5 nM Au@AHT concentrations. Data were obtained using a monomodal acquisition and fit according to the Smoluchowski theory.

4.2.10 Transmission Electron Microscopy (TEM)

Nanoparticle homogeneity was characterized using TEM (JEOL JEM-1230). In all cases, ~2 μL of diluted nanoparticle solution (50% mixture in ethanol) was applied to a carbon-formvar coated copper grid (400 mesh, Ted Pella, Redding, CA) and allowed to air dry. Any remaining solution was removed with filter paper prior to TEM analysis.

4.3 Results and Discussion

4.3.1 Bulk Optical and Charge Characterization of Gold Nanoparticles

The LSPR of gold nanoparticles[135] was previously exploited to assess the degree of nanoparticle stability as a function of surface chemistry and local environment. As shown from TEM data in Figure 4.1A, citrate reduced gold nanoparticles (Au@citrate) exhibit an average diameter of 13.3 ± 0.6 nm. Zeta potential measurements reveal the

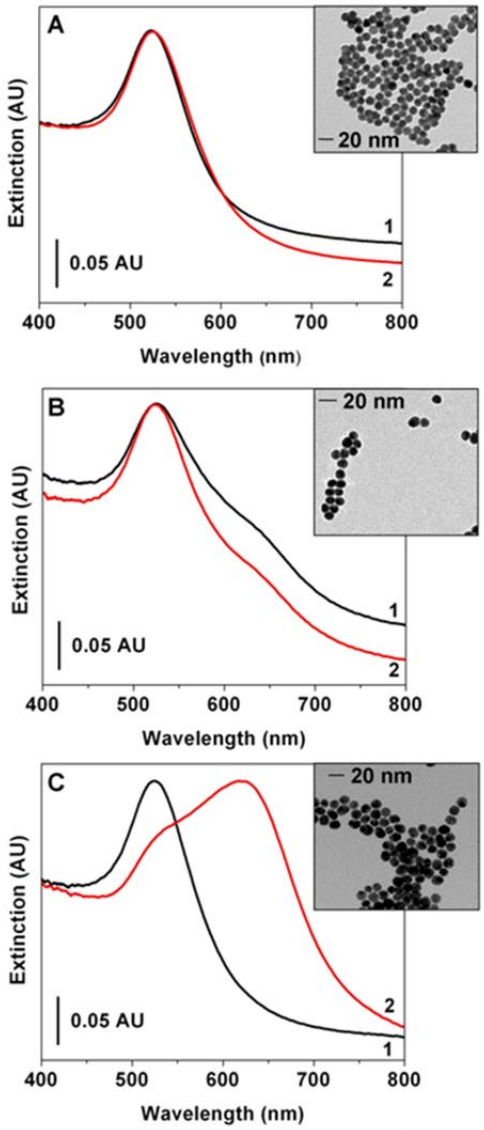

Figure 4.1 Characterization of gold nanoparticles using LSPR spectroscopy and TEM (inset). (A) Au@citrate (d = 13.3 ± 0.6 nm) exhibit an extinction maximum located at (1) 523.3 nm in water and (2) 524.8 nm in buffer. (B) Au@MHA (d = 10.9 ± 1.8 nm) exhibit an extinction maximum located at (1) 521.5 nm in water and (2) 522.3 nm in buffer with a slight shoulder located ~625 nm in both spectra. (C) Au@AHT (d = 13.8 ± 2.0 nm) exhibit an extinction maximum located at (1) 524.0 nm in water and (2) 617.5 nm with a shoulder at the original extinction maximum ~525 nm in buffer. In all buffer spectra, 10 mM tetraborate buffer (pH = 9.3) is used.

nanoparticles are highly stable and possess an average surface charge of -39.7 ± 0.7 mV at pH 9.3. Evaluation of the nanoparticle optical properties support the stability indicated by the zeta potential measurements. The extinction data clearly demonstrate the stability of Au@citrate nanoparticles in both water and buffer (Figure 4.1A-1 and 4.1A-2).

Despite the high degree of stability in bulk solution, Au@citrate nanoparticles are extremely unstable inside a capillary.[101, 217] As a result, the electrostatically-attached citrate molecules were modified using a more stable and covalently-bound surface functionalization.[24, 236] First, the citrate on the gold nanoparticle surface is replaced by thioctic acid. This step improves nanoparticle stability and reduces uncontrolled aggregation which typically occurs in direct exchange reactions. Subsequently, the easily displaced thioctic acid group is replaced by either 6-mercaptohexanoic acid (Au@MHA) or 6-amino-hexanethiol (Au@AHT) to form two "types" of nanoparticles with mixed monolayers but distinct surface chemistries (Figure 4.2).

As shown in Figure 4.1B, Au@MHA nanoparticles exhibit a similar extinction maximum that is centered at ~522 nm in both water and buffer. In both solutions, a slight shoulder is observed at ~615 nm and is characteristic of reduced interparticle distances and increased electromagnetic coupling between nanoparticles. In comparison to Au@citrate nanoparticles, Au@MHA nanoparticles are slightly smaller (average diameter = 10.9 ± 1.8 nm) and exhibit a zeta potential that is slightly less negative (-36.4 ± 2.0 mV at pH 9.3). For carboxylic acid terminated monolayers, the surface pK_a ranges from 5 to 8 versus 4 to 5 (for free ligand) in solution.[237, 238]

Representative extinction spectra and a TEM image for Au@AHT nanoparticles are shown in Figure 4.1C. In contrast to both Au@citrate and Au@MHA nanoparticles, Au@AHT nanoparticles exhibit a large degree of instability in buffer (pH 9.3) which is supported by an average zeta potential equal to 5.9 ± 0.2 mV at pH 9.3. It should be noted that as the zeta potential approaches zero, inherent nanoparticle stability worsens.

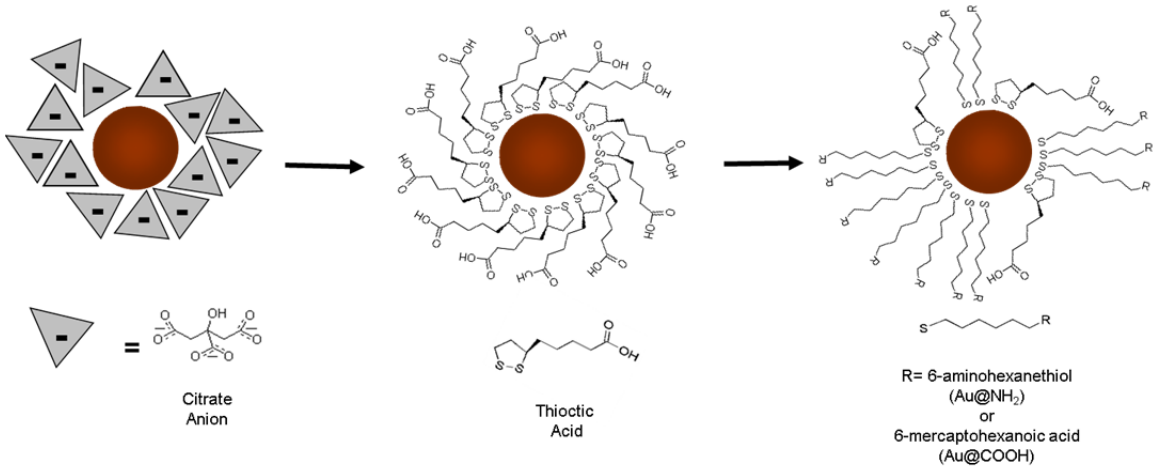

Figure 4.2 Modifying nanoparticle surface chemistry. Gold nanoparticles stabilized with citrate were functionalized with thioctic acid. The thioctic acid on the gold nanoparticles were subsequently exchanged with either 6-mercaptohexanoic acid (Au@NH2) or 6-aminohexanethiol (Au@COOH). Drawing is not to scale.

Importantly, the surface pK_a for amine terminated nanoparticles ranges from 4 to 6 or ~2 - 4 units lower than the solution pK_a values.[239-241]

Clearly, surface pK_a values are important for the ultimate stability of nanoparticles in solution. At pH 9.3, the amine groups will be more protonated with an overall positive surface charge, a result supported by positive zeta potential measurements for Au@AHT nanoparticles. The effective Au@AHT nanoparticle surface charge arises from both the exchanged amine molecules (6-amino-hexanthiol) and the remaining unexchanged molecules (thioctic acid) yielding ~65-70% amine group surface coverage (estimated from zeta potential measurements).

4.3.2 Evaluation of Gold Nanoparticle Stability in a Capillary

Identifying whether solution-phase nanoparticle are reversibly (agglomerated) or irreversibly (aggregated) interacting is important in understanding nanoparticle function. As shown in Figure 4.1, if the majority of the nanoparticles are in an isolated form, Au nanoparticles will absorb strongly at 520 nm and weakly at 600 nm. By taking the ratio of the absorbance (R) at both wavelengths as follows:

$$R = \frac{\text{Absorbance}_{520}}{\text{Absorbance}_{600}} \tag{4.1}$$

where Absorbance_{520} = absorbance collected at 520 nm and Absorbance_{600} = absorbance collected at 600 nm, nanoparticle stability can be quantified. For highly stable or isolated nanoparticles (i.e. Figure 4.1C-1), R = ~3.5-4. When nanoparticles electromagnetically couple, the ratio decreases and will eventually approach 0.

While photodiode array (PDA) detector sensitivity is poor (versus UV detection) and the extinction cross sections for isolated and aggregated nanoparticles vary with size and local dielectric environment, the large magnitude of the nanoparticle extinction cross section permits the detection of nanoparticles down to ~600 pM in a capillary (S/N ~4+).

Furthermore, the combination of capillary electrophoresis with multi-wavelength PDA detection provides for the separation and detection of aggregates from isolated nanoparticles.

As shown in Figure 4.3A-i, when a 2% total volume plug length of 1.5 nM Au@MHA is injected into a capillary, a band with a migration time = 6.1 minutes is observed in the electropherograms collected at both 520 and 600 nm. Using Equation 4.1, the ratio between these band areas is determined at ~3.8. To improve the characterization of nanoparticles both outside and inside the capillary, a new attribute called the "critical nanoparticle concentration" (CNC) is defined. The CNC, a parameter similar to the critical micelle concentration in micellar electrokinetic chromatography (MEKC), is the lowest concentration of nanoparticles that induces dominant nanoparticle aggregation (versus stable nanoparticles) under specific buffer conditions. Experimentally, the CNC is defined by a value of ratio band areas (Equation 4.1) at 50% the total value for isolated nanoparticles.

When Au@MHA nanoparticle concentration is increased to 2.5 nM, three notable differences are observed in the resulting electropherograms (Figure 4.3A-ii) versus the lower nanoparticle concentration (Figure 4.3A-i). First, as expected, the nanoparticle band intensities at both 520 and 600 nm increase. Second, two bands with varying migration times (6.1 and 6.4 minutes) are detected at the two wavelengths. This indicates multiple nanoparticle species are being detected. Finally, the band shape in Figure 4.3A-ii (600 nm) is significantly broader than Figure 4.3A-ii (520nm), characteristic of a distribution of aggregates.

Determination of the CNC for Au@MHA nanoparticles is shown in Figure 4.3B. As nanoparticle concentration increases, the area for the band centered at 6.1 minutes (band 1) decreases while an area increase in the second band centered at 6.4 minutes (band 2) is observed. Using Equation 4.1, band 1 maintains an R values of 3.8, a value

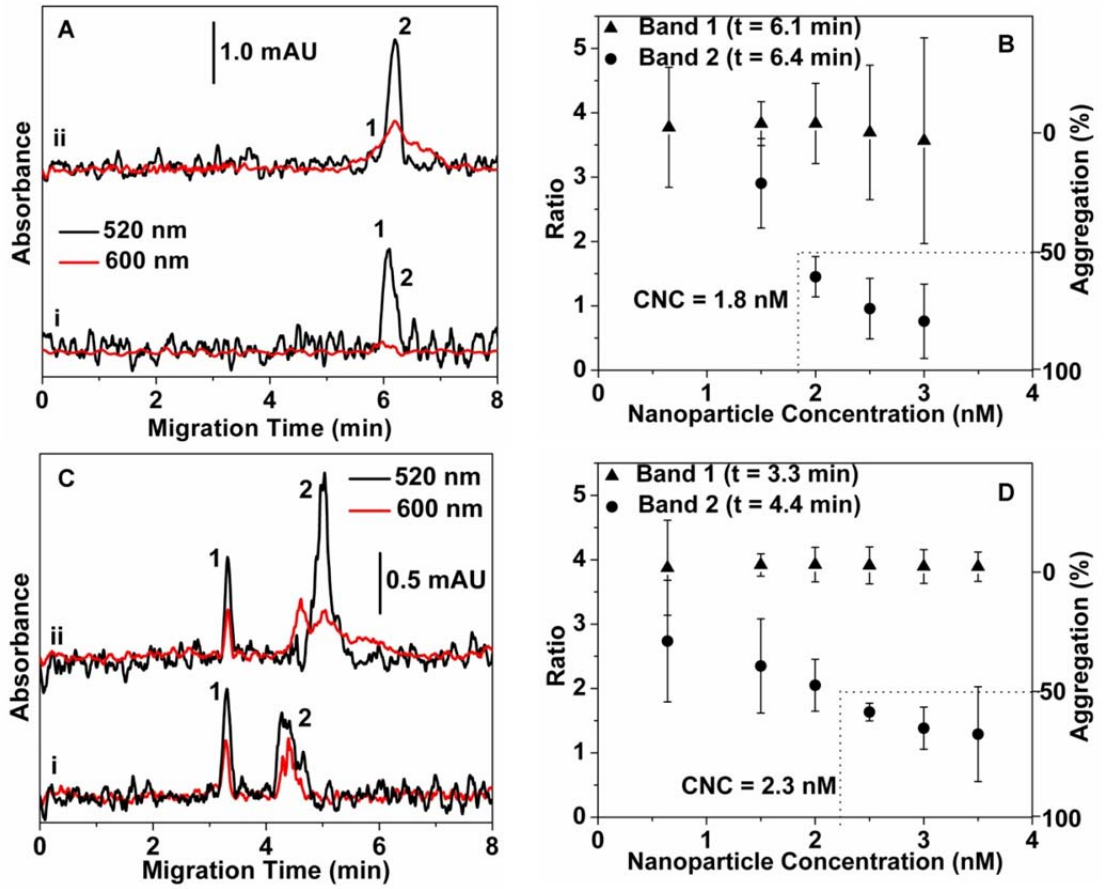

Figure 4.3 Dual-wavelength PDA detection of nanoparticles in a capillary. (A) Representative electropherograms for (i) 1.5 nM Au@MHA nanoparticles at λ_{det} = 520 nm (band 1 S/N = 12.4 and band 2 S/N = 6.8) and λ_{det} = 600 nm (band 1 S/N = 7.4 and band 2 S/N = 4.0). Representative electropherograms for (ii) 2.5 nM Au@MHA nanoparticles at λ_{det} = 520 nm (band 1 S/N = 3.0 and band 2 S/N = 19.4), and λ_{det} = 600 nm (band 1 S/N = 8.0 and band 2 S/N = 18.9). (B) Determination of the CNC of Au@MHA nanoparticles. (C) Representative electropherograms for (i) 1.5 nM Au@AHT nanoparticles at λ_{det} = 520 nm (band 1 S/N = 16.1 and band 2 S/N = 11.1) and λ_{det} = 600 nm (band 1 S/N = 17.6 and band 2 S/N = 16.9). Representative electropherograms for (ii) 3.5 nM Au@AHT nanoparticles at λ_{det} = 520 nm (band 1 S/N = 12.0 and band 2 S/N = 21.0) and λ_{det} = 600 nm (band 1 S/N = 15.4 and band 2 S/N = 18.3). (D) Determination of the CNC of Au@AHT nanoparticles. In panels B and D, average areas for bands 1 and 2 were measured via integration techniques. Error bars represent propagated error from a minimum of three electropherograms.

characteristic of isolated nanoparticles. As nanoparticle concentration increases, band 2 area decreases from 2.9 ± 0.7 (at 1.5 nM) to 0.8 ± 0.6 (at 3.0 nM) As a result; band 2 is attributed to nanoparticle aggregates. From these data, the CNC is estimated at 1.8 nM.

When Au@AHT nanoparticles are injected into the capillary; surface chemistry-dependent migration times are observed. At all concentrations studied, bands centered at 3.3 and 4.4 minutes are detected at 520 and 600 nm. Using Equation 4.1, for 1.5 nM Au@AHT (Figure 4.3C-i); R = 3.9 ± 0.2 for band 1 and agrees with the extinction intensity ratio outside the capillary. This result indicates nanoparticles are behaving as isolated instead of as aggregated/flocculated nanoparticles as their characterization outside the capillary suggests. The ratio for band 2 is 2.3 ± 0.7 indicating some degree of aggregation is occurring.

At higher concentrations of Au@AHT nanoparticles (3.5 nM), PDA measurements reveal similar band shapes at 520 and 600 nm (Figure 4.3C-ii). With increasing nanoparticle concentrations, band 1 displays a migration time of ~3.3 minutes and a ratio = 3.9 ± 0.2 while maintaining similar shapes at both detected wavelengths. Band 2, however, exhibits obvious differences in both relative absorbance area and shape versus lower nanoparticle concentrations. Notably, band shape is highly dependent on detection wavelength. For example in Figure 4.3C-i, band 2 is significantly broader at 600 nm versus 520 nm indicating detection of a heterogeneous distribution of nanoparticle aggregates.

The CNC for Au@AHT nanoparticles is determined in Figure 4.3D. Similar to Au@MHA nanoparticles, Au@AHT nanoparticles reveal concentration dependent trends in the ratio data for both bands 1 and 2. For all concentrations studied, band 1 maintains a ratio for ~3.9 indicative of isolated nanoparticles. The ratio of band 2, however, decreases with increasing concentration. Here, the CNC is estimated at 2.3 nM, a result surprising given the instability of these nanoparticles outside the capillary.

Clearly, differences in nanoparticle surface chemistries are observed. Despite injections of equal concentrations, the Au@AHT nanoparticles exhibit ~one-half the overall PDA-collected absorbance intensity versus Au@MHA nanoparticles. This could indicate three different phenomena. Au@AHT nanoparticles are more likely to (1) interact with the capillary wall, (2) diffuse through the capillary below the detection limit of the PDA detector, and/or (3) exhibit injection problems versus Au@MHA nanoparticles. Dark-field microcopy reveals that the nanoparticles are not visibly attached to the capillary walls (data not shown). Similar current changes (in amperes) are observed when the nanoparticle plug exits the capillary suggesting that the Au@AHT nanoparticles more freely diffuse along the capillary wall than the Au@MHA nanoparticles thereby resulting in lower signal strengths.

4.3.3 Impact of Nanoparticle Functionality and CNC on the Separation of Parkinson's Disease Biomarkers

Parkinson's disease is a neurodegenerative disorder affecting approximately 1% of the population over 60 years of age in the United States.[242] The disease is characterized by slowness of movements (bradykinesia), balance problems, and rigid movement.[243] Currently, Parkinson's diagnosis relies on the exhibition of cardinal symptoms and positive response to drug therapy. Because there is no definitive tests for Parkinson's disease and because symptoms are similar to other neurological disorders, misdiagnosis rates are high. Recent research, therefore, focuses on the identification and detection of potential Parkinson's disease biomarkers for improved diagnosis. [244, 245]

Nanoparticles with tailored surface chemistry can act as pseudostationary phases in capillary electrophoresis to improve the detection of Parkinson's disease biomarkers. To investigate the impact nanoparticles exhibit on potential Parkinson's disease biomarkers mobility, a 2% plug of the total capillary volume of Au@MHA and Au@AHT nanoparticles as well as a size-matched silica and Au@citrate nanoparticle

controls were injected into a capillary at various concentrations prior to a plug of three potential Parkinson's disease biomarkers (dopamine, epinephrine, and pyrocatechol). The nanoparticles travel more slowly than the biomarkers thereby serving as a pseudostationary phase. In all cases, the elution order is (d) dopamine, (e) epinephrine, and (p) pyrocatechol (Figure 4.4).

Trends in these data are clear when the migration time of only one biomarker is analyzed. In Figure 4.5, the migration time of the pyrocatechol band remains statistically constant upon the addition of either silica or Au@citrate nanoparticles (Figure 4.5A and 5B, respectively). Upon increasing the concentration of Au@MHA nanoparticles, the migration time of pyrocatechol increases until the CNC is exceeded (Figure 4.5C). Uncontrolled aggregation occurs and the capillary clogs when the CNC is achieved. In contrast, as Au@AHT nanoparticle concentration increases: pyrocatechol migration times decrease (Figure 4.5D). This is the first demonstration of increasing analyte mobility with nanoparticles! It should be noted that these trends are similar for each biomarker used in this study.

At least three mechanisms are hypothesized to influence this separation. First, Au@AHT nanoparticles exhibit a higher CNC than the other nanoparticles studied, and this improved in-capillary stability leads to more reproducible separations. This likely arises because the nanoparticles reversibly interact outside the capillary and once inside the capillary, form a mobile viscous layer at the capillary surface versus the negatively charged nanoparticles (*vida infra*). Second, the effective "positive" surface charges on the Au@AHT nanoparticles are more strongly attracted to the negative anode and negatively charged (and neutral) biomarkers. This leads to both localized increases in the electroosmotic flow in the capillary and to a larger influence on analyte mobility, respectively. Finally, the positively charged Au@AHT nanoparticles are more strongly attracted to the capillary wall than the other nanoparticles studied. While the

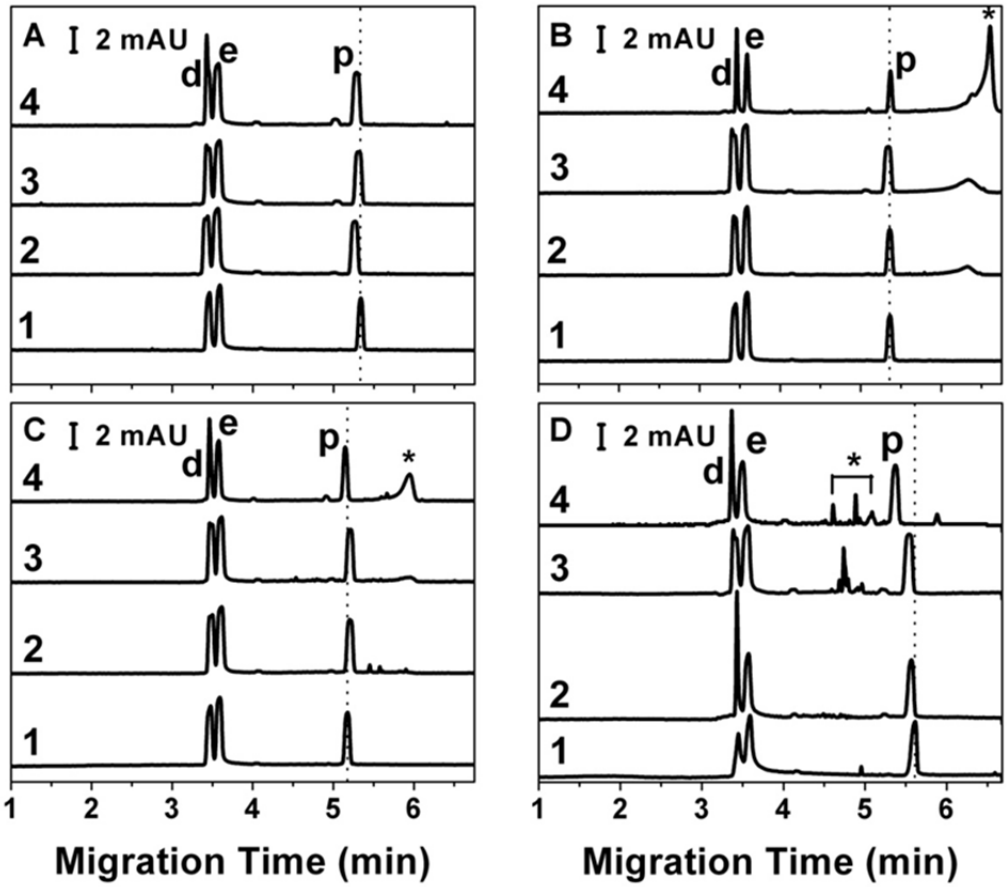

Figure 4.4 Effect of increasing nanoparticle concentration on the separation of dopamine (d), epinephrine (e), and pyrocatechol (p). (A) Representative electropherograms in the presence of (1) 0, (2) 0.71, (3) 1.30, and (4) 3.91 nM silica nanoparticles. (B) Representative electropherograms in the presence of (1) 0, (2) 0.71, (3) 1.30, and (4) 3.91 nM Au@citrate nanoparticles. (C) Representative electropherograms in the presence of (1) 0, (2) 0.64, (3) 1.18, and (4) 3.54 nM Au@MHA nanoparticles. (D) Representative electropherograms in the presence of (1) 0, (2) 0.64, (3) 1.18, and (4) 3.54 nM Au@AHT nanoparticles. In each case, nanoparticle bands are starred. 10 mM tetraborate buffer (pH = 9.3) is used and the "sample" injection order is nanoparticles (1 psi for 5 s), buffer (1 kV for 1 s), and neurotransmitters (10 kV for 10 s). Separation voltage = 20 kV, λ_{det} = 214 nm.

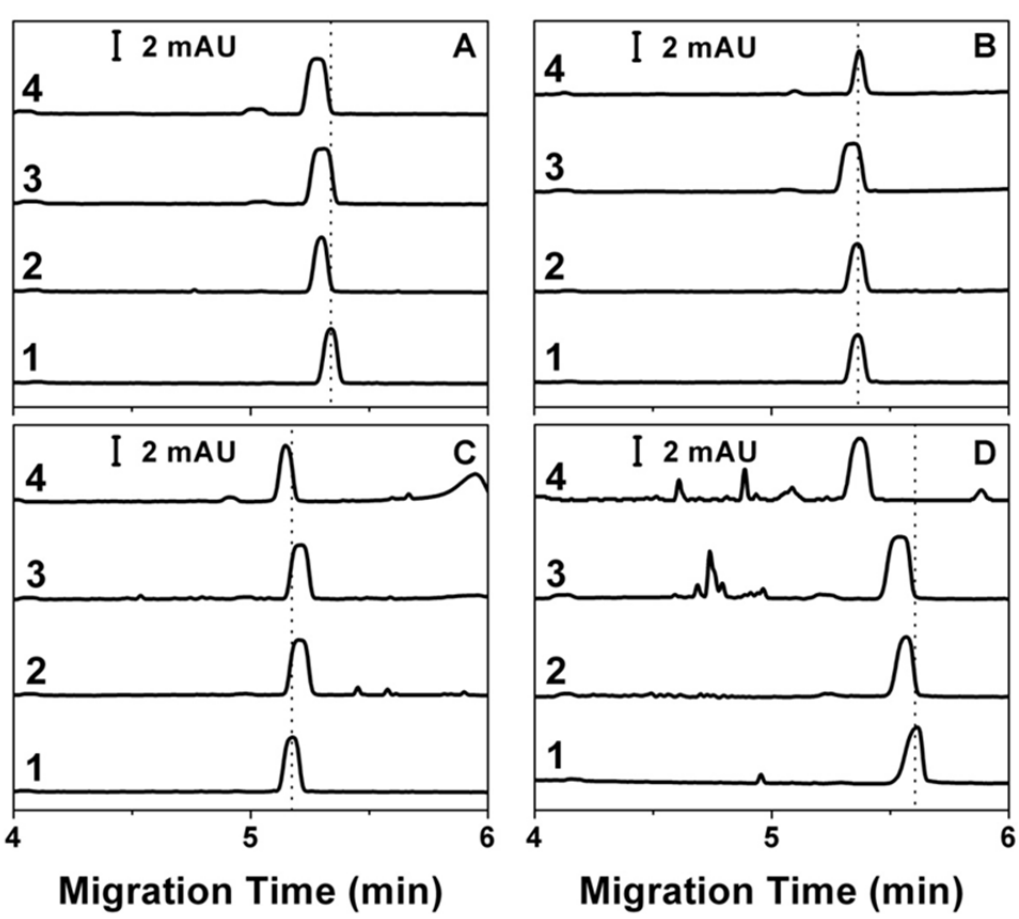

Figure 4.5 Evaluation of trends in the migration time of pyrocatechol as a function of nanoparticle concentration. Representative electropherograms in the presence of (A) silica, (B) Au@citrate, (C) Au@MHA, and (D) Au@AHT nanoparticles. Identical nanoparticle concentrations and separation conditions described in Figure 4.4 are used.

nanoparticles do not bind irreversibly to the capillary wall, a dilution effect is likely occurring as observed with the PDA measurements.

Finally, Figure 4.6 shows how nanoparticle concentration and functionalization impact the mobility of dopamine. Au@MHA nanoparticles experience a slight retarding effect while Au@AHT nanoparticles clearly decrease the migration time of the same molecule (dopamine). Closer examination of these mobility changes reveal that while the negatively charged Au@MHA nanoparticles systematically decrease the analyte mobility, the changes in mobility are not significantly different among the various nanoparticle concentrations studied. When Au@AHT nanoparticles are included in the separation, the neurotransmitter mobility significantly increases as determined from 95% confidence interval and t-test analyses.

4.3.4 Evaluation of Mobility Variations of Parkinson's Disease Biomarkers in the Presence of Covalently-Functionalized Nanoparticles

The inherent mobility of the hypothesized Parkinson's disease biomarkers is likely dependent on both (1) variations in Au@AHT nanoparticle concentration as well as (2) composition (i.e. versus Au@MHA nanoparticles). When nanoparticles are included in a separation, the electrophoretic mobility of a charged molecule may change and can be approximated using the Debye-Hückel-Henry theory:

$$\mu = \frac{q}{6\pi\eta r} \tag{4.2}$$

where q is the charge on the species, η is the viscosity of the surrounding buffer, and r is the radius of the species.[246] This means that the charge of the molecule, the size of the molecule, or the viscosity of the buffer must change if the electrophoretic mobility of a molecule varies. The effective charge and size of the biomarkers remain constant

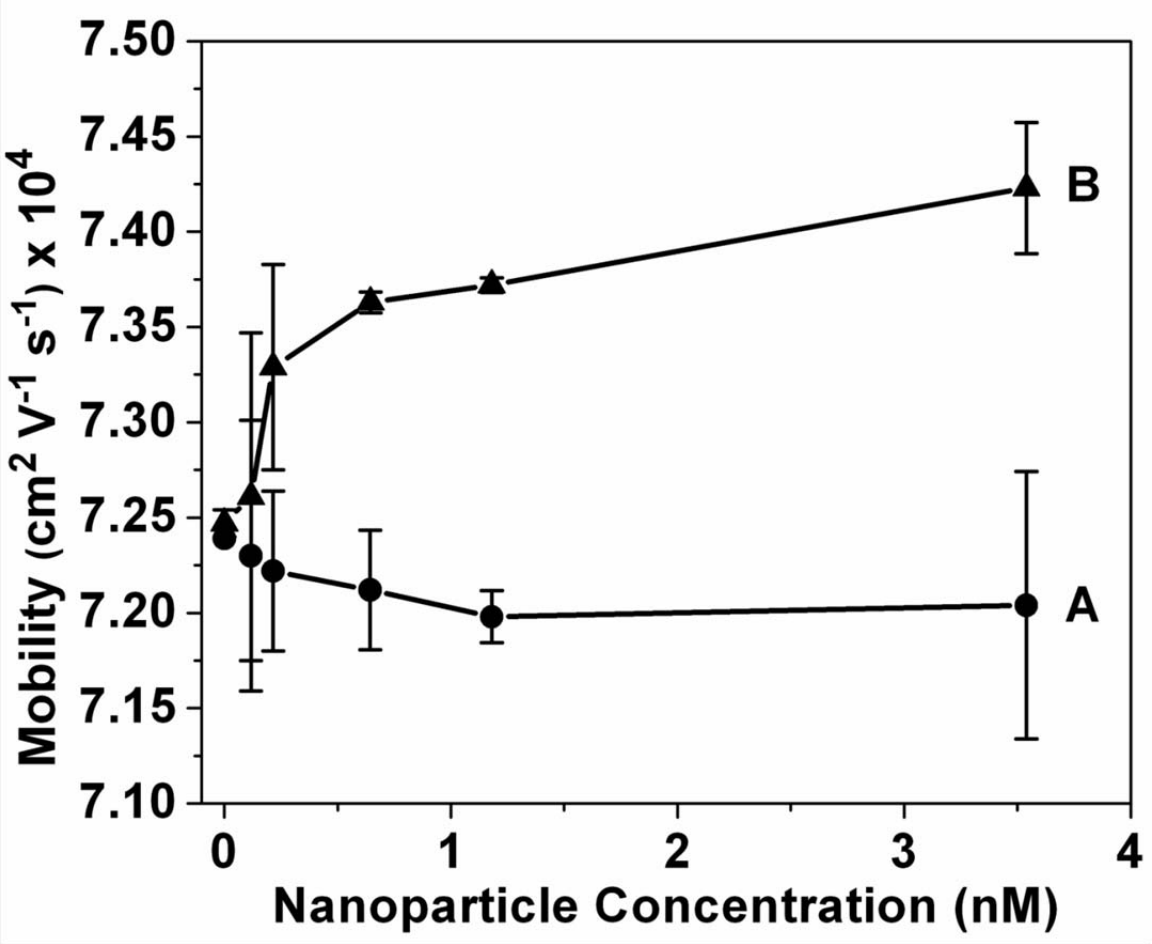

Figure 4.6 Comparison of dopamine mobility versus nanoparticle concentration. Increasing concentrations (0 – 3.54 nM) of Au@MHA and Au@AHT nanoparticles reveal opposite effects on dopamine mobility. (A) Increasing the concentration of Au@MHA nanoparticles slightly decreases the mobility of dopamine. (B) Increasing the concentration of Au@AHT nanoparticles increases the mobility of dopamine. Error bars represent the spread in the data. The lines in the plot are included to guide the eye.

regardless of nanoparticle inclusion. Consequently, buffer viscosity must increase if an increase in the electrophoretic mobility of the molecules is observed.

Similar to a dynamic coating,[246] nanoparticles must reach a steady-state interaction with both molecules and the capillary wall. As observed in Figure 4.6A, below the CNC, the error in dopamine mobility decreases with increasing Au@MHA nanoparticle concentration. We hypothesize that because these negatively charged nanoparticles are weakly attracted to the capillary wall, and a steady-state equilibrium is not reached thereby resulting in large deviations in observed analyte mobility. As the nanoparticle concentration increases, a steady-state environment[247] is achieved more efficiently, and the separation becomes systematically more reproducible until aggregation dominates.

The positively charged Au@AHT nanoparticles, on the other hand, are more strongly attracted to the capillary wall and achieve a steady-state much more quickly than the negatively charged Au@MHA nanoparticles. As observed in Figure 4.6B, when 0.6_4 nM Au@AHT nanoparticles are included, the mobility of dopamine is highly irreproducible; however, the reproducibility of the separation is greatly improved when the nanoparticle concentration exceeds 1 nM but is less than the CNC. The readily formed nanoparticle containing viscous layer at the capillary wall will increase the mobility of the molecules as observed in Figure 4.6B.

Importantly, the nanoparticle pseudostationary phases used in these studies occupies less than 2% of the total capillary volume. Just as the viscous nanoparticle layer near the capillary is formed because of the dynamic nature of the system, it will also be destabilized because the injected nanoparticle plug occupies only 2% of the total capillary volume. As the length of the nanoparticle pseudostationary phase increases, impacts on analyte mobility will likely increase. Furthermore, these results will likely be magnified as nanoparticle concentration and/or plug length are increased.[226, 227]

4.4 Conclusions

In summary, the optical properties of covalently functionalized gold nanoparticles used to investigate nanoparticle stability as well as the mobilities of dopamine, epinephrine, and pyrocatechol in capillary electrophoresis. The nanoparticle pseudostationary phase comprised only 2% of the total capillary volume allowing the optical properties of aggregated and isolated nanoparticles to be easily distinguished. The stability of both amine and carboxylated gold nanoparticles was determined using extinction spectroscopy and zeta potential measurements outside the capillary. Inside the capillary, the lowest nanoparticle concentration which induced aggregation (i.e. CNC) was subsequently evaluated using dual wavelength PDA detection.

These findings demonstrate that effective nanoparticle surface charge impacts interactions of nanoparticles with analytes, the capillary wall, and other nanoparticles. These interactions directly influence the mobility of the nanoparticles. Furthermore, the mobilites of the studied Parkinson's disease biomarkers increase in the presence of aminated nanoparticles but decrease slightly with carboxylated nanoparticles. Below the CNC, this observation is dominated by the formation of a mobile pseudostationary phase at the capillary wall which is hypothesized to increase local buffer viscosity. The presented approach of exploiting nanoparticle behavior in the presence of an electric field will have significant impacts in separation science where nanoparticles are employed. Further investigations will lead to more controlled improvements in the separation and detection of target biological and chemical species.

CHAPTER 5
GOLD NANOPARTICLE SURFACE CHEMISTRY EFFECTS IN CAPILLARY ELECTROPHORESIS

5.1 Introduction

Capillary electrophoresis (CE)[1-3] is an effective technique for the liquid-phase separation of molecules ranging from metal ions[4] to biomolecules such as DNA.[5, 6] CE separation modes[7] utilize small sample volumes (nanoliter injection volumes)[8] and high separation selectivities.[9] These electrically driven separations are achieved by applying a large potential to charged solution-phase molecules. Electrophoretic separations of charged species occur because (1) anions and cations migrate in opposite directions toward electrodes of opposite charge and (2) similarly charged ions with varying Stokes radii exhibit different migration velocities.[10]

Both pseudostationary (i.e. matrices which can either co-migrate with or migrate against the mobile phase) and stationary phases (i.e. non-moving matrices) are implemented to improve separation selectivity.[11-13] Pseudostationary or stationary phases can include nanomaterials to further improve selectivity.[24, 25] Nanomaterials possess ideal properties for integration in this manner. These nanomaterials are inherently "small" - that is, contain at least one dimension less than 100 nm and can be included at low concentrations compared to traditional pseudostationary or stationary phases such that less than 1% of the total capillary volume is occupied by nanoparticles.[26] Second, nanomaterials exhibit inherently large surface area to volume ratios and novel size dependent chemical and physical properties.[27, 28]

Although nanomaterials are used as pseudostationary and stationary phases to improve selectivity, previous studies revealed that nanomaterial surface chemistry is important during electrically driven separations.[248, 249] Furthermore, the electrophoretic mobility of nanoparticles in an electrolyte solution is a powerful tool in determining the

usefulness of nanoparticle pseudostationary phases in capillary electrophoretic separations.[250-252]

Herein, we will measure the current differences when an electric field is applied across a nanoparticle containing buffer. Furthermore, the forces that act on nanoparticles when a high field strength is applied across a capillary containing covalently functionalized gold nanoparticles are modeled. Spherical gold nanoparticles (diameter, d = 12.7 ± 1.1 nm) functionalized with 11-mercaptoundecanoic acid (MUA, solution pK_a = 4.6 - 5.0),[211] 6-mercaptohexanoic acid (MHA, solution pK_a = 4.8),[207] and thioctic acid (TA, solution pK_a = 4.75 - 5.3)[208] will be used. Separations will be performed using 5.5 mS cm^{-1} pH 7.3 phosphate separation buffer which contains the functionalized Au nanoparticles. This novel investigation reveals important surface chemistry trends. First, nanoparticle attributes such as stability and self assembled monolayer (SAM) packing density are evaluated. Extended Derjagvin-Landau-Verwey-Overbeek (DLVO) and electron tunneling theories will be used to model interparticle interactions between the functionalized nanoparticles. The most experimentally and theoretically stable nanoparticles (Au@MUA) suppress current, while Au@MHA and Au@TA nanoparticles enhance the current observed during electrically driven flow. It is hypothesized that the surface chemistry on both Au@MHA and Au@TA nanoparticles facilitates aggregation and electron tunneling effects thereby increasing currents. Au@MUA nanoparticles are stabilized by an energy barrier at separation distances less than 1.5 nm which prohibits nanoparticle aggregation and tunneling effects. Whether the current is suppressed or enhanced, nanoparticle concentration will be shown to be important where concentrations above the critical nanoparticle concentration (CNC)[106] results in irreproducible effects. These studies will help to improve further investigations of nanomaterial pseudostationary and stationary phase effects in CE separations.

5.2 Experimental

5.2.1 Synthesis of Carboxylic Acid Functionalized Gold Nanoparticles

Citrate stabilized gold (Au@citrate) nanoparticles were synthesized according to an established procedure[106] using glassware cleaned with aqua regia and rinsed prior to nanoparticle synthesis. First, 20 mg of $HAuCl_4$ was dissolved in 50 mL water and brought to a rolling boil while stirring using a reflux condenser. Trisodium citrate (60 mg) was dissolved in water (5 mL) and added to the boiling solution. The solution was refluxed for an additional 15-20 minutes. After cooling, the resulting nanoparticle solution was stored in a brown bottle. Nanoparticle solutions were filtered through 13 mm diameter, 0.45 μm nylon filters (Whatman, Middlesex, UK) prior to additional functionalization.

Next, Au@citrate nanoparticles were functionalized with either 6-mercaptohexanoic acid (MHA), thioctic acid (TA), or 11-mercaptoundecanoic acid (MUA). First, 1 mL of 10 mM ligand (MHA, TA, or MUA) in ethanol was added to 10 mL of a 10 nM Au@citrate nanoparticle solution. This solution was stirred at 500 RPM for at least 60 hours at room temperature. The nanoparticles were then centrifuged at 11,500 RPM (8,797 x g) for 40 minutes, and the supernatant was replaced with water (pH adjusted to 11 with 1 M NaOH). The rinsing procedure was repeated three times to ensure sufficient removal of unbound ligand. The nanoparticles were stored in a brown vial prior to use.

5.2.2 Transmission Electron Microscopy (TEM)

Nanoparticle homogeneity was characterized by TEM using a JEOL JEM-1230. In all cases, 2 μL of diluted nanoparticle solutions (50% mixture in ethanol) was applied to a carbon-formvar coated copper grid (400 mesh, Ted Pella, Redding, CA or Electron Microscopy Sciences Hatfield, PA) and allowed to air dry. The resulting images were

analyzed using Image Pro Analyzer, and at least 100 nanoparticles were evaluated per sample.

5.2.3 UV-Visible (UV-Vis) Spectroscopy

Nanoparticle solutions were characterized using a UV-Vis spectrometer (USB 4000, Ocean Optics, Dunedin, FL) and a white light source. All measurements were collected using the following parameters: 10 millisecond integration time, 20 spectra averaging, and a Boxcar equal to 5. Extinction maxima were calculated from the zero point crossing value of the first derivative of the spectra using an in-house developed MathCAD program. Stock nanoparticle solutions were diluted using 5.5 mS cm^{-1} pH 7.3 sodium phosphate buffer.

5.2.4 Zeta Potential

Nanoparticles solutions were diluted to 1 nM in 5.5 mS cm^{-1} pH 7.3 sodium phosphate buffer prior to zeta potential measurements (Delsa Nano, Beckman-Coulter, Brea, CA). Zeta potential measurements were performed in triplicate using H_2O diluent parameters (refractive index (RI) = 1.3328, viscosity (η) = 0.8919 cP, and dielectric constant (ε) = 78.4) at 25° C. A flow cell configuration was used for all measurements, and data were fit using the Smoluchowski theory.

5.2.5 X-Ray Photoelectron Spectroscopy (XPS)

XPS measurements were collected using a Kratos Axis Ultra Spectrometer with a monochromatic Al K_α X-ray source as described previously.[136] Briefly, a 160 eV pass energy, 1 eV step size, 200 ms dwell time, and ~700 μm x 300 μm X-ray spot size were used for a survey scan (range = 1200 – -5 eV). Region scans (O 1s, C 1s, S 2p, and Au 4f) exhibited typical band widths of 20 - 50 eV, 20 eV pass energies, 0.1 eV step sizes, and 1000 msec dwell times.

All spectra were analyzed using CasaXPS and were charge-calibrated with respect to the adventitious C 1s peak at 285.0 eV. The S 2p peak of thioctic acid was deconvoluted using the S 2p doublet with a 2:1 area ratio and an energy difference of 1.2 eV. A Shirley background was used to subtract the inelastic background from the S 2p and Au 4f signals. The curves were fit using a Gaussian/Lorentzian (GL(30)) lineshape. To account for differences in nanoparticle concentration in sample spots, the S 2p areas were normalized using the Au 4f area. Measurements were performed in duplicate, and error bars represent the standard deviation of these data.

5.2.6 Buffer Preparation

A stock 250 mM phosphate buffer (16 mS cm^{-1}, pH 7.3) was prepared from phosphoric acid and sodium phosphate and pH adjusted with concentrated NaOH. A 5.5 mS cm^{-1} pH 7.3 separation buffer was prepared by diluting the 250 mM stock buffer solution. All buffers were 0.2 μm filtered and degassed prior to use.

5.2.7 Capillary Electrophoresis (CE)

All separations were performed using a Beckman Coulter P/ACE MDQ (Brea, CA) capillary electrophoresis (CE) instrument equipped with a UV light source and UV-Vis or PDA detector. UV detection occurred at 200 nm, and PDA detection occurred at both 520 nm and 600 nm. The capillary temperature was maintained at 25° C. The instrument was utilized per manufacturer recommendations. Fused silica capillary was purchased from Polymicro (Phoenix, AZ) with an internal diameter of 75 μm and an outer diameter of 360 μm. The total capillary length was 60.2 cm and a 50 cm effective path length.

The capillary was conditioned using the following procedure: 0.1 M HNO_3 (20 psi for 5 minutes), H_2O (20 psi for 2.25 minutes), 1 M NaOH (20 psi for 2.25 minutes), H_2O (20 psi for 2.25 minutes), 250 mM sodium phosphate buffer (20 psi for 3 minutes), and 30 mM separation solution either with or without nanoparticles (20 psi for 3

minutes). Separations were performed using normal polarity and a 20 kV separation voltage.

5.2.8 Data Analysis

All electropherograms were processed using an in-house designed Excel Macro application (Appendix A). Raw data were processed into time, absorbance, current and potential columns. Peak areas were fit using OriginPro 7.5 equipped with a peak fitting module. Specifically, a two point linear baseline fit was manually assigned for each peak in the electropherogram. After baseline subtraction, peaks were fit using either Gaussian or EMGaussian peak function for symmetric or asymmetric peaks, respectively. Reported peak areas are for the best fit peaks as determined by minimized chi-squared values. Averages and standard deviations for normalized migration times and peak areas were evaluated from at least 3 replicate separations and propagated errors, respectively.

5.3 Results and Discussion

5.3.1 Characterization of Carboxylic Acid Functionalized Gold Nanoparticles

Effective use of nanoparticle pseudostationary phases requires the incorporation of stable and homogenous nanoparticles.[253] Plasmonic nanomaterials (i.e. gold, silver, composites, etc.) exhibit a localized surface plasmon resonance (LSPR), a size dependent property which induces strong electric fields at the particle surface.[67, 68] The LSPR of noble metal nanoparticles is (1) experimentally measured using extinction spectroscopy (i.e. scattered and absorbed light);[70] (2) dependent on the distance matter is from the nanoparticle surface;[71] (3) theoretically predicted using Mie theory;[72] and (4) dictated by nanoparticle composition, shape, size, and local dielectric environment.[72-74]

The influence of surface chemistry on the LSPR of gold nanoparticles is demonstrated in Figure 5.1. Gold nanoparticles functionalized with thioctic acid, 6-

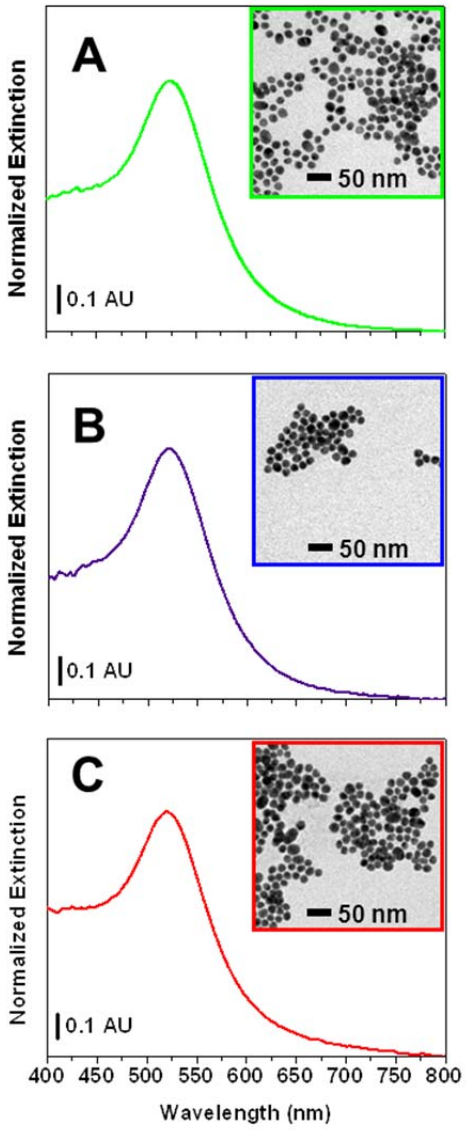

Figure 5.1 Extinction spectra and TEM inset of 1 nM (A) Au@MUA (λ_{max} = 524.7 nm), (B) Au@MHA (λ_{max} = 522.3 nm), and (C) Au@TA (λ_{max} = 521.5 nm) nanoparticles, respectively. All samples were suspended in 5.5 mS cm^{-1} buffer (pH = 7.3) prior to analysis.

mercaptohexanoic acid, and 11-mercaptoundecanoic acid display unique extinction spectra with characteristic extinction maxima wavelengths (λ_{max}) which range from 521.5, 522.3, and 524.7 nm, respectively. All three nanoparticle samples possess core sizes at or near 13 nm and are dispersed in the same bulk dielectric environment; therefore, differences in the λ_{max} are attributed to either SAM packing density and/or alkanethiol chain length variations.[72] For example, it is well-established that thioctic acid binds to the gold nanoparticle surface via a disulfide ring,[80, 81, 86] whereas 6-mercaptohexanoic acid and 11-mercaptoundecanoic acid bind via a single thiol bond.[199] The larger binding moiety of thioctic acid lowers its packing density vs. the other two ligands, and a slightly blue-shifted LSPR is observed.[189, 200] Furthermore, because the LSPR wavelength increases as alkanethiol chain length increases,[70] Au@MUA nanoparticles exhibit a lower energy extinction maximum than Au@MHA nanoparticles.

In addition to providing information regarding nanoparticle shape and size homogeneity, TEM data are coupled with a standard estimation model to calculate the concentration of gold nanoparticles.[89] To do this, a molar extinction coefficient (ε) is calculated using the average nanoparticle diameter. For these samples, an extinction coefficient at $\lambda = 450$ nm is estimated at $1.0_9 \times 10^9$ $M^{-1}cm^{-1}$.

5.3.2 Surface Charge Characterization of Au@MUA, Au@MHA, and Au@TA Nanoparticles

Nanoparticle surface properties are important for characterizing nanoparticle "structure" for functional use. Zeta potential, a direct measure of nanoparticle mobility and indirect measure of surface charge,[254] can be used to estimate nanoparticle stability. Prior investigations on carboxylic acid functionalized gold nanoparticles revealed negative zeta potential values ranging from 36 – 60 mV (pH 9).[106, 212] In these studies, functionalized gold nanoparticles were dispersed in pH 7.3, 5.5 mS cm^{-1} phosphate buffer and allowed to equilibrate for at least 1 hour. The zeta potential of carboxylic acid

functionalized Au nanoparticles is dependent on ligand pK_a, binding moiety, packing density, and surrounding dielectric environment. For example, the zeta potential from the Au@TA nanoparticles is -18.4 ± 1.3 mV which is not statistically different from Au@MHA nanoparticles (-20.9 ± 1.5 mV). In contrast, the zeta potential for Au@MUA nanoparticles is -37.6 ± 3.5 mV. This relatively greater surface charge density suggests that ligand density is greater than that for either Au@MHA or Au@TA nanoparticles.

5.3.3 XPS Characterization and Packing Density Estimations for Au@MUA, Au@MHA, and Au@TA Nanoparticles

To better understand the implications of the LSPR and zeta potential measurements, XPS is used to gain quantitative packing densities for SAMs on gold nanoparticles. To achieve this, the S 2p doublet signal was monitored (Figure 5.2A-C). These S 2p signals are corrected to the Au 4f peak area to reduce any interference caused by evaluating slightly different sample areas and nanoparticle coverages. XPS data were quantified according to a previously established procedure.[81] First, the shell method[69] and empirical atomic sensitivity factors[152] were used to correct the XPS signals. It should be noted that (1) the core size of Au nanoparticles functionalized with MUA, MHA, and TA are not statistically different and (2) the surface of 12.7 ± 1.1 nm gold nanoparticles contain predominately (100) surface planes. As a result, the packing density of carboxylic acid terminated SAMs on gold nanoparticles can be approximated from XPS spectra as follows:

$$\text{Packing density} = \left[\frac{S}{Au_{surface}}\right]\left[\frac{Ligand}{S}\right]\left[\sigma_{100}\right] \qquad (5.1)$$

where the first term is the corrected $S/Au_{surface}$ XPS signal, the second term is the ligand to sulfur ratio (1,1, and 0.5 for MUA, MHA, and TA, respectively), and the third term is the gold atom packing density for a (100) surface plane (12.03 atoms nm^{-2}).

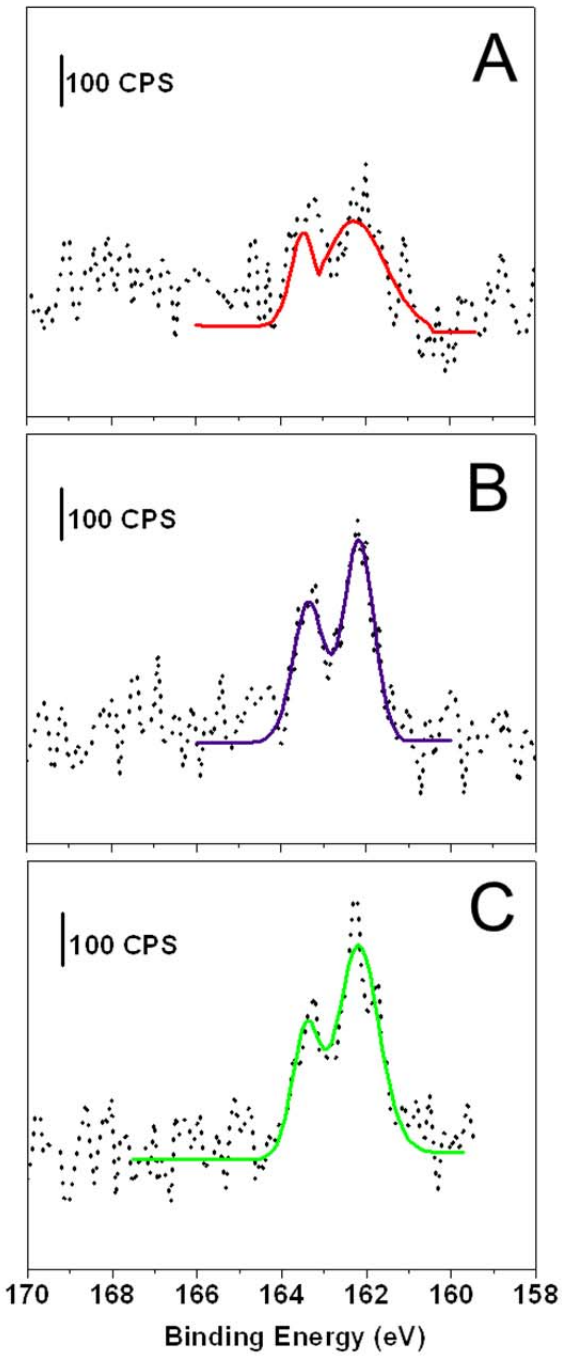

Figure 5.2 XPS characterization of Au@TA, Au@MHA, and Au@MUA nanoparticles. Normalized XPS spectra (S 2p) for (A) Au@TA, (B) Au@MHA, and (C) Au@MUA nanoparticles where the solid and dashed lines correspond to the fitted and raw data, respectively. A S 2p doublet with binding energies of 161 and 163.2 eV are predominate for all three nanoparticle species.

Table 5.1 summarizes the corrected XPS signals and estimated SAM packing densities for Au@TA, Au@MHA, and Au@MUA nanoparticles. These data demonstrate that SAM packing density on Au@MUA nanoparticles is ~5.3% and ~16% greater than Au@MHA and Au@TA nanoparticles, respectively. While zeta potential reveals similarities between Au@TA and Au@MHA nanoparticles, this more quantitative technique provides more detailed information about SAM packing density.

Table 5.1 S/Au $_{surface}$ Atomic Ratio and Estimated SAM Packing Density from XPS Data for Au@TA, Au@MHA, and Au@MUA Nanoparticles.

	S/Au$_{surface}$ Ratio	**Packing Density x 10^{14} (molecules/cm^2)**
Au@TA	$0.83_9 \pm 0.01_5$	$2.20_0 \pm 0.03_9$
Au@MHA	$0.89_2 \pm 0.02_7$	$4.58_1 \pm 0.01_9$
Au@MUA	$0.96_3 \pm 0.02_9$	$4.97_5 \pm 0.01_8$

5.3.4 Evaluation of Functionalized Au Nanoparticle Stability in CE

To assess their usefulness as continuous full filling pseudostationary phases in CE, unique LSPR properties of gold nanoparticles are exploited. Importantly, the large (~1.0 x 10^9 M^{-1} cm^{-1}) extinction coefficient of gold nanoparticles facilitate trace detection in a capillary. Previously, we monitored the plasmon bands during a CE separation at λ = 520 and 600 nm using a dual wavelength PDA detector.[106] Herein, functionalized gold nanoparticle stability is assessed by injecting a small (2% total capillary volume) 1 nM Au@MUA (Figure 5.3A), Au@MHA (Figure 5.3B), or Au@TA (Figure 5.3C) nanoparticle plug into a capillary and monitoring the plasmonic properties of the nanoparticles at λ = 520 and 600 nm during electrophoresis.

Several trends are noted in these electropherograms. First, a single band is observed at λ = 520 nm for all three nanoparticle functionalities. Second, a less intense

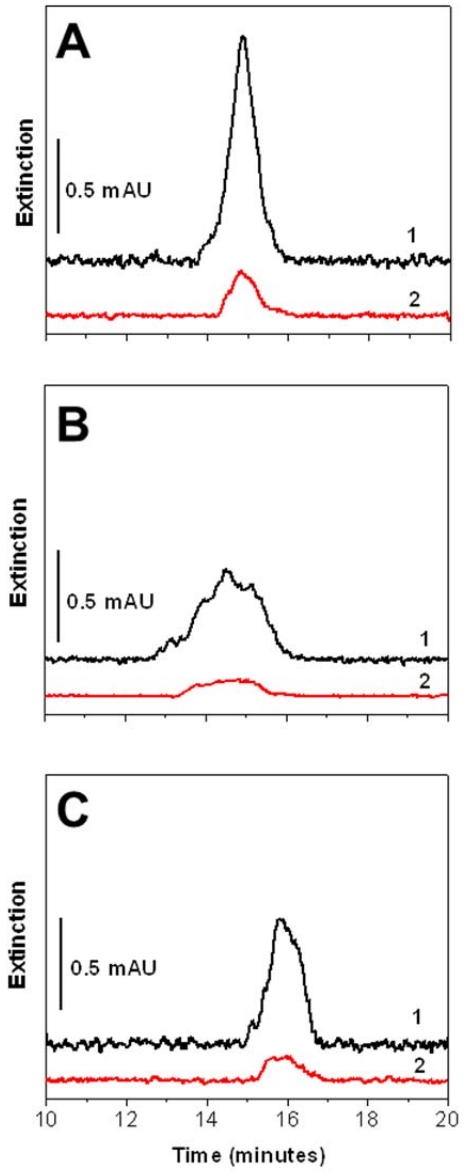

Figure 5.3 Representative electropherograms from dual-wavelength detection of 1 nM (A) Au@MUA, (B) Au@MHA, and (C) Au@TA nanoparticles in the capillary collected at (1) 520 nm and (2) 600 nm. Separations performed at 20 kV using 30 mM sodium phosphate (pH = 7.3, 5.5 mS cm^{-1}) buffer, and nanoparticles occupy ~2 % of the total capillary volume.

band with a similar migration time (as the band collected at 520 nm) is observed at λ = 600 nm. Band area ratios for the three nanoparticle functionalities are 5.43, 5.24, and 4.66 for Au@MUA, Au@MHA, and Au@TA nanoparticles, respectively. These values are similar to macro LSPR spectral intensities and indicate 1 nM carboxylic acid functionalized Au nanoparticle plugs exposed to a 333 V/cm electric field (in these separation conditions) behave as electromagnetically stable nanostructures (i.e. do not undergo uncontrolled aggregation). Au@MUA nanoparticles however, exhibit the greatest ratio and therefore are the most stable of the carboxylic acid functionalized gold nanoparticles studied.

Despite these similarities, significant differences are noted in band migration times, peak areas/intensities, and peak full width at half maximum (FWHM) values. First, the average migration time of nanoparticle bands at 520 nm and 600 nm range from 14.5_5, 14.7_1, to 15.8_7 minutes for Au@MUA, Au@MHA, and Au@TA nanoparticles, respectively. These differences are attributed to varying hydrated radii (largest and smallest hydrated radii for Au@TA and Au@MUA nanoparticles, respectively). Second, despite injecting equal concentrations of all three functionalized nanoparticles, differences in peak area and intensity are clearly noted in Figure 5.3. For Au@MUA nanoparticles, peak areas are ~1.5 times more intense than that for either Au@MHA or Au@TA nanoparticles. Au@MUA nanoparticles are relatively more negative (-37.6 mV) in these buffer conditions, a value that likely arises from a higher density of MUA molecules (4.97×10^{14} molecules/cm^2) as compared to the other two ligands. We attribute the similarity in peak areas for Au@MHA and Au@TA nanoparticles to similarities in the observed zeta potential values (-18.4 and -20.9 mV, respectively). As a result, Au@MUA nanoparticles are hypothesized to be less likely to flocculate and interact with the negatively charged capillary wall thereby exhibiting larger peak areas than either Au@MHA or Au@TA nanoparticles.

Finally, the FWHM of nanoparticle peaks differ significantly among the three functionalized nanoparticle samples (Figure 5.3A-C). Nanoparticle peak FWHM values collected at 520 nm are 56, 100, and 65 seconds for Au@MUA, Au@MHA, and Au@TA nanoparticles, respectively. We hypothesize these differences are related to SAM packing density variations among the three nanoparticle samples.

5.3.5 Electrical Affects of Carboxylic Acid Functionalized Au Nanoparticles Continuous Full Fill Pseudostationary Phases in CE

Clearly, nanoparticle pseudostationary phases exhibit surface chemistry dependent interactions during capillary-based separations.[103] Because CE separations are sensitive to subtle changes in buffer composition and pH, experiments were performed to assess how the observed DC current changes in the presence and absence of functionalized gold nanoparticles. Both nanoparticle concentration and SAM functionality were evaluated. In all cases, the capillary was filled with either 1 or 5 nM concentrations of Au@MUA, Au@MHA, or Au@TA nanoparticles prior to applying a 333 V/cm electric field. Currents were monitored as a function of time and compared to similar assays performed without gold nanoparticles. Figure 5.4 presents the change in current (collected at 1 minute after the potential was applied) as a result of the functionalized gold nanoparticles at both 1 and 5 nM concentrations. In all cases, the gold nanoparticle pseudostationary phase influence current variations in a surface chemistry dependent manner. For instance, 1 nM Au@MUA nanoparticles suppress current. These differences decreased when Au@MUA nanoparticle concentration increased. For both Au@MHA and Au@TA nanoparticles, current is enhanced relative to controls. Less systematic responses were observed at higher nanoparticle concentrations.

The electrical behavior of carboxylic acid functionalized gold nanoparticles reveals several interesting trends. First, gold nanoparticle surface chemistry impacts the

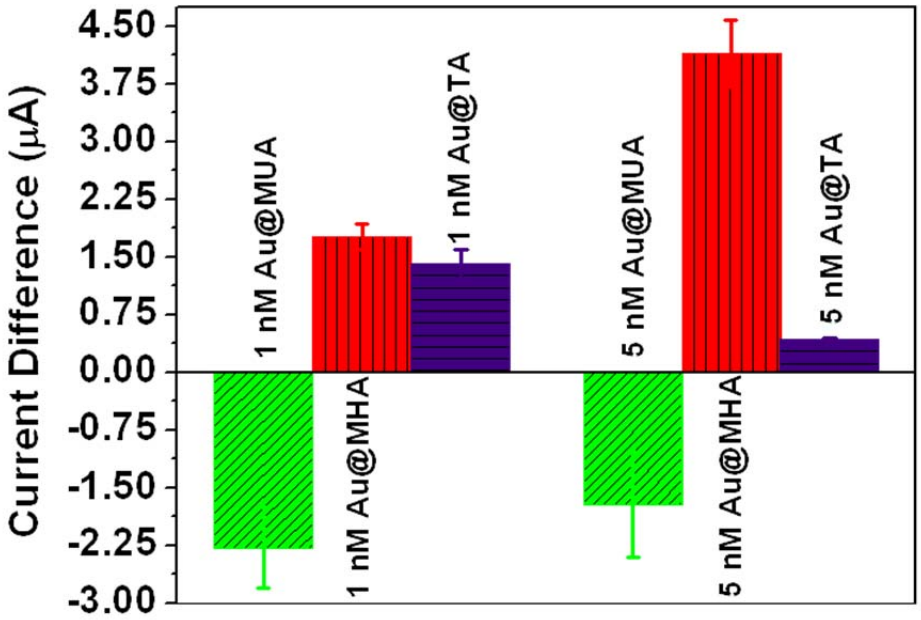

Figure 5.4 Current differences as a result of gold nanoparticle pseudostationary phases. At both 1 and 5 nM, Au@MUA nanoparticles (diagonal stripes) suppress current relative to controls. Conversely, Au@MHA (horizontal stripes) and Au@TA (vertical stripes) nanoparticles enhance current. Increasing concentrations of Au@TA produce greater current enhancement, while these effects are diminished with increasing concentrations of Au@MHA nanoparticles.

current response at all concentrations studied. To model the interactions between particles within the capillary, Derjagvin-Landau-Verwey-Overbeek (DLVO) theory is used.[87] Classical DLVO theory uses van der Waals (V_{vdW}, Equation 5.2) and electrostatic interactions (V_{elec}, Equation 5.3) to explain nanoparticle interactions and stability as follows:[88]

$$V_{vdW} = -\frac{A}{6}k_B T\left[\frac{2R^2}{d^2-4R^2}+\frac{2R^2}{d^2}+\ln\left(\frac{d^2-4R^2}{d^2}\right)\right] \tag{5.2}$$

$$V_{elec} = 2\pi\varepsilon_r\varepsilon_0\psi_0^2 R k_B T \ln\left[1+\exp(-kd)\right] \tag{5.3}$$

$$\text{where } k = \frac{1000e^{2}N_A(2I)}{\varepsilon_R\varepsilon_O k_B T},$$

A is the Hamaker constant, k_B is the Boltzman constant, T is the temperature, R is the radius of the particles, d is the separation distance between particles, ε_r is the relative dielectric constant of the liquid, ε_o is the permittivity of the vacuum, ψ_o is the zeta potential of the particles, k is the inverse Debye length, e is the elementary charge, N_A is Avagadro's number, and I is the ionic strength of the solution.

Classical DLVO theory (Figure 5.5A) models particles as infinitely flat solid surfaces with uniform surface charge densities. Furthermore, surface potential (i.e. zeta potential) is assumed to be constant and uniform and that no chemical reactions occur between the solvent and the particles (i.e. solvent influences the solution dielectric constant only). Despite these assumptions, classic DLVO is widely accepted as a plausible model to estimate total interactions (V_{total}) between two electrostatically stabilized particles in solution as follows:

$$V_{total} = V_{vdW} + V_{elec} \tag{5.4}$$

However, to apply DLVO theory to the functionalized nanoparticles evaluated in these studies, extended DLVO theory (Figure 5.5B) must be used.[255] First, localized increases

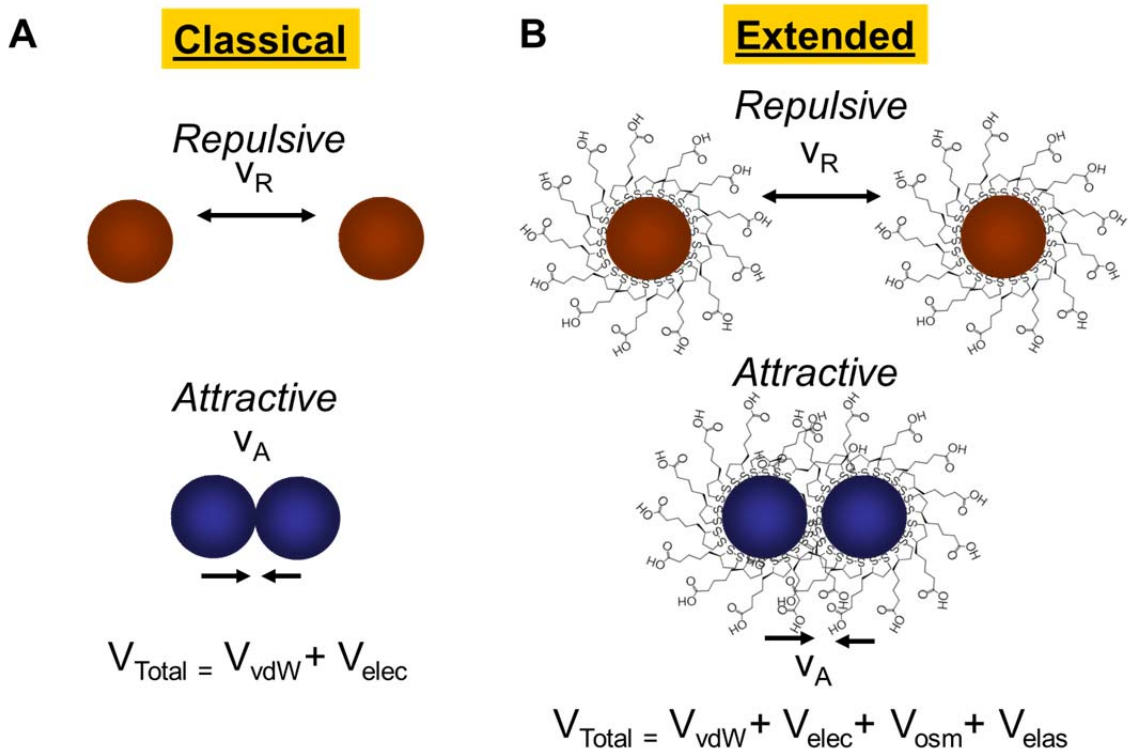

Figure 5.5 Representation of interparticle interactions between two nanoparticles via (A) classical and (B) extended DLVO theory. Both models describe the total interaction action potential energy between two particles as a function of separation distance. Drawings are not to scale.

in osmotic pressure (V_{osm}) near the surfaces between two adjacent particles is calculated.[256] This term contributes to the repulsive force between particles and is significant if the total separation distance between particles is less than the particle diameter and is calculated as follows:

$$V_{osm} = 0 \qquad 2w \le d$$

$$V_{osm} = \frac{4\pi R k_B T}{\upsilon_1}\phi^2\left(\frac{1}{2}-\chi\right)\left(w-\frac{d}{2}\right) \qquad w \le d \le 2w \tag{5.5}$$

$$V_{osm} = \frac{4\pi R k_B T}{\upsilon_1}\phi^2\left(\frac{1}{2}-\chi\right)w^2\left(\frac{d}{2w}-\frac{1}{4}-\ln\left(\frac{d}{w}\right)\right) \qquad w \le d$$

where υ_1 is the molecular volume of the solvent, Φ is the volume fraction of the coating layer, χ is the Flory-Huggins interaction parameter, R is the particle radius, and w is the thickness of the SAM layer. The surface ligands are assumed undistorted until the interparticle distance (d) equals the SAM length (w).

Extended DLVO theory also includes an interaction parameter which considers elastic repulsion as a result of SAM compression on the particle surface (V_{elas}). Analogous to V_{elas}, the elastic repulsive force (Equation 5.6) is only significant when the inter-particle distance (d) is less than the coating layer thickness (w)

$$V_{elas} = 0 \qquad w \le d \tag{5.6}$$

$$V_{elas} = \frac{2\pi R k_B T}{M_w} w^2 \phi^2 \rho^2 \left(\frac{d}{w}\ln\left(\frac{d}{w}\left(\frac{3-d/w}{2}\right)^2\right) - 6 * \ln\left(\frac{3-d/w}{2}\right) + 3\left(1+\frac{d}{w}\right)\right) \quad w \ge d$$

where M_w is the molecular weight of the particle coating molecule and ρ is its density.

Finally, the total interactions (V_{total}) between coated particles are as follows:[257, 258]

$$V_{total} = V_{vdW} + V_{elec} + V_{osm} + V_{elas} \tag{5.7}$$

Using this model, the total interactions between two Au nanoparticles functionalized with 11-mercaptoundecanoic acid, 6-mercaptohexanoic acid, and thioctic acid are presented in

Figure 5.6 as a function of separation distance. For all three nanoparticle samples, the following parameters were used: A = 0.997 eV, particle radius R = 6.5 nm, dielectric constant of water = 80.1, and a solution ionic strength = 30 mM. To calculate the osmotic and elastic interactions, important individual steric effects for each SAM were considered and are summarized in Table 5.2.

Table 5.2 Osmotic and Elastic Interaction Parameters for Au@MUA, Au@MHA, and Au@TA Nanoparticles using Extended DLVO theory.

Nanoparticle	**ζ potential (mV)**	***Φ***	**ρ (g nm^{-3}) x 10 $^{-21}$**	**Mw (g mol^{-1})**	**ω (nm)**
Au@MUA	-37.6	0.775	1.65	218.36	0.95
Au@MHA	-20.9	0.483	1.03	148.22	0.52
Au@TA	-18.4	0.388	0.69	206.3	0.49

These extended DLVO theory calculations for Au@MUA, Au@MHA, and Au@TA nanoparticles show both distinct surface chemistry dependent similarities and differences. First, all three nanoparticle species demonstrate a large buildup of osmotic repulsive pressures when the interparticle distance (*d*) is less than the coating layer thickness (*w*) where as the chemisorbed surface ligands are being compressed. Likewise, the elastic repulsion, although small, exhibits a discrete energy barrier positioned at the edge of the SAM layer. These elastic repulsions diminish as the interparticle distance decreases which restricts the steric rotation of surface ligands and as a result, reduces entropy. The electrostatic repulsive interactions are small but positive for Au@MUA, Au@MHA, and Au@TA nanoparticles and are consistent with negative zeta potential values. Finally, the van der Waals attractive forces for all three functionalized nanoparticles are the same as the Hamaker constant for all samples are equal.

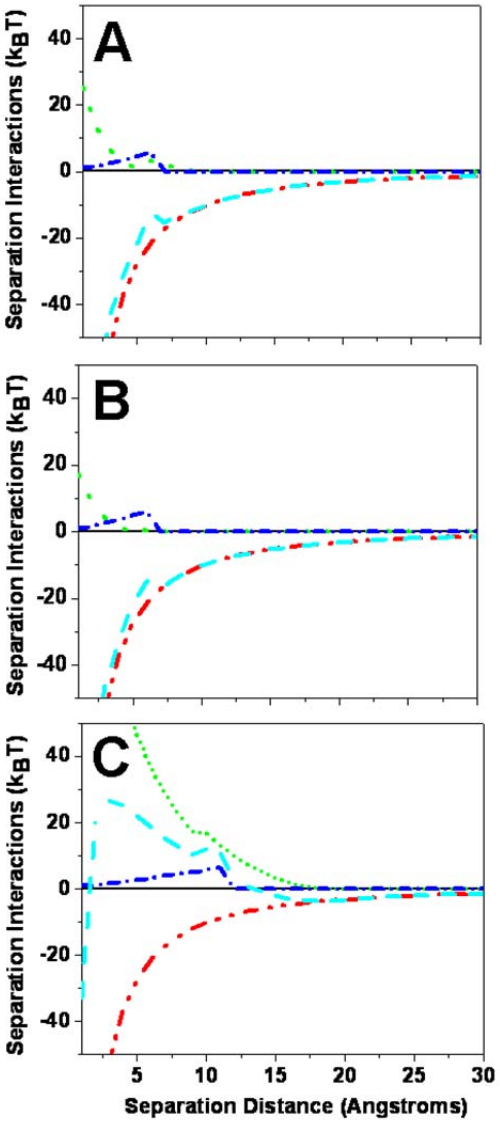

Figure 5.6 Extended DLVO theory calculation for (V_{elec}), ($V_{vdW,}$), osmotic (V_{osm}), elastic (V_{ela}), and total interparticle interactions (V_{total}) of interactions for (A) Au@MHA, (B) Au@TA, and (C) Au@MUA nanoparticles in pH 7.3, 5.5 mS cm^{-1} phosphate buffer.

While this model only estimates nanoparticle stability, subtle differences in total interactions can be related to the in-capillary nanoparticle behavior. First, while both Au@MHA and Au@TA nanoparticles will aggregate at separation distances greater than 2*w,* Au@MUA nanoparticles total exhibit repulsive total interactions until $d \sim 0.2$ nm. Furthermore, Au@MUA nanoparticles display a secondary minimum ~1.5 to 1.7 nm from the metal surface. This secondary energy minimum suggests that Au@MUA nanoparticles flocculate rather than irreversibly aggregate as indicated by the Au@MHA and Au@TA nanoparticle models. Finally, the increased packing density for Au@MUA versus Au@MHA or Au@TA nanoparticles produces larger elastic and osmotic repulsive forces, thereby facilitating aggregation only when interparticle separations approach the length of the 11-MUA monolayer (~1 nm). These extended DLVO calculations support that Au@MHA and Au@TA nanoparticles are much more likely to aggregate than Au@MUA nanoparticles. For both Au@MHA and Au@TA nanoparticles, the Brownian motion energy barrier (3/2 k_BT) is easily overcome at separation distances less than 3 nm.

Clearly, implications of surface chemistry on the aggregation behavior of these carboxylic acid functionalized gold nanoparticles is revealed through this model and can be used to explain current variations observed during continuous full filling CE experiments. Because the capillary can be modeled as a simple circuit, electrical behavior can be described using Ohm's law:

$$V = iR \tag{5.8}$$

where V is the applied potential, i is the measured current, and R is the resistance. Because all experiments both with and without gold nanoparticles were performed using a constant potential (20 kV), all current variations must be a direct result of resistance changes induced by gold nanoparticles and occur in a surface chemistry dependent manner.

To reconcile the experimental trends, the nanoparticle surface is modeled as a modified electrode submerged in a background electrolyte. Electron transfer processes for these systems are well defined for many different types of layers including those doped with electroactive species[259] and "blocking" layers.[260] Blocking layers are materials on the electrode surface which interrupt electron and ion transport between the electrode and solution and can either diminish or eliminate measured current responses for these electrodes in a surface coverage dependent fashion. If the films on these electrodes are sufficiently thin (i.e. < 1.5 nm),[261] electrons can tunnel through the blocking layer and generate increased currents.[262]

This same model is applied to Au@MUA, Au@MHA, and Au@TA nanoparticles. The probability of electron tunneling is proportional to the distance over which the electron must tunnel and the tunneling factor, β. The magnitude of the tunneling factor depends on the energy barrier of the bulk medium. The distance any electron can travel via tunneling is described in Equation 5.9:

$$k_{e^-}(x) = k_{e^-}{}^{0} \exp^{-\beta x} \qquad (5.9)$$

where $k_{e^-}(x)$ is the distance between interaction surfaces and $k_{e^-}{}^{0}$ is the transmission coefficient. For functionalized gold nanoparticle surfaces, typical tunneling distances (x) approach ~0.1 nm^{-1}.[261] Recall that both Au@MHA and Au@TA nanoparticles should aggregate when interparticle separation distances are less than 3 nm, according to the extended DLVO model. As nanoparticles aggregate, their separation distances approach zero and likely facilitate electron tunneling between particles. Conversely, Au@MUA nanoparticles are very stable or reversibly flocculated to interparticle distances of 1.5 nm at a secondary energy minimum. Because this process is reversible (from the repulsive energy rise at shorter distances), the probability that two Au@MUA nanoparticles become close enough to facilitate particle to particle tunneling is minimized.

This theory is consistent with the experimental data shown in Figure 5.4 which demonstrates that Au@MHA and Au@TA nanoparticles enhance currents. These effects are concentration dependent where 1 nM Au@TA nanoparticle solutions increase the current by 1.7_6 mA, and 5 nM Au@TA nanoparticle concentrations increase the current by 4.1_4 mA vs. controls. Recently, the concentration dependent behavior of carboxylic acid functionalized gold nanoparticles in electrically driven flow was thoroughly investigated.[106] In these studies, the critical nanoparticle concentration (CNC), a parameter similar to the critical micelle concentration in micellar electrokinetic chromatography (MEKC), was defined as the lowest concentration of nanoparticles that induces dominant nanoparticle aggregation (versus stable nanoparticles) under specific buffer conditions. Experimentally, the CNC for carboxylic acid functionalized gold nanoparticle is ~1.8 nM, well below the 5 nM concentration of Au@TA nanoparticles evaluated here. As a result, Au@TA nanoparticles should readily aggregate thereby facilitating greater electron tunneling probabilities and current enhancement effects.

Similar trends are observed for Au@MHA nanoparticles. First, when a 1 nM Au@MHA nanoparticle concentration is added to the buffer, the current is enhanced by 1.4_1 μA, indicating Au@MHA nanoparticle aggregation leads to electron tunneling. Second, the current is enhanced by 0.4_3 mA when a 5 nM Au@MHA nanoparticle concentration is included in the buffer. These differences can be attributed to the increased likelihood of aggregation for Au@MHA from either packing density or chain length differences.

The current responses for Au@MUA nanoparticle pseudostationary phases are also concentration dependent but exhibit opposite effects vs. both Au@MHA and Au@TA nanoparticles. First, when present in the capillary, Au@MUA nanoparticles neither aggregate nor facilitate electron tunneling. Furthermore, at 1 and 5 nM concentrations, current suppression is observed at -2.2_8 μA and -1.7_2 μA, respectively. This is consistent with the size dependent electrical properties of isolated gold

nanoparticles.[40] Although more stable than either of the other two nanoparticle species studied, a 5 nM Au@MUA nanoparticle concentration is still well above the CNC for carboxylic acid functionalized gold nanoparticles, and the diminished responses are attributed to combined internanoparticle separation distances and electron tunneling effects.

5.4 Conclusions

The effects of continuous full filling Au@MUA, Au@MHA, and Au@TA nanoparticle pseudostationary phases on observed separation currents during capillary electrophoresis were evaluated. Au@MUA nanoparticles suppressed while both Au@MHA and Au@TA nanoparticles enhanced the current. Extended DLVO theory was used to model interparticle interactions in the capillary for the three carboxylic acid functionalized nanoparticle samples. Modeled inter-nanoparticle interactions revealed that Au@MHA and Au@TA nanoparticles were all more likely to undergo uncontrolled aggregation at small separation distances which facilitated electron tunneling and increased currents. Opposite trends were observed for Au@MUA nanoparticles whereby a secondary energy minimum at a ~1.5 nm internanoparticle separation distance promoted reversible nanoparticle flocculation and reduced the probability of electron tunneling. All effects depended on nanoparticle concentration until the CNC was exceeded and irreproducible effects were observed.

These studies represent the first investigations of how nanoparticle surface chemistry can impact capillary circuitry during nanoparticle-containing pseudostationary phase experiments. The high degree of synthetic control and subsequent characterization of Au@MUA, Au@MHA, and Au@TA nanoparticles facilitated these findings. Further inverstigations of nanoparticle function will improve the integration of nanomaterial pseudostationary and stationary phases in CE separations for various applications.

CHAPTER 6
INVESTIGATION OF GOLD NANOPARTICLE FUNCTIONALIZATION ON THE SEPARATION OF SUSPECTED PARKINSON'S DISEASE BIOMARKERS

6.1 Introduction

Currently, Parkinson's disease (PD) is the second most common neurodegenerative disease in the U.S. and affects ~1 million patients.[242] Typically, diagnosis occurs between the ages of 50 and 70 with a slow disease progression over 10 to 20 years. The exact pathology of PD is unknown, but loss of motor function is attributed to the progressive loss of dopaminergic neurons in the substantia nigra pars compacta region of the brain.[263] Currently, there are no definitive biomarkers to produce an objective test to diagnosis PD. Instead, because physicians rely on a patient's medical history and positive response to medications, there is a relatively high rate of PD misdiagnosis.[244]

Although no definitive biomarkers exist, approximately half a dozen molecules are linked to PD.[264, 265] Dopamine (DA), a catecholamine neurotransmitter associated with control of motor neurons in the brain, is the most widely studied biomarker. In fact, motor neuron death caused by the unregulated oxidation of dopamine to melanin is hypothesized as a possible cause of PD.[266-268] Epinephrine (EP) is another catecholamine neurotransmitter linked to PD. Dopamine and epinephrine are structurally similar catalytic products of tyrosine. Because both molecules are found within the central nervous system, PD patient sample extraction is difficult. Fortunately, unlike these two neurotransmitters, uric acid (UA) is found in the blood at abnormally high levels in Parkinson's patients[244, 245] and may be a more accessible biomarker for PD diagnosis.

Detecting biomarkers in PD patient samples requires the ability to (1) use small sample volumes and (2) separate biological samples in complex matrices. Capillary

electrophoresis (CE) is well suited for these tasks. First, CE provides high separation efficiencies (1.0×10^6 plates m^{-1}),[269] requires small sample volumes (nanoliter),[8] and is compatible with aqueous solutions.[9] Ionic molecules are easily separated using CE; however, neutral analytes are poorly resolved (i.e. no electrophoretic mobility). To separate neutral species, both pseudostationary (i.e. matrices which can either co-migrate with or migrate against the mobile phase) and stationary phases (i.e. non-moving matrices) are implemented to improve separation selectivity.[11]

Nanoparticles were previously used to improve CE separations of potential PD biomarkers[106] because they possess ideal properties for integration into CE as pseudostationary and stationary phases.[5] For instance, these materials are inherently "small" - that is, exhibit at least one dimension less than 100 nm. Furthermore, nanomaterials can be included at low concentrations compared to traditional CE pseudostationary or stationary phases so that less than 1% of the total capillary volume is occupied by nanoparticles.[26] Similarly, nanomaterials exhibit inherently large surface area to volume ratios and novel size dependent chemical and physical properties.[27, 28] Finally, the high degree of synthetic control of nanomaterial core composition and surface chemistry can be used to produce a plethora of nanomaterials for use in CE.[121, 270, 271]

Nanomaterials were first used in CE separations over twenty years ago. In 1989, Wallingford demonstrated that a pseudostationary phase containing 20 nm (diameter) sulfonated polymer nanoparticles improved the separation of five catecholamines.[29] Although resolution in these experiments was poor, the usefulness of nanomaterials in separations and the importance of nanomaterial surface chemistry were clearly demonstrated. Recent advances in nanomaterials and CE were summarized in several reviews and included: (1) separation effects of nanoparticle pseudostationary phases;[30, 31] (2) general uses of nanomaterials;[32] (3) extension and modification of micellar electrokinetic chromatography mathematics to nanoparticle pseudostationary and

stationary phases;[33] (4) exploitation of nanomaterials for electrochemical detection;[34] (5) electrophoretic separations of nanoparticles;[35] and (6) nanoparticle surface chemistry effects.[253]

Separations of biological samples in the presence of nanoparticle pseudostationary phases will require a clear understanding of nanoparticle-analyte interactions. As a result, this chapter includes an investigation of how nanoparticle surface chemistry as well as analyte and nanoparticle concentrations influence the CE separation of dopamine, epinephrine, and uric acid ($pK_a = 8.8_7$, 8.5_5, and $10.3_{0,}$ respectively). Spherical gold nanoparticles (diameter, d = 12.4 ± 1.3) functionalized with 11-mercaptoundecanoic acid (solution pK_a = 4.6- 5.0),[211] 6-mercaptohexanoic acid (solution pK_a = 4.8),[207] and thioctic acid (solution pK_a = 4.75-5.3)[208] will be used as CE pseudostationary phases. These separations will be performed using 5.5 mS cm^{-1} pH 7.3 phosphate buffer which contains Au nanoparticles. Notably, these novel investigations reveal the role of surface chemistry on the usefulness and impact of gold nanoparticles during continuous full filling assays. First, nanoparticle stability in the capillary improves with increased ligand packing density. Second, increased nanoparticle concentration systematically impacts PD biomarker peak areas and migration times. These effects diminish as either nanoparticles aggregate within the capillary or with increased concentrations of PD biomarkers. Finally, electrostatic interactions between the carboxylic acid functionalized gold nanoparticles and PD biomarkers can be used to determine experimental half dose response values. These finding will help to efficiently implement nanomaterials in continuous full filling integration modes for separation-based assays.

6.2 Experimental

6.2.1 Carboxylic Acid Functionalized Gold Nanoparticle Synthesis

Citrate stabilized nanoparticles were synthesized using an established procedure.[106] All glassware was cleaned with aqua regia and rinsed prior to nanoparticle synthesis. Unless otherwise stated, all chemicals were purchased from Sigma Aldrich (St. Louis, MO). First, 20 mg of $HAuCl_4$ was dissolved in 50 mL 18.2 MΩ cm^{-1} Nanopure water (Barnstead International, Dubuque, IA) and brought to a rolling boil while stirring using a reflux condenser. Trisodium citrate (60 mg) was dissolved in Nanopure water (5 mL) and added to the boiling solution. Initially, the solution turned very dark violet and quickly changed to burgundy. The solution was refluxed for an additional 15-20 minutes. After cooling, the resulting nanoparticle solution was stored in a brown bottle.

Nanoparticle solutions were filtered through 13 mm diameter, 0.45 μm nylon filters (Whatman, Middlesex, UK) prior to use. Citrate stabilized gold (Au@citrate) nanoparticles were functionalized with various carboxylic acid ligands to form 6-mercaptohexanoic acid (Au@MHA), thioctic acid (Au@TA), or 11-mercaptoundecanoic acid (Au@MUA) self-assembled monolayers (SAMs). First, 1 mL of 10 mM ligand (MHA, TA, or MUA) was dissolved in ethanol and added to 10 mL of a 10 nM Au@citrate nanoparticle solution. This solution was stirred at 500 RPM for at least 60 hours at room temperature. The nanoparticles were then centrifuged at 11,500 RPM (8,797 x g) for 40 minutes, and the supernatant was replaced with pH adjusted water (pH = 11 with 1 M NaOH). The rinsing procedure was repeated three times to ensure sufficient removal of unbound ligand. The nanoparticles were stored in a brown vial until use.

6.2.2 Transmission Electron Microscopy (TEM)

Nanoparticle homogeneity was characterized by TEM using a JEOL JEM-1230. In all cases, 2 μL of diluted nanoparticle solutions (50% mixture in ethanol) was applied to a carbon-formvar coated copper grid (400 mesh, Ted Pella, Redding, CA or Electron Microscopy Sciences Hatfield, PA) and allowed to air dry. The resulting images were analyzed using Image Pro Analyzer, and at least 100 nanoparticles were evaluated per sample.

6.2.3 UV-Visible (UV-Vis) Spectroscopy

Nanoparticle solutions were characterized using an UV-Vis spectrometer (USB 4000, Ocean Optics, Dunedin, FL) and white light source. All measurements were taken using the following parameters: 10 millisecond integration time, 20 spectra averaging, and a boxcar of 5. Stock solutions were diluted using 5.5 mS cm^{-1} pH 7.3 sodium phosphate buffer. Extinction maxima were calculated from the zero point crossing value of the first derivative of the spectra using an in-house developed MathCAD program.

6.2.4 Zeta Potential Measurements

Surface charge was estimated using 1 nM nanoparticle solutions diluted in 5.5 mS cm^{-1} pH 7.3 sodium phosphate buffer. Zeta potential measurements (Delsa Nano, Beckman-Coulter, Brea, CA) were performed in triplicate using H_2O diluent parameters (refractive index (RI) = 1.3328, viscosity (η) = 0.8919 cP, and dielectric constant (ε) = 78.4) at 25° C. A flow cell configuration was used for all measurements and data was fit using the Smoluchowski theory.

Zeta potential measurements for nanoparticle-dopamine interactions were measured using 1 nM nanoparticle solutions in 5.5 mS cm^{-1} pH 7.3 sodium phosphate buffer. Nanoparticle to dopamine mole ratios of 1:0, 1:25,000, 1:125,000, 1:2,500,000 and 1:5,000,000 were allowed to incubate for 1 hour prior to zeta potential measurements. (Zeta Sizer, Malvern, Worcestershire, UK). Zeta potential measurements

were performed in triplicate using H_2O diluent parameters (RI = 1.3328, η = 0.8919 cP, and ε = 78.4) at 25° C. Zeta potentials were obtained from monomodal acquisitions and fit using the Smoluchowski theory. For easier comparison, the zeta potential data for all nanoparticle to dopamine mole ratios were normalized and referenced to values measured in the absence of dopamine.

6.2.6 X-ray Photoelectron Spectroscopy (XPS)

XPS measurements were collected using a Kratos Axis Ultra Spectrometer with a monochromatic Al K_α X-ray source as described previously.[136] Briefly, a 160 eV pass energy, 1 eV step size, 200 ms dwell time, and ~700 μm x 300 μm X-ray spot size were used for a survey scan (range = 1200 – -5 eV). Region scans (O 1s, C 1s, S 2p, Au 4f) exhibited typical band widths of 20 - 50 eV, 20 eV pass energies, 0.1 eV step sizes, and 1000 msec dwell times.

All spectra were analyzed using CasaXPS and were charge-calibrated with respect to the adventitious C 1s peak at 285.0 eV. The S 2p peak of MUA, MHA, and TA were deconvoluted using the S 2p doublet with a 2:1 area ratio and an energy difference of 1.2 eV. A Shirley background was used to subtract the inelastic background from the S 2p and the Au 4f signals. The curves were fit using a Gaussian/Lorentzian (GL(30)) lineshape. To account for differences in nanoparticle concentration in sample spots, the S 2p areas were normalized using the Au 4f area. Measurements were performed in duplicate, and error bars represent the standard deviation of these data.

6.2.7 Buffer, Biomarker, and Nanoparticle Solution Preparation

A stock 250 mM phosphate buffer (~16 mS cm^{-1}, pH 7.3) was prepared from phosphoric acid and sodium phosphate and pH adjusted with concentrated NaOH. A 5.5 mS cm^{-1} pH 7.3 separation buffer was prepared by diluting the 250 mM stock buffer. All

buffers were filtered (0.2 μm filters, Whatman, Middlesex, UK) and degassed prior to use.

Stock (5 mM) solutions of dopamine and epinephrine were prepared in 10 mM HCl. A 5 mM uric acid solution was prepared in 10 mM NaOH. To prepare sample aliquots, all three biomarker stock solutions were mixed and diluted in 10 mM HCl. Sample 1 contained 1.56 μM dopamine, 1.56 μM epinephrine, and 0.78 μM uric acid. Sample 2 contained 3.25 μM dopamine, 3.25 μM epinephrine, and 1.56 μM uric acid. Sample 3 contained 6.25 μM dopamine, 6.25 μM epinephrine, and 3.25 μM uric acid. Sample 4 contained 9.375 μM dopamine, 9.375 μM epinephrine, and 6.25 μM uric acid. Sample 5 contained 12.5 μM dopamine, 12.5 μM epinephrine, and 9.375 μM uric acid. Sample 6 contained 15 μM dopamine, 15 μM epinephrine, and 12.5 μM uric acid.

To prepare 0.5, 1.0, and 2.0 nM nanoparticle solutions, the stock nanoparticle solutions were centrifuged (Au@MUA nanoparticles = 11,500 RPM (8,797 x g), Au@TA nanoparticles = 11,500 RPM (8,797 x g) and Au@MHA nanoparticles = 10,000 RPM (7,932 x g)) for 20 minutes. The supernatant was removed and replaced with separation buffer. The concentration of the new stock solution was calculated using a standard estimation model.[89]

6.2.8 Capillary Electrophoresis

All separations were performed using a Beckman Coulter P/ACE MDQ (Brea, CA) capillary electrophoresis instrument equipped with a UV light source and UV or photodiode array (PDA) detector. The instrument was utilized per manufacturer recommendations. UV detection occurred at 200 nm, and PDA detection occurred at both 520 and 600 nm. The capillary temperature was maintained at 25° C. Fused silica capillary was purchased from Polymicro (Phoenix, AZ) with an internal diameter of 75 μm and an outer diameter of 360 μm. The total capillary length was 60.2 cm with a 50 cm effective separation length.

The capillary was conditioned using the following procedure: 0.1 M HNO_3 (20 psi for 5 minutes), H_2O (20 psi for 2.25 minutes), 1 M NaOH (20 psi for 2.25 minutes), H_2O (20 psi for 2.25 minutes), 250 mM sodium phosphate buffer (20 psi for 3 minutes), and 30 mM separation buffer (either with or without nanoparticles) depending on the experiment (20 psi for 3 minutes). Biomarker and nanoparticle samples were hydrodynamically injected into the capillary at 1 psi for 5 seconds, and separations were performed using normal polarity and a 20 kV separation voltage.

6.2.9 Capillary Electrophoresis Data Analysis

All electropherograms were processed using an in-house written Excel Macro application (Appendix A). For UV and PDA experiments, the raw data was processed into time, absorbance, current, and potential columns. The electroosmotic flow (EOF) velocities for all separations were adjusted to control experiments where no nanoparticles were present. Average analyte migration time differences were calculated using the control experiments and experiments performed with 0.5, 1.0, and 2.0 nM of Au@MUA nanoparticle concentrations. Peak areas of each potential biomarker peak were fit using OriginPro 7.5 equipped with a peak fitting module. Specifically, a two point linear baseline fit was manually assigned for each peak in the electropherogram. After baseline subtraction, peaks were fit using either a Gaussian or EMGaussian peak function for symmetric or asymmetric peaks, respectively. Reported peak areas are for the best fit peaks as determined by minimized chi-squared values. Average biomarker peak areas were normalized to the average peak area collected without any nanoparticles present. Averages and standard deviations for normalized migration times and peak areas were evaluated from at least 3 replicate separations and propagated errors. For PDA experiments, each electropherogram was smoothed using 50-point adjacent averaging before determining migration times or peak areas. Nanoparticle peak areas were determined using the same method as for the biomarkers.

6.3 Results and Discussion

6.3.1 Characterization of Au@MHA, Au@MUA, and Au@TA Nanoparticles

Achieving reproducible separations through the effective use of nanoparticle pseudostationary phases requires stable, shape, and size homogenous nanoparticles. Plasmonic nanomaterials (i.e. gold, silver, composites, etc.) exhibit localized surface plasmon resonance (LSPR) spectra, a size dependent property in which electromagnetic fields arise at nanoparticle surfaces.[67, 68] The LSPR of noble metal nanoparticles is (1) experimentally measured using extinction spectroscopy (i.e. scattered and absorbed light);[70] (2) dependent on the distance matter is from the nanoparticle surface;[71] (3) theoretically predicted using Mie theory;[72] and (4) dictated by nanoparticle composition, shape, size, and local environment surrounding the core nanomaterial.[72, 82]

The influence of self-assembled monolayers (SAMs) on the LSPR of gold nanoparticles is demonstrated in Figure 6.1A-C. Gold nanoparticles functionalized with thioctic acid, 11-mercaptoundecanoic acid, and 6-mercaptohexanoic acid display unique extinction spectra with characteristic extinction maxima wavelengths (λ_{max}). All three nanoparticle samples exhibit statistically identical (95% confidence interval) core sizes (Figure 6.1A-C TEM insets). The average core diameter is 12.7 ± 1.1 nm for all three carboxylic acid functionalized gold nanoparticle samples. Although all three nanoparticle samples exhibit the same core sizes, the λ_{max} red shifts from 522.3 to 524.7 nm for Au@MHA and Au@MUA nanoparticles, respectively, indicative of increased alkanethiol chain length.[70] Furthermore, it is well-established that thioctic acid binds to gold via a disulfide ring,[80, 81, 86] whereas 6-mercaptohexanoic acid and 11-mercaptoundecanoic acid bind via a single thiol bond.[199] The larger binding moiety of thioctic acid decreases the achievable SAM packing density vs. the other two ligands.[189, 200] As a result, the observed extinction maximum for Au@TA nanoparticles is

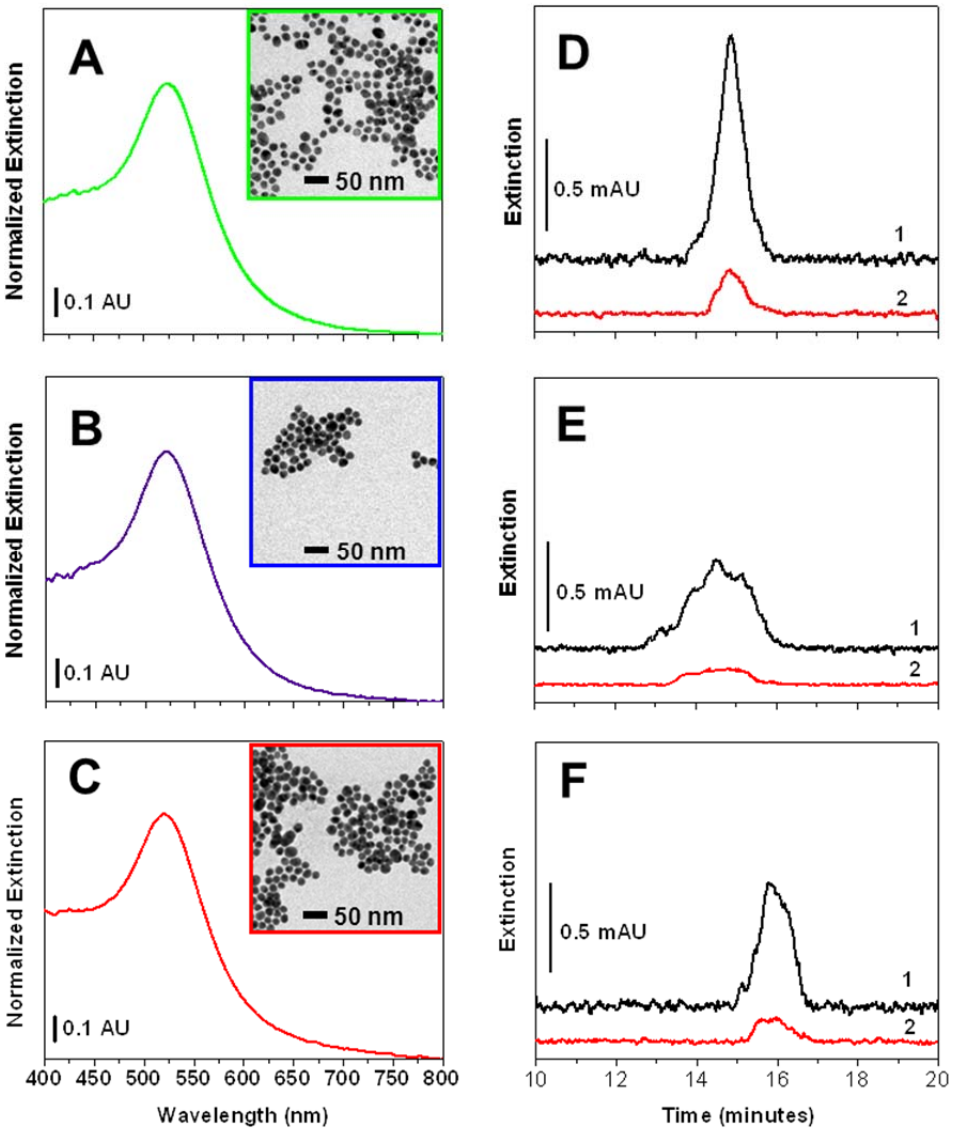

Figure 6.1 Extinction spectra and TEM inset of 1 nM (A) Au@MUA (λ_{max} = 524.7 nm), (B) Au@MHA (λ_{max} = 522.3 nm), and (C) Au@TA (λ_{max} = 521.5 nm) nanoparticles, respectively. Representative electropherograms from dual wavelength detection at (1) 520 and (2) 600 nm for a 2% plug of 1 nM (D) Au@MUA, (E) Au@MHA, and (F) Au@TA nanoparticles (separation voltage = 20 kV).

centered at 521.5 nm, a value blue-shifted from the two straight chain alkanethiol functionalized nanoparticles.

To use these nanostructures in a separation, nanoparticle concentration must be considered. For this reason, nanoparticle size was coupled with a standard estimation model to calculate the concentration of gold nanoparticles.[89] To do this, an average nanoparticle diameter is first obtained from TEM measurements. Based on this value, a corresponding molar extinction coefficient (ε) is calculated from the standard estimation model. Next, nanoparticle concentration is verified using the extinction intensity at 450 nm versus the extinction at its extinction maximum wavelength. In this way, nanoparticle concentration effects upon inclusion in continuous full filling pseudostationary phases could be studied during separations.

The pH-dependent surface charge or zeta potential is commonly used to assess nanoparticle stability.[272, 273] Previous studies revealed that carboxylic acid functionalized gold nanoparticles exhibited negative zeta potential values that ranged from 36 – 60 mV (pH 9).[106, 212] To distinguish differences between nanoparticles functionalized with various carboxylic acid terminated SAMs, zeta potential was measured. In these studies, nanoparticle concentration was maintained at 1 nM and solution conductivity of 5.5 mS cm^{-1}. The zeta potential of carboxylic acid functionalized Au nanoparticles is dependent on the ligand (pK_a),[106] packing density,[167] and surrounding environment.[166] For example, Au@TA nanoparticles reveal a zeta potential of -18.4 ± 1.3 mV which is not statistically different from that observed for Au@MHA nanoparticles (-20.9 ± 1.5 mV). This suggests that the carboxylic acid pK_a values and/or surface coverages for these two ligands are similar when bound to the surface of gold nanoparticles. MUA, which exhibits the most acidic pK_a in solution vs. the other two ligands, reveals a more negative zeta potential (-37.6 ± 3.5 mV) when bound to gold nanoparticles at pH = 7.3. This suggests that nanoparticle SAM packing density and pK_a both influence the effective surface charge and as a result, nanoparticle stability.

To better understand the implications of zeta potential measurements, chain length, and binding moiety on SAM packing density on Au nanoparticles, XPS is used. Expanding on previous methods [81], the packing density of carboxylic acid SAMs on gold nanoparticle surfaces can be estimated. It should be noted that (1) the core size of Au nanoparticles functionalized with MUA, MHA, or TA are not statistically different and (2) the surface of 12.7 ± 1.1 nm gold nanoparticles contain predominately (100) surface planes.[157, 158] As a result, the packing density of carboxylic acid terminated SAMs on gold nanoparticles can be approximated from XPS peak areas as follows:

$$\text{Packing density} = \left[\frac{S}{Au_{surface}}\right]\left[\frac{Ligand}{S}\right]\left[\sigma_{100}\right] \qquad (6.1)$$

where the first term is the corrected $S/Au_{surface}$ XPS signal, the second term is the ligand to sulfur ratio (1, 1, and 0.5 for MUA, MHA, and TA, respectively), and the third term is the gold atom packing density for a (100) surface plane (12.03 atoms nm^{-2}).[81]

Table 6.1 summarizes the corrected XPS signal and estimated SAM packing densities for Au@TA, Au@MHA, and Au@MUA nanoparticles. These data demonstrate that SAM packing density on Au@MUA nanoparticles increases by ~5.3% and ~16% relative to Au@MHA and Au@TA nanoparticles, respectively. These values are larger than previously reported thiol ligand packing densities on flat gold surfaces which range from $1.8x10^{14} – 2.1x10^{14}$ molecules/cm[160-162, 164, 274-276] These differences can be attributed to crystalline structures differences between the flat gold and nanostructured surfaces.[167]

Table 6.1 $S/Au_{surface}$ Atomic Ratio and Estimated SAM Packing Density for Au@TA, Au@MHA, and Au@MUA Nanoparticles.

	$S/Au_{surface}$ Atomic Ratio	**Packing Density x 10^{14} (molecules/cm^2)**
Au@TA	$0.83_9 \pm 0.01_5$	$2.20_0 \pm 0.03_9$
Au@MHA	$0.89_2 \pm 0.02_7$	$4.58_1 \pm 0.01_9$
Au@MUA	$0.96_3 \pm 0.02_9$	$4.97_5 \pm 0.01_8$

6.3.2 Evaluation of Carboxylic Acid Functionalized Au Nanoparticles in Capillary Electrophoresis

The large (~2.0 x 10^8 M^{-1} cm^{-1}) extinction coefficient of gold nanoparticles (LSPR) allows their stability to be easily monitored using visible wavelength detection coupled with capillary electrophoresis. Previously,[106] nanoparticle stability in a capillary was evaluated using a ratio of nanoparticle absorbance band areas monitored at λ= 520 and 600 nm using dual wavelength PDA detection. A similar approach was used to evaluate the optical stability of Au@MUA, Au@MHA, and Au@TA nanoparticles in the capillary. Representative electropherograms collected at λ= 520 and 600 nm for a 2% total capillary volume plug of 1 nM Au@MUA (Figure 6.1.D), Au@MHA (Figure 6.1.E), and Au@TA nanoparticles (Figure 6.1.F) injected into the capillary reveal both similarities and differences.

First, the electrophrograms collected at λ = 520 nm reveal a single band for all three nanoparticle functionalizations. Second, a less intense band with a similar migration time as the band collected at 520 nm is observed at λ= 600 nm. Evaluation of the band area ratios for all three nanoparticle samples are 5.4_3, 5.2_4, and 4.6_6 for Au@MUA, Au@MHA, and Au@TA nanoparticles, respectively. In general, more nanoparticle stability is assumed from large ratios.[106]

Despite these similarities, three significant differences are noted including: (1) band migration times, (2) peak areas and/or intensities, and (3) peak full width half maximum (FWHM) values. For instance, the average migration time of nanoparticle bands at 520 nm and 600 nm range from 14.5_5, 14.7_1, and 15.8_7 minutes for Au@MUA, Au@MHA, and Au@TA nanoparticles, respectively. In CE, analyte migration time and electrophoretic mobility (μ) depend on charge (q) and Stokes radius (r) as described in Equation 6.2.

$$\mu = \frac{q}{r} \tag{6.2}$$

As a result, nanoparticle elution order and migration time depend on the surface charge (zeta potential) and hydrated radii for each functionalize nanoparticle. While Au@MUA nanoparticles exhibit the most negative zeta potential, the mobility of these nanoparticles are large compared to the other functionalized nanostructures. We hypothesize that the hydrated radius of these Au@MUA nanostructures are small and govern these surface chemistry driven trends.

Second, peak area and intensity differences are clearly noted among the three functionalized nanoparticles in Figure 6.1D-F. Despite injecting equal concentrations of nanoparticles, peak areas for Au@MUA nanoparticles are ~1.5 times more intense than that for either Au@MHA or Au@TA nanoparticles, respectively. We attribute the similarity in peak areas for Au@MHA and Au@TA nanoparticles to similarities in the observed zeta potential values (-18.4 and -20.9 mV, respectively). Au@MUA nanoparticles are relatively more negative (-37.6 mV) in these buffer conditions - a value that likely arises from a higher density of MUA molecules (4.97×10^{14} molecules/cm^2) as compared to the other two ligands. As a result, Au@MUA nanoparticles are hypothesized to interact with the negatively charged capillary wall to a lesser extent thereby exhibiting more intense and narrow peaks than either Au@MHA or Au@TA nanoparticles.

Finally, nanoparticle band FWHM values differ significantly among the three functionalized nanoparticle samples (Figure 6.1D-F). FWHM values collected at 520 nm are 56, 100, and 65 seconds for Au@MUA, Au@MHA, and Au@TA nanoparticles, respectively. Band broadening generally occurs via three mechanisms: longitudinal diffusion, mass transfer, and Eddy diffusion.[277] Because all three nanoparticle samples exhibit no evidence of aggregation (520 to 600 nm peak intensity ratio), Eddy diffusion is assumed to be ~0. Band broadening from longitudinal diffusion and mass transfer (i.e. nanoparticle-capillary interactions) will increase and decrease, respectively as the time the nanoparticles spend in the capillary increases. Au@MUA nanoparticle plugs migrate more quickly and exhibit the narrowest, most symmetric peak shapes of three samples. Because the migration times for the three samples differ by less than 1.5 minutes, longitudinal diffusion differences are likely minimal. None of these mechanisms adequately explain these trends; therefore, we attribute these differences to nanoparticle surface chemistry.

6.3.3 Potential PD Biomarker Separations as a Function of Nanoparticle Concentration

Because Au@MUA nanoparticles exhibited minimal interactions with the capillary wall, these nanostructures were added to the separation buffer at varying concentrations and used to optimize the separation of the possible Parkinson's disease biomarkers dopamine, epinephrine, and uric acid (5.5 mS/cm pH 7.3 phosphate buffer containing 0.5, 1.0, or 2.0 nM Au@MUA nanoparticles). The detector was auto-zeroed at the start of the separation to remove any background interferences from the buffer and/or nanoparticles, and the biomarkers were detected at $\lambda = 200$ nm. Several nanoparticle-related trends are observed in Figure 6.2. First, biomarker elution order depends on their electrophoretic mobilites and *not* on the presence or absence of the nanoparticles.

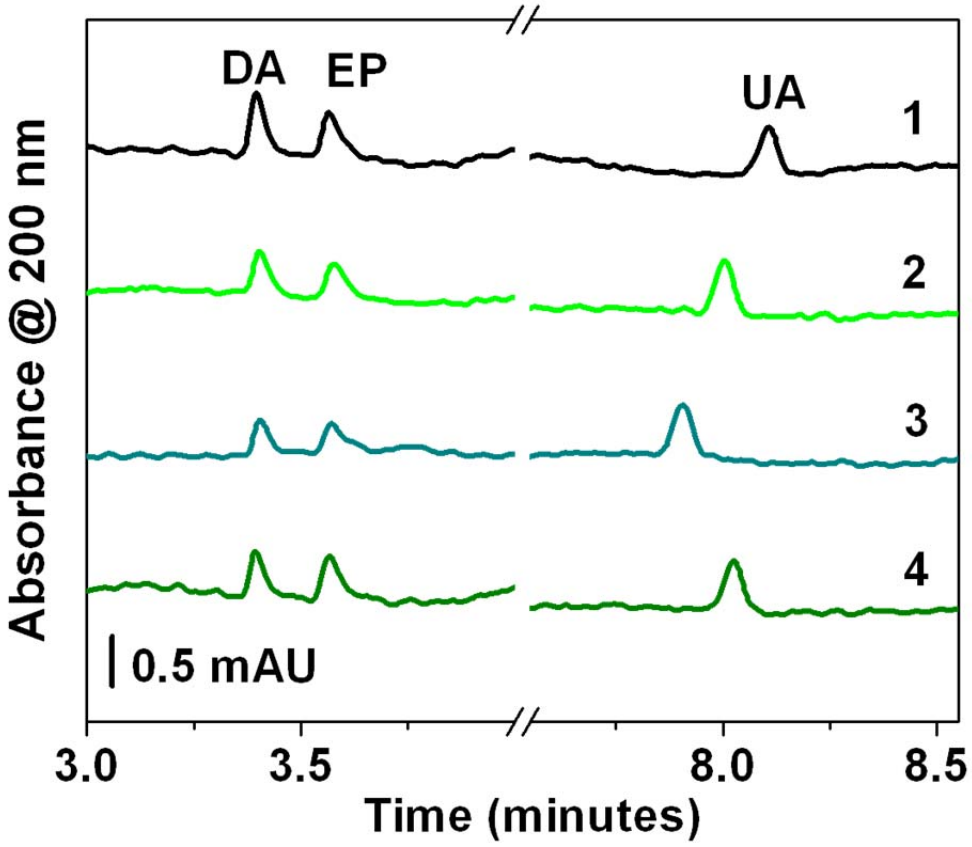

Figure 6.2 Evaluation of trends in the peak areas of PD biomarkers as a function of nanoparticle concentration. Representative electropherograms for the separation of PD biomarkers in the presence of (1) 0, (2) 0.5, (3) 1.0, and (4) 2.0 nM Au@MUA nanoparticles included in the separation buffer. 30 mM sodium phosphate buffer (pH = 7.3, 5.5 mS/cm) is used, and the "sample" is injected (1 psi for 5 seconds) into the capillary. Separation voltage = 20 kV, λ_{det} = 200 nm, and a ~4 minute window that included the electroosmotic band was removed for clarity. The analyte peaks are labeled as follows: dopamine (DA), epinephrine (EP), and uric acid (UA).

Second, increasing the Au@MUA nanoparticle concentration from 0.5 to 1 nM slightly increases the migration time for both dopamine (1.5_5 sec) and epinephrine (1.9_5 sec). Conversely, uric acid migrates more quickly as Au@MUA nanoparticle concentration increases from 0 to 1 nM. Above 2 nM, Au@MUA nanoparticle separations are irreproducible. Third, peak areas of dopamine and epinephrine decrease as a function of increasing nanoparticle concentrations. Finally, unlike cationic dopamine or epinephrine, the peak area for anionic urate increases slightly as Au@MUA nanoparticle pseudostationary phase concentration increases. These changes indicate that Au@MUA nanoparticles interact with and/or influence the apparent mobilities of the biomarkers.

6.3.4 Evaluating Trends in Biomarker Migration Times

Nanoparticle pseudostationary phase applications in CE separations were previously reviewed.[253] Utilizing nanoparticles in a continuous full fill mode[30, 103] requires optimization of nanoparticle concentration to produce targeted separation effects while not adversely impacting reproducibility. Thus, nanoparticles functionalized with varying surface chemistries exhibit characteristic critical nanoparticle concentrations (CNC).[106] The CNC, a parameter similar to the critical micelle concentration in micellar electrokinetic chromatography, is the lowest nanoparticle concentration that induces nanoparticle aggregation (versus stable nanoparticles) under specific buffer conditions and leads to irreproducible separations. Previously reported CNC values for Au@MHA functionalized nanoparticles is 1.8 nM at pH 9.3.[106]

In the current study, similar CNCs are observed for Au@MUA nanoparticles as separation reproducibility is poor when nanoparticle concentration approaches 2 nM. This is apparent when biomarker migration times are analyzed according to Au@MUA nanoparticle concentration (Figure 6.3). It should be noted that these results are referenced to assays performed in the absence of nanoparticles. Two classes of trends are observed. First, at 0.5 and 1 nM Au@MUA nanoparticle concentrations, no significant

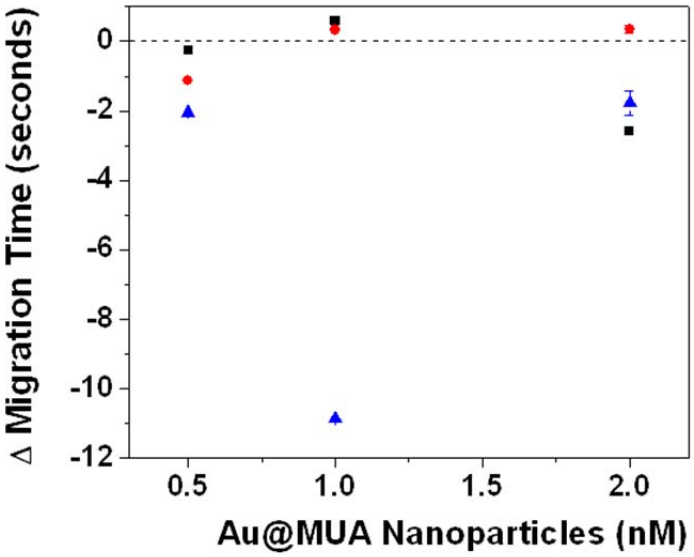

Figure 6.3 Evaluation of the migration time trends for PD biomarkers: (■) dopamine, (●) epinephrine, and (▲) uric acid as a function of Au@MUA nanoparticle concentration. Changes in migration times are reported relative to assays performed in the absence of Au@MUA nanoparticles. Same separation conditions as in Figure 6.2.

changes are measured in the migration times for dopamine, epinephrine versus controls.[278] Second, the migration time for the urate anion decreases by 10.8 ± 0.034 seconds relative to controls as Au@MUA nanoparticle concentration increase. This effect is attributed to repulsive forces between the anionic biomarker and Au@MUA nanoparticles

Regardless of these small changes, surface chemistry is important for directing the interactions between the nanoparticles and biomarkers during a separation. Furthermore, surface chemistry facilitates nanoparticle stability and separation reproducibility. Because 1 nM Au@MUA nanoparticles revealed the most consistent and significant separation results, this nanoparticle concentration was selected for all subsequent bioassays.

6.3.5 Evaluating Trends in Normalized Biomarker Peak Areas in the Presence of 1 nM Gold Nanoparticle Containing Buffers

As previously stated, each of the studied biomarkers possesses an inherent pK_a value which induces either a negative or positive charge based on the buffer conditions. These electrostatic differences can be exploited to understand the selective interaction between the negatively charged, functionalized Au nanoparticles and potential Parkinson's disease biomarkers in CE. The extent of attraction or repulsion is accessed via comparison to control experiments (no nanoparticles present).

While all three covalently functionalized nanoparticles are negatively charged, Au@MUA nanoparticles contain the most densely packed monolayers which leads to the most systematic trends vs. the other nanoparticles studied. As a result, Au@MUA nanoparticles are used to evaluate how biomarker concentration impacts nanoparticle-

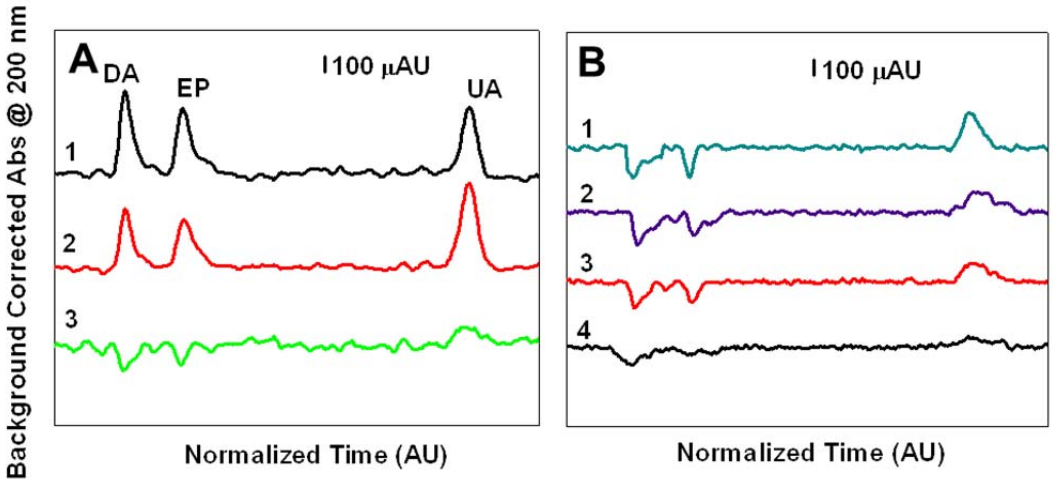

Figure 6.4 Evaluation of PD biomarker peak areas as a function of increasing Au@MUA nanoparticle concentration. (A) Representative electropherograms for separations performed with buffer containing (1) 0 and (2) 1.0 nM Au@MUA nanoparticles. (3) Electropherograms difference plot between (1) and (2). (B) Electropherogram difference plots for various concentrations of biomarkers performed with 1.0 nM Au@MUA nanoparticle containing buffer. Sample 1 contains 1.56 μM dopamine, 1.56 μM epinephrine, and 0.78 μM uric acid; sample 2 contains 3.25 μM dopamine, 3.25 μM epinephrine, and 1.56 μM uric acid; sample 3 contains 6.25 μM dopamine, 6.25 μM epinephrine, and 3.25 μM uric acid, and sample 4 contains 9.375 μM dopamine, 9.375 μM epinephrine, and 6.25 μM uric acid. 30 mM sodium phosphate buffer (pH = 7.3. 5.5 mS/cm) is used, and the "biomarker" is injected (1 psi for 5 seconds) into the capillary. Separation voltage = 20 kV, λ_{det} = 200 nm and the analyte peak are labeled as follows: dopamine (DA), epinephrine (EP), and uric acid (UA).

dictated mechanisms. In these studies, separations were performed in the absence (Figure 6.4A-1) and presence (Figure 6.4A-2) of 1 nM Au@MUA nanoparticle containing buffer. Several interesting trends are observed for these data. First, there is a significant decrease in peak areas for positively charged dopamine and epinephrine. Peak area loss for these analytes is attributed to electrostatic interactions between the negatively charged carboxylic acid headgroups on Au@MUA nanoparticle surfaces and positively charged biomarkers. Second, uric acid reveals an *increase* in peak area. If no partitioning and/or solubility differences exist, there should be an electrostatic repulsion between the anionic uric acid biomarker and carboxylated Au nanoparticles. As a result, we attribute this area enhancement to sample stacking. This phenomenon occurs when the conductivity of the injected sample is lower than the surrounding buffer inducing an enriched concentration analyte zone.[269, 279]

To better illustrate these nanoparticle effects, a difference electropherogram is included in Figure 6.4A-3. To account for migration time differences, the time scale was normalized prior to subtracting nanoparticle free from nanoparticle containing electropherograms. By doing this, differences in electropherograms can be generated where negative and positive peak areas indicate peak area losses and gains, respectively. These effects are biomarker concentration dependent, where increasing the biomarker concentration diminishes peak area losses or gains (Figure 6.4B).

Figure 6.5 demonstrates the impact of a 1 nM Au@MUA nanoparticle-containing separation buffer as a function of (A) dopamine, (B) epinephrine, and (C) uric acid concentrations. As the concentration of dopamine, epinephrine, and uric acid increase, the impact of nanoparticles on biomarker peak areas diminishes (i.e. the greatest effect is observed for the lowest biomarker concentrations). For instance, 1.5 μM dopamine and epinephrine containing sample matrices reveal peak area decreases by ~30 % and ~25 %, respectively, due to electrostatic interactions between the biomarkers and the Au@MUA nanoparticle surface. Above 8 and 6 μM dopamine and epinephrine concentrations,

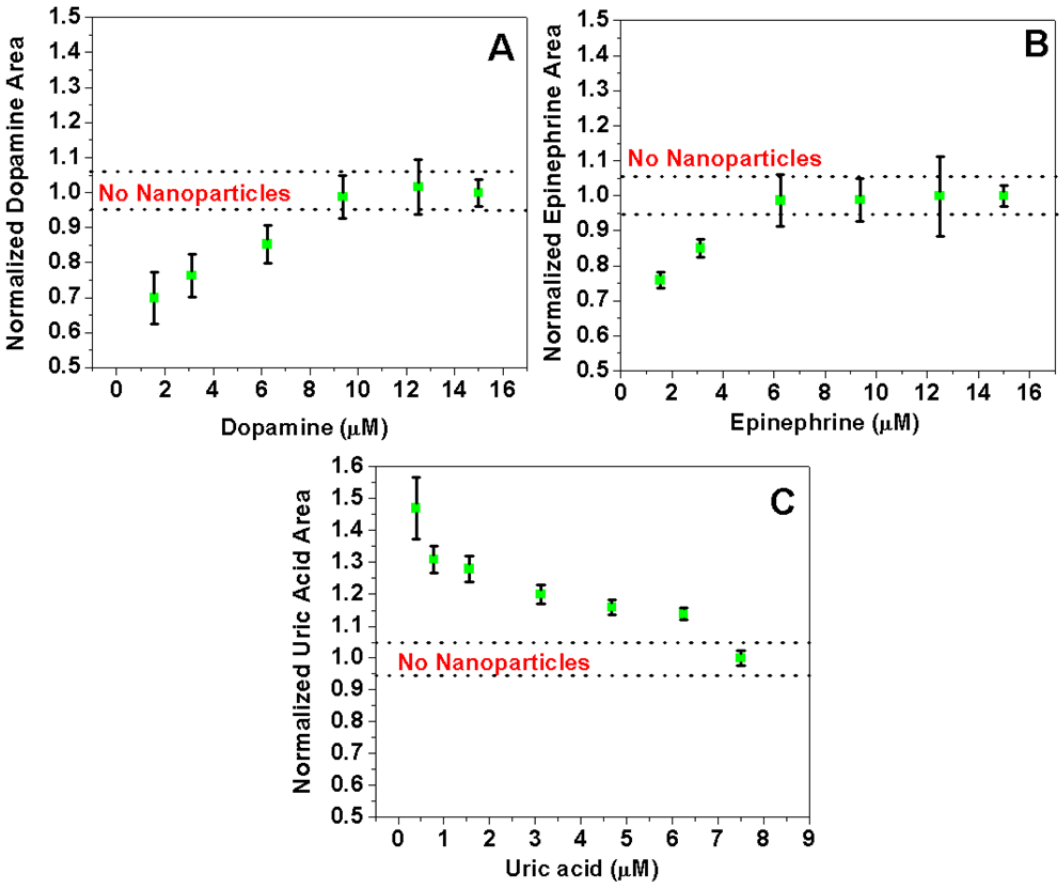

Figure 6.5 Evaluating normalized (A) dopamine, (B) epinephrine, and (C) uric acid peaks areas as a function of concentration in the presence of 1 nM Au@MUA. In all cases, the dotted line region around 1 represents the error of the controls (no nanoparticles present in the separation buffer). Same separation conditions used as in Figure 6.4

respectively, no observed peak area differences between nanoparticle containing and nanoparticle free assays are observed. Conversely, opposite effects are shown for uric acid. At most uric acid concentrations, peak areas increase relative to no nanoparticle-containing assays. As with cationic biomarkers, these effects are maximized at the lowest uric acid concentration. Significant normalized peak area increases result from electrostatic repulsions between the nanoparticle and anionic analyte.

While trends are less clear (presumably from less robust surface chemistries), buffers containing 1 nM Au@MHA nanoparticles reveal a ~28 % and ~12 % peak area decrease for 1.5 μM epinephrine and 1.5 μM dopamine bands, respectively (Figure 6.6). No systematic trends or reproducable separation impacts are observed in the presence of buffer containing 1 nM Au@TA nanoparticles (Figure 6.7).

6.3.6 Evaluating Nanoparticle-Dopamine Interactions

To investigate the mechanism of functionalized gold nanoparticles and the target biomarkers, the zeta potentials of 1 nM Au nanoparticle solutions incubated in varying dopamine concentrations are measured. Biomarker concentration-dependent trends are evaluated by incubating 1 part 1 nM Au@MUA, Au@MHA, and Au@TA nanoparticles with 0, 25,000, 125,000, 2,500,000, and 5,000,000 dopamine mole ratios. The normalized zeta potentials for Au@MUA, Au@MHA, and Au@TA nanoparticles are presented in Figure 6.8. To directly compare the three functionalized Au nanoparticle samples, all zeta potential measurements were normalized to nanoparticle zeta potential values in the absence of dopamine. Deviations relative to this value after incubation in dopamine represent a decrease in normalized zeta potential magnitude. Similar dopamine-concentration dependent trends are observed for all three functionalized nanoparticles. At low nanoparticle to dopamine mole ratios, only slight differences in normalized zeta potential are observed for Au@MUA, Au@MHA, and Au@TA nanoparticles. Increasing the nanoparticle to dopamine mole ratio to 1:25,000, dopamine neutralizes ~10% of the

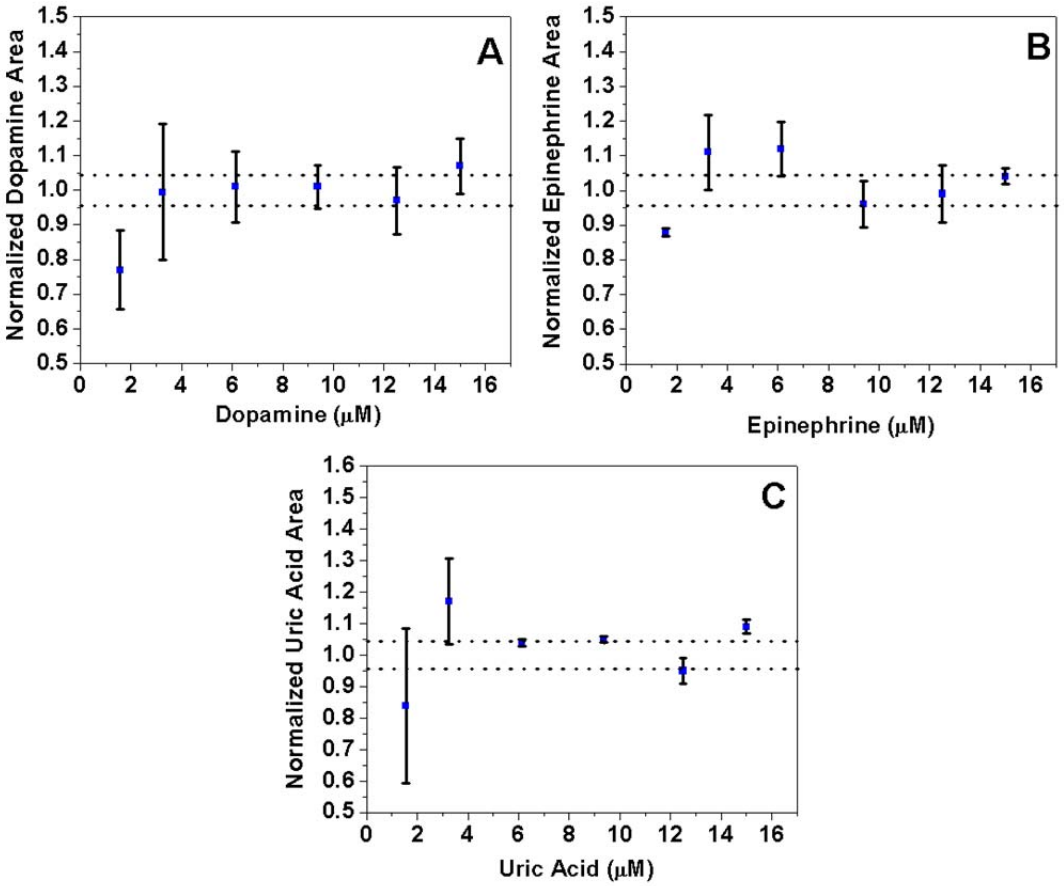

Figure 6.6 Evaluating the normalized dopamine, epinephrine, and uric acid peak areas as a function of concentration in the presence of 1 nM Au@MHA nanoparticle solutions. In all cases, the dotted line region around 1 represents the error of control (no nanoparticles present in the separation buffer). Same separation conditions used as in Figure 6.4.

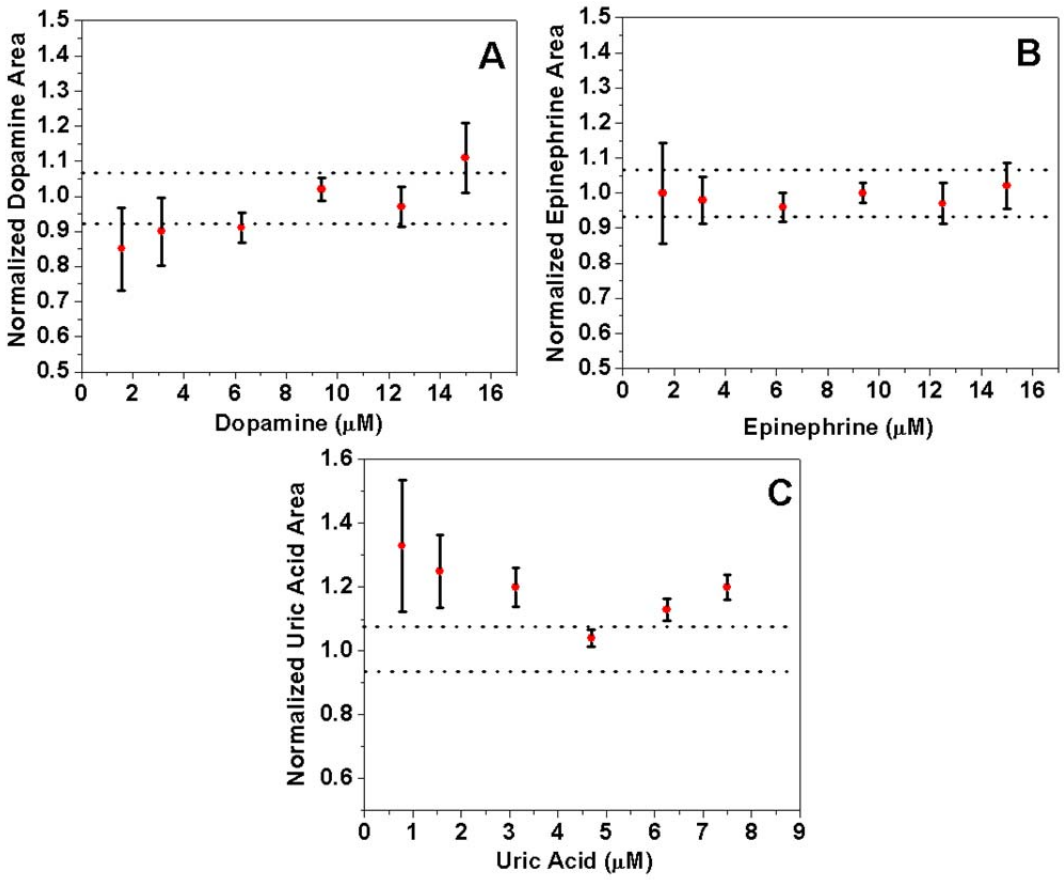

Figure 6.7 Evaluating the normalized dopamine, epinephrine, and uric acid peak areas as a function of concentration in the presence of 1 nM Au@TA nanoparticle solutions. In all cases, the dotted line region around 1 represents the error of control (no nanoparticles present in the separation buffer). Same separation conditions used as in Figure 6.4.

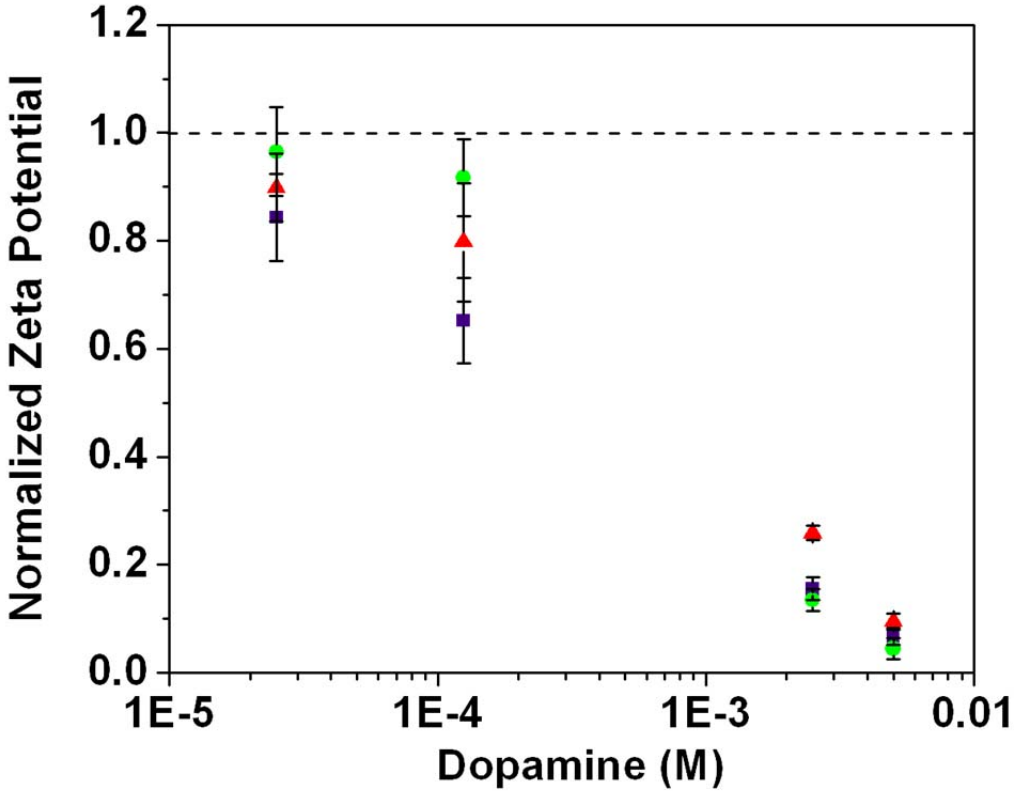

Figure 6.8 Normalized zeta potential decreases as a function of increasing dopamine concentration in the presence of 1 nM Au@MUA (●), Au@MHA (■), and Au@TA (▲) nanoparticle solutions were recorded as a function of increasing dopamine concentrations. Changes in zeta potential are reported relative to assays performed in the absence of dopamine.

nanoparticle surface charge. Because Au nanoparticles functionalized with MUA contain the most densely packed and stable SAM, the largest impacts are observed with Au@MUA nanoparticles as compared to other functional groups. At high nanoparticle to dopamine concentrations, all three functionalized gold nanoparticle samples exhibit significant changes in zeta potential, and dopamine effectively shields the stabilizing carboxylic acid groups on the nanoparticle surface.

Several methods can be used to model these electrostatic interactions. For instance, the change in normalized zeta potential are plotted as a function of dopamine concentration (Figure 6.9). A Langmuir isotherm[73] poorly describes these data because (1) dopamine and deprotonated carboxylated surface sites may not bind in a 1 to 1 ratio; (2) each deprotonated carboxylate group may not independently bind to dopamine; and (3) binding cannot be assumed to be only electrostatic in nature (i.e. no partitioning into the SAM by dopamine). Instead, a dose curve response was used to model the data:

$$y = \frac{A_1 - A_2}{1 + \left(\frac{x}{x_0}\right)^{\rho}} + A_2 \qquad (6.3)$$

where A_1 and A_0 are the upper and lower zeta potential response offsets, respectively; ρ is the Hill's slope parameter; and x_0 is the half dose response concentration.

To apply this half dose response equation, the weak acid (or base) equilibrium of both the SAMs and dopamine must be considered. At pH 7.3, the Henderson-Hasselbach equation coupled with the SAM packing density can be used to approximate the number of deprotonated carboxylic acid groups on the nanoparticle surface. It is clear from this model that a half dose response occurs when ~640 μM dopamine is added to the nanoparticle solution.

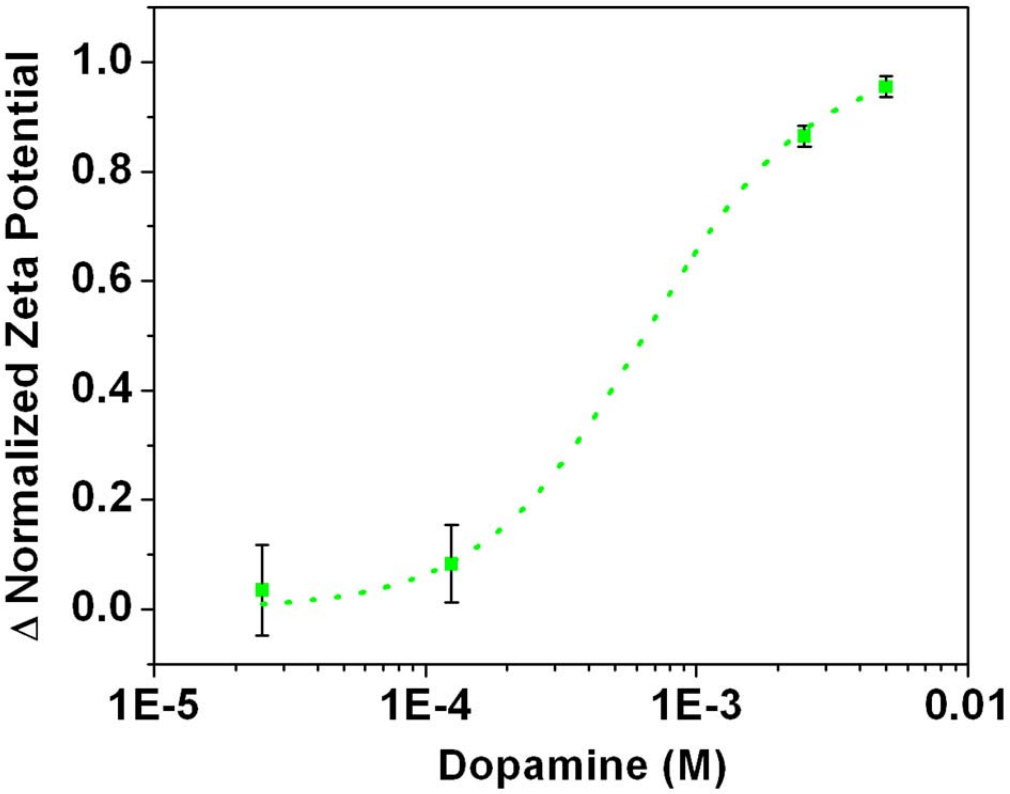

Figure 6.9 Difference in normalized zeta potential increases as the dopamine to Au@MUA nanoparticle ratio increases. The dotted line represents the half dose response fitting for the change in normalized zeta potential vs. titrated dopamine concentrations data: $y = A_2 + (A_1 - A_2 / 1 + (x/x_0)^p)$. The half dose response for these data was ~640 μM dopamine.

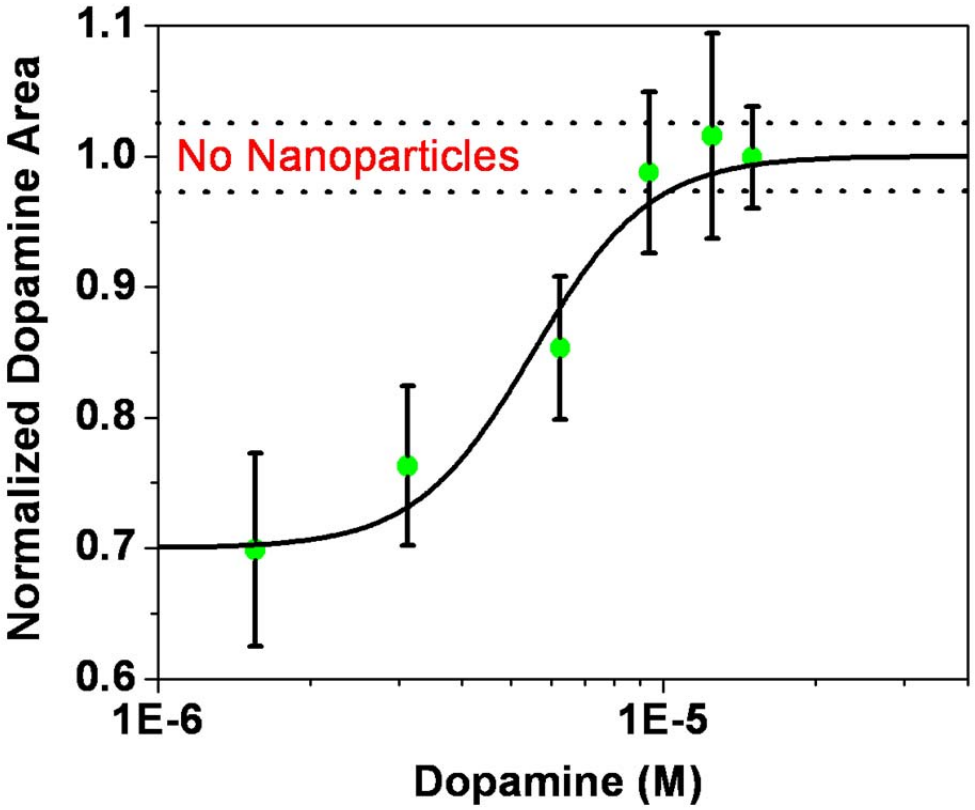

Figure 6.10 Difference in normalized dopamine area decreases as the dopamine to Au@MUA nanoparticle ratio increases. The solid line represents the dose response curve for the change in normalized dopamine area vs. dopamine concentration data: $y = A_2 + (A_1 - A_2 / 1 + (x/x_0)^p)$. The half dose response for these data is ~5.5 μM dopamine.

Using this same model to the data collected with CE (Figure 6.10), a half dose of ~5.5 μM is estimated - a value approximately an order of magnitude greater than the zeta potential measurements (Figures 6.9). This suggests that more dopamine is required to neutralized half of the deprotonated carboxylic acid SAMs. This discrepancy can be explained via temporal differences in the experiments. For example, the dopamine-nanoparticle titration experiments were allowed to incubate for one hour versus the ~ 3 minute incubation times allowed in CE. As a result, increased interactions/incubation times in CE will likely result in more similar half-dose response concentrations for biomarkers as observed in zeta potential measurements.

6.4 Conclusions

The capillary electrophoresis separation of the proposed Parkinson's disease biomarkers dopamine, epinephrine, and uric acid were evaluated using Au@MUA, Au@MHA, or Au@TA nanoparticles suspended in the separation buffer. Nanoparticle stability in the separation buffer was evaluated using LSPR spectroscopy, zeta potential measurements, and XPS. Au@MUA nanoparticles were found to contain the greatest SAM packing density and as a result, were the most stable nanostructures versus Au@MHA and Au@TA nanoparticles.

When included in the separation buffer, nanoparticle functionalization dictated interactions with biomarkers and other nanoparticles. Cationic Parkinson's disease biomarkers (dopamine and epinephrine) experienced slight decreases in velocities for Au@MUA nanoparticles, while the velocity of uric acid increased. These trends were concentration dependent until a CNC was achieved resulting in nanoparticle aggregation which reduced separation repeatability.

In separations performed using Au@MUA, Au@MHA, and Au@TA nanoparticle pseudostationary phases, cationic dopamine and epinephrine electrostatically interacted with the nanoparticle surfaces. These effects depended SAM packing density and

biomarker concentrations. These data were described using a half dose response function. The half dose response concentration was estimated at 5.5 μM dopamine. To further understand these results. Similar Au@MUA nanoparticle and dopamine interaction studies were evaluated with zeta potential. For high dopamine concentrations, all three functionalized gold nanoparticles experienced neutralized surface potentials revealing a half dose response concentration of 0.64 μM dopamine. The discrepancy in half dose response concentrations was attributed to equilibrium (zeta potential) vs. non-equalibrium (CE) measurement conditions. Further investigations of nanoparticle interactions with biomarkers, the capillary, and other nanoparticles should lead to systematic improvements in biomarker separations and subsequent detection of target biological and chemical species.

CHAPTER 7
CONCLUSIONS AND FUTURE DIRECTIONS

7.1 Conclusions

The work presented here consists of the synthesis and characterization of carboxylic acid functionalized gold nanoparticles. The methods used and the results published from these studies can be applied to future work towards understanding and facilitating the integration of nanomaterials as pseudostationary and stationary phases in capillary electrophoresis.

Chapter 1 reviewed the use of nanomaterials as pseudostationary and stationary phases in electrically driven capillary separations. The advantages of nanomaterial for these applications are numerous and include small/tunable sizes, core composition variations, flexible injection/introduction methods in separation techniques, and diverse surface chemistry options. Nanomaterials, however, exhibit inherently large surface energies which are minimized upon aggregation and/or surface chemistry modification. As a result, these materials can yield unpredictable function in separations. Furthermore, nanomaterials can adversely impact separations by changing buffer conductivity, viscosity, and pH which requires a careful balance in nanoparticle stability and separation optimization. Finally, nanomaterials can complicate detection by inducing an inconsistent background. A unified mechanism which predicts the structure-function relationship of a nanomaterial phase to separation effects is complex, dynamic, and often not thoroughly understood. In this dissertation, a rigorous evaluation of nanoparticle core and surface properties was used to develop a better mechanistic understanding of nanomaterial interactions in capillary electrophoresis.

Initially, the characterization and optimization of gold nanoparticles with tailored surface chemistries was described in Chapters 2 and 3. Specifically, Chapter 2 focused on the synthesis and characterization of thioctic acid functionalized gold nanoparticles. In

summary, gold nanoparticles functionalized with thioctic acid were prepared with the slow addition of NaCl. TEM, ^{1}H NMR, extinction spectroscopy, zeta potential, XPS, and flocculation studies determined that the self-assembly of thioctic acid on gold nanoparticles increases with increasing NaCl concentration.

An increase in NaCl was shown to decrease the Debye length surrounding the deprotonated carboxylate groups on the assembled thioctic acid molecules thereby facilitating increased SAM packing densities. Furthermore, the slow addition of NaCl to gold nanoparticles during thioctic acid self assembly increased subsequent functionalized nanoparticle stability vs. controls as determined from flocculation studies. We expect these results to improve strategies for reproducible SAM formation on solution-phase nanostructures. Future studies could be expanded to investigate how nanoparticle shape, size, and radius of curvature impact this self assembly process for ultimate improvements in the reproducible synthesis and use of nanomaterials in a variety of applications.

Chapter 3 investigated the surface chemistry on and morphology of gold nanoparticles functionalized with thioctic acid, 6-mercaptohexanoic acid, and 11-mercaptoundecanoic acid. This study used multiple techniques to evaluate the synthesis and functionalization of gold nanoparticles. The gold nanoparticle core composition, shape, size, SAM formation kinetics, and SAM packing density were evaluated. LSPR spectroscopy was used to monitor SAM formation kinetics onto gold nanoparticles. Ligand chain length was found to impact SAM formation. 11-Mercaptoundecanoic acid SAMs exhibited faster kinetics than both 6-mecaptohexanoic acid and thioctic acid SAMs. Furthermore, slower SAM formation kinetics was demonstrated for thioctic acid (dithiol) than for either 6-mercaptohexanoic acid (monothiol) or 11-mercaptoundecnanoic acid (monothiol).

Functionalized nanoparticles were dispersed into buffers ranging in pH from 3 to 11 and evaluated using the flocculation parameter. The longer alkanethiol chain length of 11-mercaptoundecanoic acid exhibited a pK_a value which more closely resembles the free

ligand in solution than either Au@MHA or Au@TA nanoparticles. Using flocculation parameter data, pK_a values were calculated at 6.3_0, 6.9_0, and 5.6_7 for Au@TA, Au@MHA, and Au@MUA nanoparticles, respectively. Resultantly, Au@MUA nanoparticles were stable over the greatest pH range vs. other nanostructures.

Four significant ^1H NMR spectral characteristics were observed: (1) peak broadening as a result of binding to the gold nanoparticle surface; (2) the absence of free ligand signatures superimposed on the surface-bound ligand spectrum; (3) the disappearance of protons associated with thiols for 11-mercaptoundecanoic acid and 6-mercaptohexanoic acid after binding to the gold surface; (4) chemical shift differences between free ligand and surface-bound ligands. Similar observations were made for all three nanoparticle species studied. As expected, these data help reconcile how these three ligands attach to the surface of the gold nanoparticles.

The gold nanoparticle SAM ligand packing density was evaluated using zeta potential and XPS. The zeta potential of Au@TA, Au@MHA, and Au@MUA nanoparticles was dependent on ligand structure (chain length and binding moiety) and SAM packing density. Qualitative zeta potential comparisons revealed similar surface charges for Au@TA and Au@MHA nanoparticles while Au@MUA nanoparticles were twice as negative indicating highly ordered and densely packed SAMs. XPS quantified packing densities revealed that AU@MUA and Au@MHA nanoparticles contained similar packing densities that were greater than that for AU@TA nanoparticles. These data suggested that zeta potential measurements are likely more sensitive to SAM order than XPS.

Next, Chapter 4 focused on the applications of gold nanoparticle as pseudostationary phases in capillary electrophoresis. Gold nanoparticles functionalized with SAMs composed of thioctic acid and either 6-mercaptohexanoic acid or 6-aminohexanethiol were injected into the capillary as discrete plugs to affect the separation of possible Parkinson's disease biomarkers. In summary, the optical properties

of covalently functionalized gold nanoparticles were used to investigate nanoparticle stability as well as the mobilities of dopamine, epinephrine, and pyrocatechol in capillary electrophoresis. The stability of both amine and carboxylated gold nanoparticles were determined using extinction spectroscopy and zeta potential measurements outside the capillary. Inside the capillary, the lowest nanoparticle concentration which induced aggregation (i.e. CNC) was subsequently evaluated using dual wavelength PDA detection. These findings demonstrated that effective nanoparticle surface charge impacts interactions of nanoparticles with analytes, the capillary wall, and other nanoparticles. These interactions directly influenced nanoparticle mobility. Furthermore, the mobilites of the studied Parkinson's disease biomarkers increased in the presence of aminated nanoparticles but decrease slightly with carboxylated nanoparticles. Below the CNC, this observation was dominated by the formation of a mobile pseudostationary phase at the capillary wall which was hypothesized to increase local buffer viscosity.

Chapter 5 evaluated how functionalized gold nanoparticle pseudostationary phases behaved during capillary electrophoresis. When included in the separation buffer; Au@MUA, Au@MHA, and Au@TA nanoparticles impacted the measured currents during electrically driven flow in a surface chemistry dependent manner. Extended DLVO theory was used to model the interparticle interactions of the three functionalized nanoparticles types and was correlated to nanoparticle stability within the capillary. Au@MUA nanoparticles suppressed current, while Au@MHA and Au@TA nanoparticles both enhanced the current. Au@MHA or Au@TA nanoparticles were both experimentally and theoretically shown to aggregate and experience electron tunneling effects between nanoparticles thereby increasing currents vs. Au@MUA nanoparticles. In all cases, these effects were concentration dependent and limited by the CNC.

Chapter 6 examined nanoparticle concentration and surface chemistry effects on the separation of hypothesized Parkinson's disease biomarkers. The impact of SAM composition and packing density on gold nanoparticle continuous full fill

pseudostationary phases were evaluated during the separation of dopamine, epinephrine, and uric acid. Cationic Parkinson's disease biomarkers (dopamine and epinephrine) experienced slight increases in velocities for Au@MUA nanoparticles, while the velocity of uric acid decreased. These trends were concentration dependent until the CNC was exceeded. These effects were systematic with SAM packing density and revealed that Au@MUA nanoparticles exhibited the largest effects followed by Au@MHA nanoparticles then Au@TA nanoparticles. Furthermore, these effects were dependent on biomarker concentrations where above a saturation concentration, peak area differences were detected. To understand these interactions, functionalized gold nanoparticles were incubated with dopamine, and zeta potential was monitored to evaluate trends in separation data. As the dopamine concentration increased, all the three functionalized gold nanoparticles experienced neutralized surface potentials. These responses followed dose response curve functions and half dose response concentration for dopamine was quantified.

7.2 Future Directions

In closing, the use of nanomaterial pseudostationary and stationary phases in separations will likely expand because of resulting improvements in the mechanistic understanding of the structure and function of these materials as well as both separation selectivity and detection advantages. The advantages of nanomaterial incorporation into CE are numerous and include small/tunable sizes, core composition variations, flexible injection/introduction methods in separation techniques, and diverse surface chemistry options. Nanomaterials, however, exhibit inherently large surface energies which can change upon aggregation and/or surface chemistry modification, and as a result, yield unpredictable function in separations.

The optimization and characterization of gold nanoparticles with tailored surface chemistries is an area of study which will be crucial for overcoming these limitations and

realizing new applications.Future research directions could focus on (1) further improving gold nanoparticle core synthesis and surface chemistry functionalization, (2) addressing the challenges of incorporating these nanomaterials into reproducible separations, and (3) additional investigations into nanoparticle interactions with biomarkers, the capillary, and other nanoparticles. New surface functionalization schemes where monolayers containing thiolated PEGs could be used to further promote nanoparticle stability and reduce the probability of uncontrolled aggregation during separations. Alternatively, various SAM functionalities (amine, hydroxyl, etc.) could be conjugated to nanoparticle surfaces. This approach would facilitate more flexibility in nanoparticle stability in various pH and ionic strength environments. Finally, other nanoparticles (i.e. shape, size, and core composition) could be utilized to evaluate how nanoparticle core properties impact separations. When coupled with the characterization tools described in this dissertation, these proposed studies would provide a comprehensive understanding of how the structure of nanoparticle pseudostationary phases impact their function in separations and other applications.

APPENDIX A

32 KARAT GOLD SOFTWARE CONVERSION MACROS

PDA CE Instrument File Conversion Macro

The following macros are written to work for the 32 gold software package from the Beckman Coulter P/ACE MDQ capillary electrophoresis instrument.

```
' Macro recorded 01/6/2011 by Mike Ivanov and Amanda Jones
' Keyboard Shortcut: Ctrl+i
'Open text file.
    FileOpenName = Application.GetOpenFilename
    If FileOpenName = False Then Exit Sub
    Workbooks.Open FileOpenName
    ActiveSheet.Range("A:A").TextToColumns DataType:=xlDelimited,
Comma:=True
    Application.ScreenUpdating = False
'Creates a data set based on the number of points in a file, currently it uses data
already contained in the file
'dataset = InputBox("How many data points are in the set?")
    dataset = Range("B9")
'Initializes a data counter and declares variables
    Dim dataset2 As Integer
    Dim dataset3 As Integer
    Dim dataset4 As Integer
    Dim dataset5 As Integer
    Dim dataset6 As Integer
    Dim dataset7 As Integer
```

```
    dataset2 = dataset * 2
    dataset3 = dataset * 3
    dataset4 = dataset * 4
    dataset5 = dataset * 5
    dataset6 = dataset * 6
    dataset7 = dataset * 7
'Rename active sheet, create new data sheets, and sort data.
    ActiveSheet.Name = "Original Data"
    Range("A:I").Select
    Selection.Copy
    Worksheets.Add Count:=2, After:=Sheets(1)
    Worksheets("Sheet2").Name = "Processed Data"
    Range("A:A").Select
    ActiveSheet.Paste
' Removes header information and moves all data up
    Range("A1:I13").Select
    Selection.Cut
    Range("N14").Select
    ActiveSheet.Paste
    Range("A1:A13").Select
    Selection.Delete Shift:=xlUp
' Gathers 214nm, 280nm and 330nm data along with current and potential data
   'Also records the data sets used in the original file sheet
    datastart = Cells(1, 1).Address
    datafinish = Cells(dataset, 1).Address
    Range(datastart, datafinish).Cut
```

```
Columns("C:C").Select
ActiveSheet.Paste
Worksheets("Original Data").Cells(15, 4) = "Data Ranges"
Worksheets("Original Data").Cells(16, 3) = "214nm"
Worksheets("Original Data").Cells(17, 3) = "280nm"
Worksheets("Original Data").Cells(18, 3) = "330nm"
Worksheets("Original Data").Cells(19, 3) = "Potential kV"
Worksheets("Original Data").Cells(20, 3) = "Current i"
Worksheets("Original Data").Cells(16, 4) = datastart
Worksheets("Original Data").Cells(16, 5) = datafinish
datastart = Cells(dataset + 1, 1).Address
datafinish = Cells(dataset2, 1).Address
Range(datastart, datafinish).Cut
Columns("D:D").Select
ActiveSheet.Paste
Worksheets("Original Data").Cells(17, 4) = datastart
Worksheets("Original Data").Cells(17, 5) = datafinish
datastart = Cells(dataset2 + 1, 1).Address
datafinish = Cells(dataset3, 1).Address
Range(datastart, datafinish).Cut
Columns("E:E").Select
ActiveSheet.Paste
Worksheets("Original Data").Cells(18, 4) = datastart
Worksheets("Original Data").Cells(18, 5) = datafinish
datastart = Cells(dataset3 + 1, 1).Address
datafinish = Cells(dataset5, 1).Address
Range(datastart, datafinish).Select
```

```
Selection.ClearContents
datastart = Cells(dataset5 + 1, 1).Address
datafinish = Cells(dataset6, 1).Address
Range(datastart, datafinish).Cut
Columns("F:F").Select
ActiveSheet.Paste
Worksheets("Original Data").Cells(19, 4) = datastart
Worksheets("Original Data").Cells(19, 5) = datafinish
datastart = Cells(dataset6 + 1, 1).Address
datafinish = Cells(dataset7, 1).Address
Range(datastart, datafinish).Cut
Columns("G:G").Select
ActiveSheet.Paste
Worksheets("Original Data").Cells(20, 4) = datastart
Worksheets("Original Data").Cells(20, 5) = datafinish
 'Assigns each data type range, and multiplies the data with the Y multiplier value for each data set and creates a time data column
datastart = Cells(1, 8).Address
datafinish = Cells(dataset, 8).Address
Range(datastart, datafinish).FormulaR1C1 = "=(ROW(RC)-1)/(60*R21C15)  "
For j = 9 To 13
Data = Cells(1, j).Address
Data1 = Cells(dataset, j).Address
Range(Data, Data1) = "=RC[-6]*R26C15"
Next j
```

```
'Pastes processed data into a usable format and removes all the junk- removes the first data point in each set
    For j = 8 To 13
    Data = Cells(1, j).Address
    Data1 = Cells(dataset, j).Address
    Range(Data, Data1).Copy
    Cells(2, j - 7).PasteSpecial Paste:=xlPasteValues
    Next j
'Labels the columns of data
    Range("A1").FormulaR1C1 = "Time/min"
    Range("B1").FormulaR1C1 = "214nm"
    Range("C1").FormulaR1C1 = "280nm"
    Range("D1").FormulaR1C1 = "330nm"
    Range("E1").FormulaR1C1 = "Potential/kV"
    Range("F1").FormulaR1C1 = "Current/uA"
    Range("G:V").ClearContents
End Sub
```

UV CE Instrument File Conversion Macro

```
' Macro recorded 8/24/2009 by Mike Ivanov
' Keyboard Shortcut: Ctrl+i
'Open text file.
    FileOpenName = Application.GetOpenFilename
    If FileOpenName = False Then Exit Sub
    Workbooks.Open FileOpenName
    ActiveSheet.Range("A:A").TextToColumns DataType:=xlDelimited, Comma:=True
```

```
    Application.ScreenUpdating = False
'Creates a data set based on the number of points in a file, currently it uses data already contained in the file
'dataset = InputBox("How many data points are in the set?")
    dataset = Range("B9")
'Initializes a data counter and declares variables
    Dim dataset2 As Integer
    Dim dataset3 As Integer
    dataset2 = dataset * 2
    dataset3 = dataset * 3
'Rename active sheet, create new data sheets, and sort data.
    ActiveSheet.Name = "Original Data"
    Range("A:D").Select
    Selection.Copy
    Worksheets.Add Count:=2, After:=Sheets(1)
    Worksheets("Sheet2").Name = "Processed Data"
    Range("A:A").Select
    ActiveSheet.Paste
' Removes header information and moves all data up
    Range("A1:D13").Select
    Selection.Cut
    Range("N14").Select
    ActiveSheet.Paste
    Range("A1:A13").Select
    Selection.Delete Shift:=xlUp
' Gathers 230nm data along with current and potential data
  'Also records the data sets used in the original file sheet
```

```
datastart = Cells(1, 1).Address
datafinish = Cells(dataset, 1).Address
Range(datastart, datafinish).Cut
Columns("C:C").Select
ActiveSheet.Paste
Worksheets("Original Data").Cells(15, 4) = "Data Ranges"
Worksheets("Original Data").Cells(16, 3) = "214nm"
Worksheets("Original Data").Cells(17, 3) = "Potential kV"
Worksheets("Original Data").Cells(18, 3) = "Current i"
Worksheets("Original Data").Cells(16, 4) = datastart
Worksheets("Original Data").Cells(16, 5) = datafinish
datastart = Cells(dataset + 1, 1).Address
datafinish = Cells(dataset2, 1).Address
Range(datastart, datafinish).Cut
Columns("D:D").Select
ActiveSheet.Paste
Worksheets("Original Data").Cells(17, 4) = datastart
Worksheets("Original Data").Cells(17, 5) = datafinish
datastart = Cells(dataset2 + 1, 1).Address
datafinish = Cells(dataset3, 1).Address
Range(datastart, datafinish).Cut
Columns("E:E").Select
ActiveSheet.Paste
Worksheets("Original Data").Cells(18, 4) = datastart
Worksheets("Original Data").Cells(18, 5) = datafinish
Range(datastart, datafinish).Select
Selection.ClearContents
```

```
' Multiplies the data with the Y multiplier value for each data set and creates a time data column
    Range("H1").FormulaR1C1 = "=RC[-5]*R26C15"
    Range("I1").FormulaR1C1 = "=RC[-5]*R26C16"
    Range("J1").FormulaR1C1 = "=RC[-5]*R26C17"
    Range("K1").FormulaR1C1 = "=(ROW(RC)-1)/(60*R21C15)"
    Columns("H:K").FillDown
'Pastes processed data into a usable format and removes all the junk- removes the first data point in each set
    For j = 8 To 11
    Data = Cells(1, j).Address
    Data1 = Cells(dataset, j).Address
    Range(Data, Data1).Copy
    Cells(2, j - 7).PasteSpecial Paste:=xlPasteValues
    Next j
'Labels the columns of data
    Range("A1").FormulaR1C1 = "214nm"
    Range("B1").FormulaR1C1 = "Potential/kV"
    Range("C1").FormulaR1C1 = "Current/uA"
    Range("D1").FormulaR1C1 = "Time/min"
    Range("E:V").ClearContents
'Prompts a file save
    'ActiveWorkbook.Save
    End Sub
   Sub Macro1()
```

REFERENCES

1 Tiselius, A. *Transactions of the Faraday Society* **1937**, 33(524.

2 Hjerten, S. *Chromatography Reviews* **1967**, 9(1), 122-219.

3 Jorgenson, J. W.; Lukacs, K. D. *Analytical Chemistry* **1981**, 53(8), 1298-1302.

4 Tsuda, T.; Nomura, K.; Nakagawa, G. *Journal of Chromatography A* **1983**, 264(1), 385-392.

5 Huang, M. F.; Kuo, Y. C.; Huang, C. C.; Chang, H. T. *Analytical Chemistry* **2004**, 76(1), 192-196.

6 Clark, B. K.; Vo Dinh, T.; Sepaniak, M. J. *Analytical Chemistry* **1995**, 67(3), 680-3.

7 Goodall, D. M.; Williams, S. J.; Lloyd, D. K. *TrAC, Trends in Analytical Chemistry* **1991**, 10(9), 272-279.

8 Rose, D. J.; Jorgenson, J. W. *Analytical Chemistry* **1988**, 60(7), 642-648.

9 Karger, B. L.; Foret, F. *Capillary Electrophoresis: Introduction and Assessment*, 1st ed.; Marcel Dekker: New York, New York, USA, **1993**.

10 Altria, K. *Journal of Chromatography A* **1999**, 856(443.

11 Li, S. F. Y. *Capillary Electrophoresis: Principles, Practice and Applications*, 1st ed.; Elsevier: Amsterdam, **1992**.

12 Terabe, S.; Otsuka, K.; Ichikawa, K.; Tsuchiya, A.; Ando, T. *Analytical Chemistry* **1984**, 56(1), 111-113.

13 Terabe, S.; Otsuka, K.; Ando, T. *Analytical Chemistry* **1985**, 57(4), 834-841.

14 Sepaniak, M. J.; Burton, D. E.; Maskarinec, M. P. *Ordered Media in Chemical Separations (ACS Symposium Series)*, 1st ed.; America Chemical Society: Washington D.C, **1987**.

15 Hiroyuki, N. *Journal of Chromatography A* **1991**, 553(503-516.

16 Vindevogel, J.; Sandra, P. *Analytical Chemistry* **1991**, 63(15), 1530-1536.

17 Yashima, T.; Tsuchiya, A.; Morita, O.; Terabe, S. *Analytical Chemistry* **1992**, 64(23), 2981-2984.

18 Seifar, R. M.; Kraak, J. C.; Kok, W. T. *Analytical Chemistry* **1997**, 69(14), 2772-2778.

19 Jorgenson, J. W.; Lukacs, K. D. *Journal of Chromatgography A* **1981**, 218(209-216.

20 Cohen, A. S.; Karger, B. L. *Journal of Chromatography A* **1987**, 397(409-417.

21 Huhn, C.; Ramautar, R.; Wuhrer, M.; Somsen, G. *Analytical and Bioanalytical Chemistry* **2010**, 396(1), 297-314.

22 Pyell, U. *Fundementals of Capillary Electrophoresis*, 1st ed.; Marcel Dekker: New York, **2001**.

23 Wen, E.; Asiaie, R.; Horváth, C. *Journal of Chromatography A* **1999**, 855(2), 349-366.

24 Yu, C. J.; Su, C. L.; Tseng, W. L. *Analytical Chemistry* **2006**, 78(23), 8004-8010.

25 Hsieh, Y. *Electrophoresis* **2005**, 26(4089-4097.

26 Freitag, R. *Journal of Chromatography A* **2004**, 1033(2), 267-273.

27 Roduner, E. *Chemical Society Reviews* **2006**, 35(7), 583-592.

28 Eustis, S.; El-Sayed, M. A. *Chemical Society Reviews* **2006**, 35(209-217.

29 Wallingford, R. A.; Ewing, A. G. *Advances in Chromatography* **1989**, 29(1-76.

30 Nilsson, C.; Nilsson, S. *Electrophoresis* **2006**, 27(76-83.

31 Nilsson, C.; Birnbaum, S.; Nilsson, S. *Journal of Chromatgography A* **2007**, 1168(212-224.

32 Guihen, E.; Glennon, J. D. *Analytical Letters* **2003**, 36(15), 3309-3336.

33 Gottlicher, B.; Bachmann, K. *Journal of Chromatography A* **1997**, 780(63-73.

34 Pumera, M.; Escarpa, A. *Electrophoresis* **2009**, 30(19), 3315-3323.

35 Surugau, N.; Urban, P. L. *Journal of Separation Science* **2009**, 32(11), 1889-1906.

36 Dang, Y.; Zhang, Y.; Fan, L.; Chen, H.; Roco, M. *Journal of Nanoparticle Research* **2010**, 12(3), 687-706.

37 21st Century Nanotechnology Research and Development Act, 2003, 108-153.

38 Grass, M. *Journal of Physical Chemistry C* **2009**, 113(8616-8623.

39 Yang, S. B. *Journal of Physical Chemistry C* **2010**, 114(9296-9300.

40 Hori, H.; Yamamato, T.; Iwamoto, T. *Physical Review B* **2004**, 69(174411.

41 Smart, S. *Journal of Applied Polymer Science* **2010**, 117(1), 24-32.

42 Nehl, C. L.; Hafner, J. H. *Journal of Materials Chemistry* **2008**, 18(2415-2419.

43 Buffat, P. *Physical Review A* **1976**, 13(6), 2287-2298.

44 Srisombat, L.; Park, J.; Zhang, S.; Lee, T. R. *Langmuir* **2008**, 24(15), 7750-7754.

45 Weisbecker, C. S.; Merritt, M. V.; Whitesides, G. M. *Langmuir* **1996**, 12(16), 3763-3772.

46 Lee, S.; Jun, Y.; Cho, S.; Cheon, J. *Journal of the American Chemical Society* **2002**, 124(38), 11244-11245.

47 Murphy, C. J. *Journal of Physical Chemistry B* **2005**, 109(13857-13870.

48 Kuo, I.; Huang, Y.; Chang, H. *Electrophoresis* **2005**, 26(13), 2643-2651.

49 Wang, W.; Zhao, L.; Zhou, F.; Zhu, J. J.; Zhang, J. R. *Talanta* **2007**, 73(3), 534-539.

50 Li, M.; Tseng, W.; Cheng, T. *Journal of Chromatography A* **2009**, 1216(36), 6451-6458.

51 Agüí, L.; Yáñez-Sedeño, P.; Pingarrón, J. M. *Analytica Chimica Acta* **2008**, 622(1-2), 11-47.

52 Li, Y.; Chen, Y.; Xiang, R.; Ciuparu, D.; Pfefferle, L. D.; Horvath, C.; Wilkins, J. A. *Analytical Chemistry* **2005**, 77(5), 1398-1406.

53 Luong, J. H. T.; Bouvrette, P.; Liu, Y.; Yang, D.-Q.; Sacher, E. *Journal of Chromatography A* **2005**, 1074(1-2), 187-194.

54 Jiménez-Soto, J. M.; Moliner-Martínez, Y.; Cárdenas, S.; Valcárcel, M. *Electrophoresis* **2010**, 31(1-8.

55 Xu, Y.; Li, S. F. Y. *Electrophoresis* **2006**, 27(20), 4025-4028.

56 Zhou, W.; Bai, X.; Wang, E.; Xie, S. *Advanced Materials* **2009**, 21(45), 4565-4583.

57 Bahr, J. L.; Mickelson, E. T.; Bronikowski, M. J.; Smalley, R. E.; Tour, J. M. *Chemical Communications* **2001**, 2001(193-194.

58 Zhao, W.; Song, C.; Pehrsson, P. E. *Journal of the American Chemical Society* **2002**, 124(42), 12418-12419.

59 Chen, J.; Rao, A. M.; Lyuksyutov, S.; Itkis, M. E.; Hamon, M. A.; Hu, H.; Cohn, R. W.; Eklund, P. C.; Colbert, D. T.; Smalley, R. E.; Haddon, R. C. *The Journal of Physical Chemistry B* **2001**, 105(13), 2525-2528.

60 Wang, Z.; Luo, G.; Chen, J.; Xiao, S.; Wang, Y. *Electrophoresis* **2003**, 24(24), 4181-4188.

61 Suárez, B.; Simonet, B. M.; Cárdenas, S.; Valcárcel, M. *Electrophoresis* **2007**, 28(11), 1714-1722.

62 Palmer, C.; Hilder, E. F.; Quirino, J. P. *Analytical Chemistry* **2010**, 82(10), 4046-4054.

63 Fujimoto, C. *Journal of High Resolution Chromatography* **1997**, 20(400-402.

64 Liu, D. N. *Electrophoresis* **2008**, 29(863-870.

65 Wang, Y. *Talanta* **2009**, 77(1667.

66 Bächmann, K.; Göttlicher, B.; Haag, I.; Han, K. Y.; Hensel, W.; Mainka, A. *Journal of Chromatography A* **1994**, 688(1-2), 283-292.

67 Campbell, D. J.; Xia, Y. *Journal of Chemical Education* **2007**, 84(1), 91-96.

68 Haes, A. J.; Zou, S.; Zhao, J.; Schatz, G. C.; Van Duyne, R. P. *Journal of the American Chemical Society* **2006**, 128(33), 10905-10914.

69 Daniel, M. C.; Astruc, D. *Chemical Reviews* **2004**, 104(293-346.

70 Malinsky, M. D.; Kelly, K. L.; Schatz, G. C.; Van Duyne, R. P. *Journal of the American Chemical Society* **2001**, 123(7), 1471-1482.

71 Golden, M. S.; Bjonnes, A. C.; Georgiadis, R. M. *The Journal of Physical Chemistry C* **2010**, 114(19), 8837-8843.

72 Kelly, K. L.; Coronado, E.; Zhao, L.; Schatz, G. C. *Journal of Physical Chemistry B* **2003**, 107(3), 668-677.

73 Haes, A. J.; Zou, S.; Schatz, G. C.; Van Duyne, R. P. *Journal of Physical Chemistry B* **2004**, 108(1), 109-116.

74 Xia, Y.; Halas, N. J. *MRS Bulletin* **2005**, 30(338-346.

75 Haes, A. J.; Hall, W. P.; Chang, L.; Klein, W. L.; Van Duyne, R. P. *Nano Letters* **2004**, 4(6), 1029-1034.

76 Sinha, R.; Kim, G. J.; Nie, S.; Shin, D. M. *Molecular Cancer Therapeutics* **2006**, 5(8), 1909-1917.

77 Cuenca, A. G.; Jiang, H.; Hochwald, S. N.; Delano, M.; Cance, W. G.; Grobmyer, S. R. *Cancer* **2006**, 107(3), 459-466.

78 Campbell, D. J.; Herr, B. R.; Hulteen, J. C.; Van Duyne, R. P.; Mirkin, C. A. *Journal of the American Chemical Society* **1996**, 118(42), 10211-10219.

79 Campion, A.; Kambhampati, P. *Chemical Society Reviews* **1998**, 27(4), 241-250.

80 Rooth, M.; Shaw, A. M. *The Journal of Physical Chemistry C* **2007**, 111(42), 15363-15369.

81 Volkert, A. A.; Subramaniam, V.; Ivanov, M. R.; Jones, A. M.; Haes Amanda, J. *ACS Nano* **2011**, Submitted(1),

82 Haes, A. J.; Zou, S.; Schatz, G. C.; Van Duyne, R. P. *Journal of Physical Chemistry B* **2004**, 108(22), 6961-6968.

83 Hostetler, M. J.; Wingate, J. E.; Zhong, C. J.; Harris, J. E.; Vachet, R. W.; Clark, M. R.; Londono, J. D.; Green, S. J.; Stokes, J. J.; Wignall, G. D.; Glish, G. L.; Porter, M. D.; Evans, N. D.; Murray, R. W. *Langmuir* **1998**, 14(1), 17-30.

84 Templeton, A. C.; Wuelfing, W. P.; Murray, R. W. *Accounts of Chemical Research* **1999**, 33(1), 27-36.

85 Hostetler, M. J.; Templeton, A. C.; Murray, R. W. *Langmuir* **1999**, 15(11), 3782-3789.

86 Abad, J. M.; Mertens, S. F. L.; Pita, M.; Fernandez, V. M.; Schiffrin, D. J. *Journal of the American Chemical Society* **2005**, 127(15), 5689-5694.

87 Verwey, E. J.; Overbeek, J. T. *Theory of the Stability of Lyophilic Colloids*, 1st ed.; Elsevier: Amsterdam, **1948**.

88 Stebounova, L.; Guio, E.; Grassian, V. *Journal of Nanoparticle Research* **2010**, 1-12.

89 Haiss, W.; Thanh, N. T. K.; Aveyard, J.; Fernig, D. G. *Analytical Chemistry* **2007**, 79(11), 4215-4221.

90 Mayya, K. S.; Patil, V.; Sastry, M. *Langmuir* **1997**, 13(15), 3944-3947.

91 Hiemenz, P. C.; Rajagopalan, R. *Principles of Colloid and Surface Chemistry*, 3rd ed.; Marcel Dekkar: New York, **1997**.

92 Alvarez-Puebla, R. A.; Arceo, E.; Goulet, P. J. G.; Garrido, J. J.; Aroca, R. F. *The Journal of Physical Chemistry B* **2005**, 109(9), 3787-3792.

93 Park, J. N.; Forman, A. J.; Tang, W.; Cheng, J. H.; Hu, Y. S.; Lin, H. F.; McFarland, E. W. *Small* **2008**, 4(10), 1694-1697.

94 Zhang, S.; Leem, G.; Srisombat, L.; Lee, T. R. *Journal of the American Chemical Society* **2007**, 130(1), 113-120.

95 Leff, D. V.; Brandt, L.; Heath, J. R. *Langmuir* **1996**, 12(20), 4723-4730.

96 Zhou, H. Y.; Du, F. F.; Li, X.; Zhang, B.; Li, W.; Yan, B. *Journal of Physical Chemistry C* **2008**, 112(49), 19360-19366.

97 Badia, A.; Demers, L.; Dickinson, L.; Morin, F. G.; Lennox, R. B.; Reven, L. *Journal of the American Chemical Society* **1997**, 119(45), 11104-11105.

98 Kohlmann, O.; Steinmetz, W. E.; Mao, X. A.; Wuelfing, W. P.; Templeton, A. C.; Murray, R. W.; Johnson, C. S. *The Journal of Physical Chemistry B* **2001**, 105(37), 8801-8809.

99 Terrill, R. H.; Postlethwaite, T. A.; Chen, C.; Poon, C.; Terzis, A.; Chen, A.; Hutchison, J. E.; Clark, M. R.; Wignall, G. *Journal of the American Chemical Society* **1995**, 117(50), 12537-12548.

100 Schmitt, H.; Badia, A.; Dickinson, L.; Reven, L.; Lennox, R. B. *Advanced Materials* **1998**, 10(6), 475-480.

101 Neiman, B.; Grushka, E.; Lev, O. *Analytical Chemistry* **2001**, 73(21), 5220-5227.

102 Viberg, P.; Jornten-Karlsson, M.; Petersson, P.; Spagel, P.; Nilsson, S. *Analytical Chemistry* **2002**, 74(18), 4595-4601.

103 Nilsson, C.; Viberg, P.; Spegel, P.; Jornten-Karlsson, M.; Petersson, P.; Nilsson, S. *Analytical Chemistry* **2006**, 78(17), 6088-6095.

104 Neiman, B.; Grushka, E.; Gun, J.; Lev, O. *Analytical Chemistry* **2002**, 74(14), 3484-3491.

105 Suarez, B.; Simonet, B. M.; Cardenas, S.; Valcarcel, M. *Journal of Chromatography, A* **2006**, 1128(1-2), 282-289.

106 Ivanov, M. R.; Bednar, H. R.; Haes, A. J. *ACS Nano* **2009**, 3(2), 386-394.

107 Yang, L.; Guihen, E.; Holmes, J. D.; Loughran, M.; O'Sullivan, G. P.; Glennon, J. D. *Analytical Chemistry* **2005**, 77(6), 1840-1846.

108 Zhang, Z. *Electrophoresis* **2009**, 30(379-387.

109 Bachmann, S. *Electrophoresis* **2010**, 31(618-629.

110 Ulman, A. *Chemical Reviews* **1996**, 96(4), 1533-1554.

111 Hickman, J. J.; Ofer, D.; Laibinis, P. E.; Whitesides, G. M.; Wrighton, M. S. *Science* **1991**, 252(5006), 688-691.

112 Mirkin, C. A.; Ratner, M. A. *Annual Review of Physical Chemistry* **1992**, 43(1), 719-754.

113 Wollman, E. W.; Kang, D.; Frisbie, C. D.; Lorkovic, I. M.; Wrighton, M. S. *Journal of the American Chemical Society* **1994**, 116(10), 4395-4404.

114 Bonnemann, H.; Richards, R. *European Journal of Inorganic Chemistry* **2001**, 10(2455-2480.

115 Noh, J.; Kato, H. S.; Kawai, M.; Hara, M. *Journal of physical Chemistry B* **2006**, 110(6), 2793-2797.

116 Dameron, A. A.; Charles, L. F.; Weiss, P. S. *Journal of the American Chemical Society* **2005**, 127(24), 8697-8704.

117 Crooks, R. M.; Ricco, A. J. *Accounts of Chemical Research* **1998**, 31(5), 219-227.

118 Badia, A.; Lennox, R. B.; Reven, L. *Accounts of Chemical Research* **2000**, 33(7), 475-481.

119 Adams, D. M.; Brus, L. E.; Chidsey, C. E. D.; Creager, S. E.; Creuts, C.; Kagan, C. R.; Kamat, P. V.; Lieberman, M.; Lindsay, S.; Marcus, R. A.; Metzger, R. M.; Michel-Beyerle, M. E.; Miller, J. R.; Newton, M. D.; Rolison, D. R.; Sankey, O.; Schanze, K. S.; Yardley, J.; Zhu, X. Y. *Journal of Physical Chemistry B* **2003**, 107(6668-6697.

120 Fendler, J. H. *Chemistry of Materials* **2001**, 13(10), 3196-3210.

121 Brust, M.; Fink, J.; Bethell, D.; Schiffrin, D. *Journal of the Chemical Society: Chemical Communications* **1995**, 1655.

122 Weare, W. W.; Reed, S. M.; Warner, M. G.; Hutchison, J. E. *Journal of the American Chemical Society* **2000**, 122(51), 12890-12891.

123 Haes, A. J.; Zhao, J.; Zou, S.; Own, C. S.; Marks, L. D.; Schatz, G. C.; Van Duyne, R. P. *Journal of Physical Chemistry B* **2005**, 109(22), 11158-11162.

124 DeVries, G. A.; Talley, F. R.; Carney, R. P.; Stellacci, F. *Advanced Materials* **2008**, 20(22), 4243-4247.

125 Sardar, R.; Heap, T. B.; Shumaker-Parry, J. S. *Journal of the American Chemical Society* **2007**, 129(17), 5356-5357.

126 Shipway, A. N.; Katz, E.; Willner, I. *Chemical and Physical Chemistry* **2000**, 1(18-52.

127 Finklea, H. O. *Electroanalytical Chemistry* **1996**, 19(309-335.

128 Preiner, M. J.; Melosh, N. A. *Langmuir* **2009**, 25(5), 2585-2587.

129 Lusk, A. T.; Jennings, G. K. *Langmuir* **2001**, 17(25), 7830-7836.

130 Campuzano, S.; Pedrero, M.; Montemayor, C.; Fatas, E.; Pingarrón, J. M. *Journal of Electroanalytical Chemistry* **2006**, 586(1), 112-121.

131 Kwon, S.; Choi, J.; Lee, H. J.; Noh, J. *Colloids and Surfaces* **2008**, 313(324-327.

132 Losic, D.; Shapter, J. G.; Gooding, J. J. *Australian Journal of Chemistry* **2001**, 54(10), 643-648.

133 Losic, D.; Gooding, J. J.; Shapter, J. G.; Hibbert, D. B.; Short, K. *Electroanalysis* **2001**, 13(17), 1385-1393.

134 Losic, D.; Shapter, J. G.; Gooding, J. J. *Langmuir* **2001**, 17(11), 3307-3316.

135 Grabar, K. C.; Freeman, R. G.; Hommer, M. B.; Natan, M. J. *Analytical Chemistry* **1995**, 67(4), 735-43.

136 Usher, C. R.; Baltrusaitis, J.; Grassian, V. H. *Langmuir* **2007**, 23(13), 7039-7045.

137 Haes, A. J.; Haynes, C. L.; McFarland, A. D.; Schatz, G. C.; Van Duyne, R. P.; Zou, S. *MRS Bulletin* **2005**, 30(5), 368-375.

138 El-Sayed, M. A. *Accounts of Chemical Research* **2001**, 34(4), 257-264.

139 Link, S.; El-Sayed, M. A. *Journal of Physical Chemistry B* **1999**, 103(40), 8410-8426.

140 Bohren, C. F.; Huffman, D. R. *Absorption and Scattering of Light by Small Particles*, 1st ed.; Wiley Interscience: New York, **1983**.

141 Schmid, G. *Chemical Reviews* **1992**, 92(8), 1709-1727.

142 Aslan, K. *Langmuir* **2002**, 18(16), 6059-6065.

143 Haynes, C. L.; Haes, A. J.; McFarland, A. D.; Van Duyne, R. P. *Nanoparticles with Tunable Localized Surface Plasmon Resonances*, 1st ed.; Plenum Press: New York, **2003**.

144 Haynes, C. L.; Haes, A. J.; McFarland, A. D.; Van Duyne, R. P. *Topics in Fluorescence Spectroscopy* **2005**, 8(Radiative Decay Engineering), 47-99.

145 Mie, G. *Annalen der Physik (Weinheim, Germany)* **1908**, 25(377-445.

146 Song, Y.; Harper, A. S.; Murray, R. W. *Langmuir* **2005**, 21(12), 5492-5500.

147 Badia, A.; Gao, W.; Singh, S.; Demers, L.; Cuccia, L.; Reven, L. *Langmuir* **1996**, 12(5), 1262-1269.

148 Crespo, P.; Litrán, R.; Rojas, T. C.; Multigner, M.; de la Fuente, J. M.; Sánchez-López, J. C.; García, M. A.; Hernando, A.; Penadés, S.; Fernández, A. *Physical Review Letters* **2004**, 93(8), 087204.

149 Parks, G. A. *Chemical Reviews* **1965**, 65(2), 177-198.

150 Castner, D. G.; Hinds, K.; Grainger, D. W. *Langmuir* **1996**, 12(21), 5083-5086.

151 Baer, D. R.; Englehard, M. H. *Journal of Electron Spectroscopy and Related Phenomena* **2010**, 178(415-432.

152 Lumsden, J. B. *X-Ray Photoelectron Spectroscopy in Materials Characterizaton*, 1st ed.; American Society for Metals: **1986**.

153 Giray, C. B.; Dogan, M.; Akalin, A.; Baltrusaitis, J.; Chan, D. C.; Skinner, H. C.; Dogan, A. U. *Scanning* **2007**, 29(5), 206-210.

154 Jablonski, A. *Electron inelastic-mean-free-path database*, 1st ed.; National Institutes of Standards and Technology: Gaitherburg, MD, **2000**.

155 Beilschmidt, H.; Tiliuin, I. S.; Werner, W. S. M. *Surface and Interface Analysis* **1994**, 22(1-12), 120-123.

156 Schmid, G. *Advanced Engineering Materials* **2001**, 3(10), 737-743.

157 Cademartiri, L.; Ozin, G. *Concepts of Nanochemistry*, 1st ed.; Wiley-VCH: **2009**.

158 Cao, L.; Zhu, T.; Liu, Z. *Journal of Colloid and Interface Science* **2006**, 293(1), 69-76.

159 Wang, Z. L.; Petroski, J. M.; Green, T. C.; El-Sayed, M. A. *Journal of Physical Chemistry B* **1998**, 102(6145-6151.

160 Dong, Y. Z.; Abaci, S.; Shannon, C.; Bozack, M. J. *Langmuir* **2003**, 102(6145-6151.

161 Mazur, M.; Krysinski, P. *Langmuir* **2001**, 17(22), 7093-7101.

162 Willey, T. M.; Vance, A. L.; Bostedt, C.; Van Buuren, T.; Meulenberg, R. W.; Terminello, L. J.; Fadley, C. S. *Langmuir* **2004**, 20(12), 4939-4944.

163 Porter, M. D.; Bright, T. B.; Allara, D. L.; Chidsey, C. E. D. *Journal of the American Chemical Society* **1987**, 109(12), 3559-3568.

164 Schlenoff, J. B.; Li, M. D.; H., L. *Journal of the American Chemical Society* **1995**, 117(50), 12528-12536.

165 Fawcett, W. R.; Tikanen, A. C. *The Journal of Physical Chemistry* **1996**, 100(10), 4251-4255.

166 Volkert, A. A.; Subramaniam, V.; Haes, A. J. *Chemical Communications* **2011**, 47(1), 478-480.

167 Bishop, K.; Wilmer, C.; Soh, S.; Grzybowski, B. A. *Small* **2009**, 5(1), 1600-1630.

168 West, J. L.; Halas, N. J. *Current Opinion in Biotechnology* **2000**, 11(2), 215-217.

169 Shim, J.-H.; Lee, B. J.; Cho, Y. W. *Surface Science* **2002**, 512(3), 262-268.

170 Huang, X.; Jain, P. K.; El-Sayed, I. H.; El-Sayed, M. A. *Nanomedicine* **2007**, 2(5), 681-693.

171 Brennan, J. L.; Hatzakis, N. S.; Tshikhudo, T. R.; Razumas, V.; Patkar, S.; Vind, J.; Svendsen, A.; Nolte, R. J. M.; Rowan, A. E.; Brust, M. *Bioconjugate Chemistry* **2006**, 17(6), 1373-1375.

172 Tessier, P. M.; Velev, O. D.; Kalambur, A. T.; Rabolt, J. F.; Lenhoff, A. M.; Kaler, E. W. *Journal of the American Chemical Society* **2000**, 122(39), 9554-9555.

173 Talley, C. E.; Jackson, J. B.; Oubre, C.; Grady, N. K.; Hollars, C. W.; Lane, S. M.; Huser, T. R.; Nordlander, P.; Halas, N. J. *Nano Letters* **2005**, 5(8), 1569-1574.

174 Vericat, C. *Journal of Physics: Condensed Matter* **2006**, 18(48), R867-.

175 Bourg, M. C.; Badia, A.; Lennox, R. B. *The Journal of Physical Chemistry B* **2000**, 104(28), 6562-6567.

176 Felice, R. D.; Selloni, A. *The Journal of Chemical Physics* **2004**, 120(10), 4906-4914.

177 Tielens, F.; Santos, E. *The Journal of Physical Chemistry C* **2010**, 114(20), 9444-9452.

178 Chidsey, C. E. D.; Loiacono, D. N. *Langmuir* **1990**, 6(3), 682-691.

179 Wang, H.; Chen, S.; Li, L.; Jiang, S. *Langmuir* **2005**, 21(7), 2633-2636.

180 Chaki, N.; Aslam, M.; Sharma, J.; Vijayamohanan, K. *Applications of self-assembled monolayers in materials chemistry*, 1st ed.; Springer India: **2001**.

181 Yang, A.; Weng, C. *Journal of Physical Chemistry C* **2010**, 114(8697-8709.

182 He, H. X.; Zhang, H.; Li, Q. G.; Zhu, T.; Li, S. F. Y.; Liu, Z. F. *Langmuir* **2000**, 16(8), 3846-3851.

183 Liu, G.-Y.; Xu, S.; Qian, Y. *Accounts of Chemical Research* **2000**, 33(7), 457-466.

184 Jones, R. L.; Pearsall, N. C.; Batteas, J. D. *The Journal of Physical Chemistry C* **2009**, 113(11), 4507-4514.

185 Luedtke, W. D.; Landman, U. *The Journal of Physical Chemistry B* **1998**, 102(34), 6566-6572.

186 Truong, K. D.; Rowntree, P. A. *Journal of Physical Chemistry* **1996**, 100(19917-19926.

187 Calvente, J. J.; Lopez-Perez, G.; Jurado, J. M.; Andreu, R.; Molero, M.; Roldan, E. *Langmuir* **2009**, 26(4), 2914-2923.

188 Xu, S.; Cruchon-Dupeyrat, S. J. N.; Garno, J. C.; Liu, G.; Jennings, G. K.; Yong, T.; Laibinis, P. E. *The Journal of Chemical Physics* **1998**, 108(12), 5002-5012.

189 Bain, C. D.; Biebuyck, H. A.; Whitesides, G. M. *Langmuir* **1989**, 5(3), 723-727.

190 Peterlinz, K. A.; Georgiadis, R. *Langmuir* **1996**, 12(20), 4731-4740.

191 Georgiadis, R.; Peterlinz, K. P.; Peterson, A. W. *Journal of the American Chemical Society* **2000**, 122(13), 7837-3173.

192 Bensebaa, F.; Voicu, R.; Huron, L.; Ellis, T. H.; Kruus, E. *Langmuir* **1997**, 13(20), 5335-5340.

193 Prucker, O.; Ruhe, J. *Macromolecules* **1998**, 31(3), 592-601.

194 Gottlieb, H. E.; Kotlyar, V.; Nudelman, A. *The Journal of Organic Chemistry* **1997**, 62(21), 7512-7515.

195 Aizpurua, J.; Hanarp, P.; Sutherland, D. S.; Kall, M.; Bryant, G. W.; Garcia de Abajo, F. J. *Physical Review Letters* **2003**, 90(5), 057401-057404.

196 Alivisatos, A. P. *Science* **1996**, 271(933-937.

197 Linnert, T.; Mulvaney, P.; Henglein, A. *Journal of Physical Chemistry* **1993**, 97(3), 679-682.

198 Willets, K. A.; Van Duyne, R. P. *Annual Review of Physical Chemistry* **2007**, 58(1), 267-297.

199 Bellino, M. G.; Calvo, E. J.; Gordillo, G. *Physical Chemistry Chemical Physics* **2004**, 6(2), 424-428.

200 Biebuyck, H. A.; Bain, C. D.; Whitesides, G. M. *Langmuir* **1994**, 10(6), 1825-1831.

201 Cao, G. *Nanostructures and Nanomaterials: Synthesis, Properties and Applications*, 1st ed.; Imperial College Press: London, **2004**.

202 Love, J. C.; Estroff, L. A.; Kriebel, J. K.; Nuzzo, R. G.; Whitesides, G. M. *Chemical Reviews* **2005**, 105(4), 1103-1169.

203 Dubois, L. H.; Nuzzo, R. G. *Annual Review of Physical Chemistry* **1992**, 43(1), 437-463.

204 Kim, Y. T.; McCarley, R. L.; Bard, A. J. *Langmuir* **1993**, 9(8), 1941-1944.

205 Hao, E.; Schatz, G. C. *The Journal of Chemical Physics* **2004**, 120(1), 357-366.

206 Creager, S. E.; Clarke, J. *Langmuir* **1994**, 10(3675-3683.

207 Preston, T. C.; Nuruzzaman, M.; Jones, N. D.; Mittler, S. *The Journal of Physical Chemistry C* **2009**, 113(32), 14236-14244.

208 Smith, A. R.; Shenvi, S. V.; Widlansky, M.; Suh, J. H.; Hagen, T. *Current Medicinal Chemistry* **2004**, 11(1135-1146.

209 Letsinger, R. L.; Elghanian, R.; Viswanadham, G.; Mirkin, C. A. *Bioconjugate Chemistry* **2000**, 11(2), 289-291.

210 Yonezawa, T.; Yasui, K.; Kimizuka, N. *Langmuir* **2000**, 17(2), 271-273.

211 Shimazu, K.; Teranishi, T.; Sugihara, K.; Uosaki, K. *Chemistry Letters* **1998**, 27(7), 669-670.

212 Subramaniam, V.; Ivanov, M. R.; Volkert, A. A.; Jones, A. M.; Haes, A. J. *ACS Nano* **2010**, Submitted(

213 Hasan, M.; Bethell, D.; Brust, M. *Journal of the American Chemical Society* **2002**, 124(7), 1132-1133.

214 Porta, F.; Krpetici , Z.; Prati, L.; Gaiassi, A.; Scarile, G. *Langmuir* **2008**, 24(14), 7061-7064.

215 Sellers, H.; Ulman, A.; Shnidman, Y.; Eilers, J. E. *Journal of the American Chemical Society* **1993**, 115(21), 9389-9401.

216 Shiddiky, M. J. A.; Shim, Y. *Analytical Chemistry (Washington, DC, United States)* **2007**, 79(10), 3724-3733.

217 Pumera, M.; Wang, J.; Grushka, E.; Polsky, R. *Analytical Chemistry* **2001**, 73(22), 5625-5628.

218 He, L.; Natan, M. J.; Keating, C. D. *Analytical Chemistry* **2000**, 72(21), 5348-5355.

219 Connatser, R. M.; Riddle, L. A.; Sepaniak, M. J. *Journal of Separation Science* **2004**, 27(17-18), 1545-1550.

220 Dijkstra, R. J.; Ariese, F.; Gooijer, C.; Brinkman, U. A. *Trends in Analytical Chemistry* **2005**, 24(4), 304-323.

221 Seifar, R. M.; Dijkstra, R. J.; Gerssen, A.; Ariese, F.; Brinkman, U. A. T.; Gooijer, C. *Journal of Separation Science* **2002**, 25(13), 814-818.

222 Nirode, W. F.; Devault, G. L.; Sepaniak, M. J.; Cole, R. O. *Analytical Chemistry* **2000**, 72(8), 1866-1871.

223 Wang, Y.; Ouyang, J.; Baeyens, W. R. G.; Delanghe, J. R. *Expert Review of Proteomics* **2007**, 4(2), 287-298.

224 Liu, F. K.; Tsai, M. H.; Hsu, Y. C.; Chu, T. C. *Journal of Chromatography, A* **2006**, 1133(1-2), 340-346.

225 Song, X.; Li, L.; Qian, H.; Fang, N.; Ren, J. *Electrophoresis* **2006**, 27(7), 1341-1346.

226 Tseng, W. L.; Huang, M. F.; Huang, Y. F.; Chang, H. T. *Electrophoresis* **2005**, 26(16), 3069-3075.

227 Lin, Y. W.; Huang, M. F.; Chang, H. T. *Electrophoresis* **2005**, 26(2), 320-330.

228 Liu, F. K.; Hsu, Y. T.; Wu, C. H. *Journal of Chromatography, A* **2005**, 1083(1-2), 205-214.

229 Jensen, T. R.; Malinsky, M. D.; Haynes, C. L.; Van Duyne, R. P. *Journal of Physical Chemistry B* **2000**, 104(45), 10549-10556.

230 Kreibig, U.; Vollmer, M. *Cluster Materials*, 1st ed.; Springer-Verlag: Heidelberg, Germany, **1995**.

231 Ghosh, S.; Pal, T. *Chem. Rev.* **2007**, 107(11), 4797-4862.

232 Liz-Marzan, L. M. *Langmuir* **2006**, 22(32-41.

233 Heath, J. R.; Knobler, C. M.; Leff, D. V. *Journal of Physical Chemistry B* **1997**, 101(2), 189-197.

234 Rouhana, L. L.; Jaber, J. A.; Schlenoff, J. B. *Langmuir* **2007**, 23(26), 12799-12801.

235 Hunter, R. J. *Introduction to Modern Colloid Science*, ed.; Oxford University Press: **1993**.

236 Lin, S. Y.; Tsai, Y. T.; Chen, C. C.; Lin, C. M.; Chen, C. *Journal of Physical Chemistry B* **2004**, 108(2134-2139.

237 Hu, K.; Bard, A. *Langmuir* **1997**, 13(5114-5119.

238 van der Vegte, E. W.; Hadziioannou, G. *Journal of Physical Chemistry B* **1997**, 101(9563-9569.

239 Nishiyama, K.; Kubo, A.; Ueda, A.; Taniguchi, I. *Chemistry Letters* **2002**, 80-81.

240 Nitzan, B.; Margel, S. *Journal of Polymer Science, Part A: Polymer Chemistry* **1997**, 35(1), 171-181.

241 Mengistu, T. Z.; Goel, V.; Horton, J. H.; Morin, S. *Langmuir* **2006**, 22(12), 5301-5307.

242 MJFF Facts about Parkinson's Disease. http://www.michaeljfox.org/research.cfm (Oct. 20, 2010),

243 *Neuroscience*, 3rd ed.; Sinauer Associates, Inc.: Sunderland, Massachusetts, U.S.A, **2004**.

244 Bogdanov, M.; Matson, W. R.; Wang, L.; Matson, T.; Saunders-Pullman, R.; Bressman, S. S.; Beal, M. F. *Brain* **2008**, 131(389-396.

245 Michell, A. W.; Lewis, S. J. G.; Foltynie, T.; Barker, R. A. *Brain* **2004**, 127(1693-1705.

246 Landers, J. P. *Handbook of Capillary Electrophoresis*, 2nd ed.; CRC Press, Inc.: New York, **1997**.

247 Otevrel, M.; Kleparnik, K. *Electrophoresis* **2002**, 23(20), 3574-3582.

248 Doane, T. L.; Cheng, Y.; Babar, A.; Hill, R. J.; Burda, C. *Journal of the American Chemical Society* **2010**, 132(44), 15624-15631.

249 Hanauer, M.; Sebastien, P.; Zins, I.; Lotz, A. *Nano Letters* **2007**, 7(9), 2881-2885.

250 Makino, K.; Ohshima, H. *Langmuir* **2010**, 26(23), 18016-18019.

251 Dukhin, S. S. *Advances in Colloid and Interface Science* **1993**, 44(1-134.

252 Ohshima, H. *Colloids and Surfaces A: Physicochemical and Engineering Aspects* **2005**, 267(1-3), 50-55.

253 Ivanov, M. R.; Haes, A. J. *Analyst* **2011**, 136(1), 54-63.

254 Fazio, S.; Guzman, J.; Colomer, M. T.; Salomoni, A.; Moreno, R. *Journal of the European Ceramic Society* **2008**, 28(11), 2171-2176.

255 Vincent, B. *Colloid and Surfaces* **1986**, 18(261-281.

256 Fritz, G. *Langmuir* **2002**, 18(6381-6390.

257 Kamiyama, Y.; Israelachvili, J. *Macromolecules* **1992**, 25(19), 5081-5088.

258 Likos, C. N.; Vaynberg, K. A. *Langmuir* **2000**, 16(9), 4100-4108.

259 Richardson, J. N.; Dyer, A. L.; Stegemiller, M. L.; Zudans, I.; Seliskar, C. J.; Heineman, W. R. *Analytical Chemistry* **2002**, 74(14), 3330-3335.

260 Sachs, S. B.; Dudek, S. P.; Hsung, R. P.; Sita, L. R.; Smalley, J. F.; Newton, M. D.; Feldberg, S. W.; Chidsey, C. E. D. *Journal of the American Chemical Society* **1997**, 119(43), 10563-10564.

261 Bard, A. J. *Electrochemical Methods*, 2nd ed.; J. Wiley and Sons: **2001**.

262 Smalley, J. F. *Langmuir* **2003**, 19(22), 9284-9289.

263 Stoessl, A. J. *Expert Opinion on Therapeutic Targets* **2008**, 12(4), 425-436.

264 Younes-Mhenni, S.; Frih-Ayed, M.; Kerkeni, A.; Bost, M.; Chazot, G. *European Neurology* **2007**, 58(2), 78-83.

265 Sato, S.; Mizuno, Y.; Hattori, N. *Neurology* **2005**, 64(1081-1083.

266 Offen, D.; Ziv, I.; Barzilai, A.; Gorodin, S.; Glater, E.; Hochman, A.; Melamed, E. *Neurochemistry International* **1997**, 31(2), 207-216.

267 Ben-Shachar, D.; Riederer, P.; Youdim, M. B. H. *Journal of Neurochemistry* **1991**, 57(5), 1609-1614.

268 Youdim, M. B. H.; Ben-Shachar, D.; Riederer, P. *Acta Neurologica Scandinavica* **1989**, 80(47-54.

269 Burgi, D. S.; Chien, R. L. *Analytical Chemistry* **1991**, 63(18), 2042-2047.

270 Grzelczak, M.; Perez-Juste, J.; Mulvaney, P.; Liz-Marzan, L. M. *Chemical Society Reviews* **2008**, 37(9), 1783-1791.

271 Han, L.; Sakamoto, Y.; Terasaki, O.; Li, Y.; Che, S. *Journal of Materials Chemistry* **2007**, 17(12), 1216-1221.

272 Freitas, C.; Müller, R. H. *International Journal of Pharmaceutics* **1998**, 168(2), 221-229.

273 Narayanan, R.; El-Sayed, M. A. *Journal of Physical Chemistry B* **2005**, 109(26), 12663-12676.

274 Martin, C. R.; Mitchell, D. T. *Template-synthesized nanomaterials in electrochemistry*, 1st ed.; Marcel Dekker: New York, **1999**.

275 Medoz, J.; Kuznetzov, B. A.; Medrano, F. J.; Garcia, J. L.; Fernadez, V. M. *Journal of the American Chemical Society* **1997**, 119(5), 1043-1051.

276 Kewabata, S.; Fukuzaki, R.; Nishizawa, M.; Martin, C. R.; Yoneyama, H. *Langmuir* **1991**, 15(20), 6807-6812.

277 Miller, J. M. *Chromatography: Concepts and Contrasts, Second Edition*, 2nd ed.; John Wiley & Sons, Inc.: **2005**.

278 Subramaniam, V.; Griffith, L.; Haes, A. J. *Analyst* **2011**, DOI: 10. 1039/C1AN15185A(

279 Vinther, A.; Soeberg, H. *Journal of Chromatography* **1991**, 559(1-2), 27-42.